ATMOSPHERIC AND OCEANIC 40- TO 50-DAY OSCILLATIONS IN THE SOURCE REGION OF THE SOMALI CURRENT

by

GORDON JAMES MERTZ

B.Sc., University Of British Columbia, 1975
M.Sc., University Of British Columbia, 1977

A THESIS SUBMITTED IN PARTIAL FULFILMENT OF

THE REQUIREMENTS FOR THE DEGREE OF

DOCTOR OF PHILOSOPHY

in

THE FACULTY OF GRADUATE STUDIES

Department Of Physics

We accept this thesis as conforming

to the required standard

THE UNIVERSITY OF BRITISH COLUMBIA

November 1985

In presenting this thesis in partial fulfilment of the requirements for an advanced degree at the University of British Columbia, I agree that the Library shall make it freely available for reference and study. I further agree that permission for extensive copying of this thesis for scholarly purposes may be granted by the head of my department or by his or her representatives. It is understood that copying or publication of this thesis for financial gain shall not be allowed without my written permission.

Department of PHYSICS

The University of British Columbia
1956 Main Mall
Vancouver, Canada
V6T 1Y3

Date Oct. 10, 1985

ABSTRACT

Current and temperature data were acquired in the source region of the Somali Current, jointly by the Universities of Kiel and Miami, as part of the INDEX pilot studies. The data were acquired over a six-month period (January-July, 1976) which spans the springtime Monsoon reversal. The experiment and the data are described in Düing and Schott (1978).

This thesis describes the results of the spectrum analysis of fluctuations found in data from the experiment's two southernmost sensor locations. It is found that, once the annual cycle is removed, most of the variance in these current and temperature records resides in subinertial fluctuations. The most prominent spectral feature is a 40- to 50-day peak.

This 40- to 50-day period is coincident with that of the global-scale circulation cells found in the tropical atmosphere by Madden and Julian (1971 and 1972). The analysis of wind stress and wind stress curl data for the years 1976 and 1979 presented in this thesis indicate that the 40-to 50-day oscillation was present over the Western Indian Ocean during these years. It is suggested here that wind-forcing excites a long coastally trapped wave. To test this idea, a wind-forced quasi-geostrophic, three-layer model and a reduced-gravity model incorporating lateral mean current shear are applied to the Somali Current regime. Model results suggest that the wind forcing is strong enough to excite the observed current and

temperature fluctuations.

TABLE OF CONTENTS

List of Tables

List of Figure Captions

Acknowledgments

I would like to express my gratitude to all the persons involved in the completion of this thesis. I particularly thank Dr. L. A. Mysak for his guidance and exceptional patience. I also thank Drs. R. W. Burling, P. H. LeBlond, and K. Hamilton for reading this thesis and for many helpful suggestions.

The oceanographic and meteorological data were supplied by Dr. F. Schott at the University of Miami.

I am grateful to the University of British Columbia for support through Graduate Fellowships and to the Natural Sciences and Engineering Research Council of Canada for Post Graduate Scholarships. I am also grateful to the U.S. Office of Naval Research (Code 422PO) for support as a Research Assistant at the later stages of this work.

I. Introduction

It is now widely appreciated that the tropical atmosphere and ocean exert an important influence on weather and climate worldwide. Kerr (1984) notes that

> "It is an axiom of meteorology that no part of the atmosphere stands alone; everything is interconnected. It is a frustration of meteorology that major, sometimes catastrophic, atmospheric effects arise from the complex interconnection of numerous, subtle, and obscure causes. El Niño has recently become a prominent example of how elusive changes in the ocean and atmosphere can sometimes lead to dramatic shifts in the behavior of the atmosphere, sending abnormal weather through the entire system.
>
> It now seems that another prominent phenomenon, whose existence long eluded meteorologists and whose significance is only now becoming apparent, sets the circulation of the tropics pulsating at a far faster pace than the irregular 3- to 8-year recurrence time of El Niño. From a satellite's perch, the new phenomenon appears as a wave of cloudiness that first develops every 40 to 50 days in the Indian Ocean..."

This 40- to 50-day oscillation is the subject of this thesis. Recently, this oscillation has become the object of intense meteorological interest since it spreads from its origin

in the Indian Ocean throughout the Pacific Ocean with meridionally propagating branches spreading as far off as the poles. Perhaps most significantly, this 40- to 50-day oscillation may play a role in triggering the onset and withdrawal of the Indian Monsoon, causing monsoon rains to pause in midseason. The 40- to 50-day oscillation has even been implicated in reshaping the jet stream (via modification of the monsoon) that plays a central role in North American weather.

The strength of this oscillation in the atmosphere implies the likelihood of finding it in the ocean. However, it is only relatively recently that this oscillation has been definitively identified there (Luther, 1980). Even less work has been done on the relation between the atmospheric and oceanic 40- to 50-day oscillations.

In this thesis I will examine the 40- to 50-day oscillation, in both the atmosphere and the ocean, in a very interesting area, namely, the source region of the Somali Current. This area forms part of the western boundary of the Indian Ocean, and is thought to be the source of the 40- to 50-day oscillation. The area is one of marked land-sea contrast, known to be important in generating monsoons and other convective phenomena. Nearby lie the East African Highlands which profoundly affect the circulation of this region. The annual reversal of the major Somali Current system must have an important effect on any oscillations present. I will show that the properties of the 40- to 50-day oscillation are indeed unique in this area; most importantly, I identify a 40- to 50-

day signal propagating as a coastal wave that appears to be driven by fluctuations in the wind stress curl (this is also the first identification of a 40- to 50-day fluctuation in the wind stress curl).

The plan of the thesis is as follows: In Chapter II the observations of the 40- to 50-day oscillation reported in the literature to date are reviewed. Relevant meteorological and oceanographic background information is provided. Chapter III presents an analysis of oceanographic and meteorological data collected near the source region of the Somali Current, and establishes the existence and properties of the 40- to 50-day oscillation in this area. Chapter IV is concerned with relating the atmospheric and oceanic 40- to 50-day flucuations. Various models are presented to elucidate this relationship. The results are summarized in Chapter V.

II. Global Properties of 40- to 50-day Oscillation: A Review of the Literature

II.1 Introduction

In this chapter I will focus on the global-scale properties of the 40- to 50-day oscillation in the ocean and atmosphere as established in the literature to date. (This contrasts with Chapter III where I will discuss the properties of the 40- to 50-day oscillation primarily in the locality of the source region of the Somali Current, presenting an original analysis of atmospheric and oceanic data acquired in this region).

Since Madden and Julian (1971 and 1972a) announced the discovery of the 40- to 50-day oscillation in the atmosphere, great progress has been made in elucidating the properties of this oscillation. Much less progress has been made toward the understanding of the origin of the 40- to 50-day oscillation . It is only relatively recently (Luther, 1980) that the 40- to 50-day oscillation has been positively identified in oceanic data, and little work has been done on relating this oceanic oscillation to its atmospheric counterpart.

II.2 Meteorological Background

In the introduction of this thesis I emphasized the importance of the tropical atmosphere to global meteorology. As Holton (1979) states:

> "...it is the tropics [where] the majority of the solar energy which drives the atmospheric heat engine is absorbed by the earth and transferred to the atmosphere. Therefore, an understanding of the general circulation of the tropics must be regarded as a fundamental goal of dynamic meteorology."

This absorbed radiation becomes the energy source for various instability mechanisms in the tropics. The primary energy source for these instabilities is latent heat release. This is in contrast to mid-latitude meteorological systems where the potential energy available to make disturbances grow is provided by the substantial existing horizontal temperature gradients.

The significance of tropical disturbances is illustrated by the case of Easterly (or African) waves centered at around 16°N. These waves are generated by barotropic instability of an easterly thermal wind created by the strong horizontal temperature gradient over the Sahara in Northern Hemisphere summer. Propagating westward from the zone of origin, these waves are occasionally the progenitors of tropical storms and hurricanes in the Western Atlantic. In this section I intend to focus on these tropical disturbances, and especially those of

40- to 50-day time scale. It is helpful to first discuss the general circulation of the tropics.

Lau and Lim (1982) note that

> "...at least to a first approximation, the tropical large-scale circulation, including the monsoons, can be regarded as being driven by local heat sinks and sources..."

The heat sources create large-scale vertical motion, giving rise to meridional circulation cells (Hadley cells) and east-west oriented circulation cells (Walker cells). The heat release is generally accomplished by conditional instability. That is, a moist parcel of air rising adiabatically becomes saturated at some level (cloud base) and gives rise to condensation and the release of latent heat. This heat warms the parcel, and if the rate of warming is greater than the lapse rate (rate of change of ambient temperature), then the parcel will continue to rise (pseudoadiabatic ascent) and release latent heat, thus experiencing conditional instability.

At the largest scale, the entire tropics are a heat source, giving rise to the Hadley circulation illustrated in Fig.II.1. The area of rising air between 5° to 10°N constitutes the Intertropical Convergence Zone (ITCZ). Here, large cumulonimbus clouds ("heat-towers") carry heat from the low level of convergence to the upper troposphere in the updrafts of the cloud core. [This transported heat is then dispersed poleward,

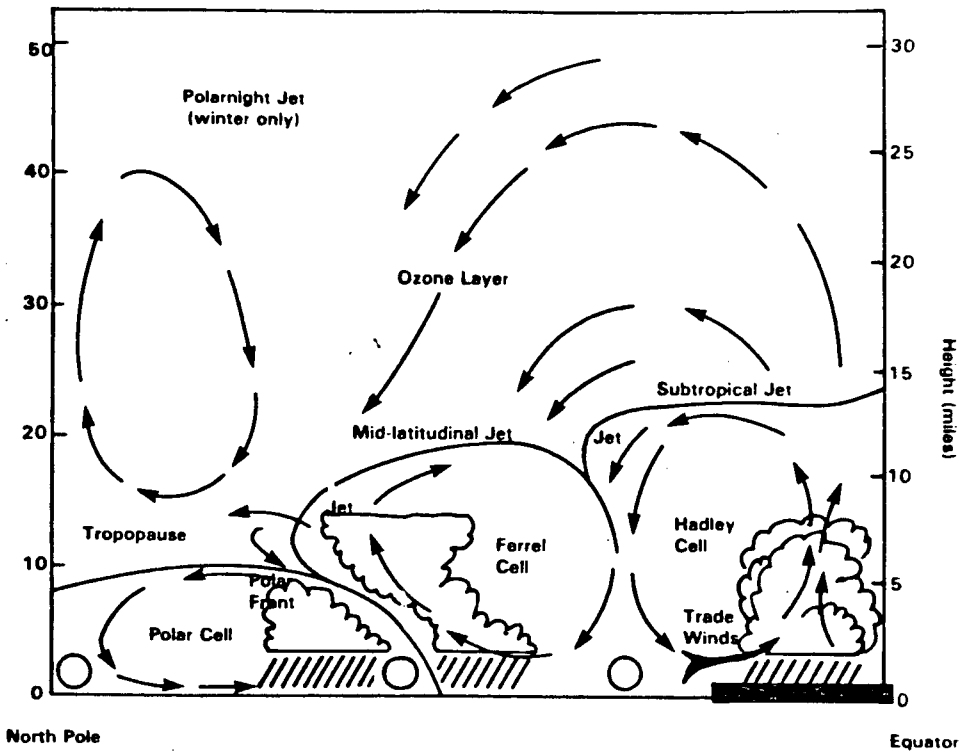

Fig. II.1. Meridional plane of a Hadley cell (from Brock,1984).

thus satisfying the global heat balance]. The ITCZ appears in satellite photographs as a series of cloud clusters with scales of the order of a few hundred kilometers. These cloud clusters are associated with weak wave disturbances propagating along the ITCZ.

The aforementioned local heat sources are associated with monsoon activity. The term "monsoon" is, according to Holton

(1979), "commonly used in a rather general sense to designate any seasonally reversing circulation system". Further,

> "Most tropical regions are influenced to some extent by monsoons. However,the most extensive monsoon circulation by far is the complex circulation associated with the Indian subcontinent, producing warm wet summers and cool dry winters."

Monsoon circulation is the result of the contrast of the thermal properties of land and sea surfaces. The penetration of solar heating on land is limited (by conduction) to a depth of the order of one meter. Thus land surfaces have small effective heat capacities. The ocean, in contrast, is mixed by wind to depths of the order of 100 meters and can thus absorb a comparatively large amount of heat. In summer conditions the land becomes warmer giving rise to vertical advection over the land with consequent enhanced cumulus convection and, in turn, the release of latent heat which causes warming throughout the troposphere. The situation is illustrated in Fig.II.2. The monsoon is thus driven by diabatic (latent and radiative) heating. In the winter season the thermal contrast is opposite to that in summer, and the continents become cool and dry with precipitation found over the relatively warm oceans.

Major monsoonal heat sources include the three continents straddling the equator, i.e., South America, equatorial Africa and the "maritime continent" of Borneo and Indonesia (Lau and

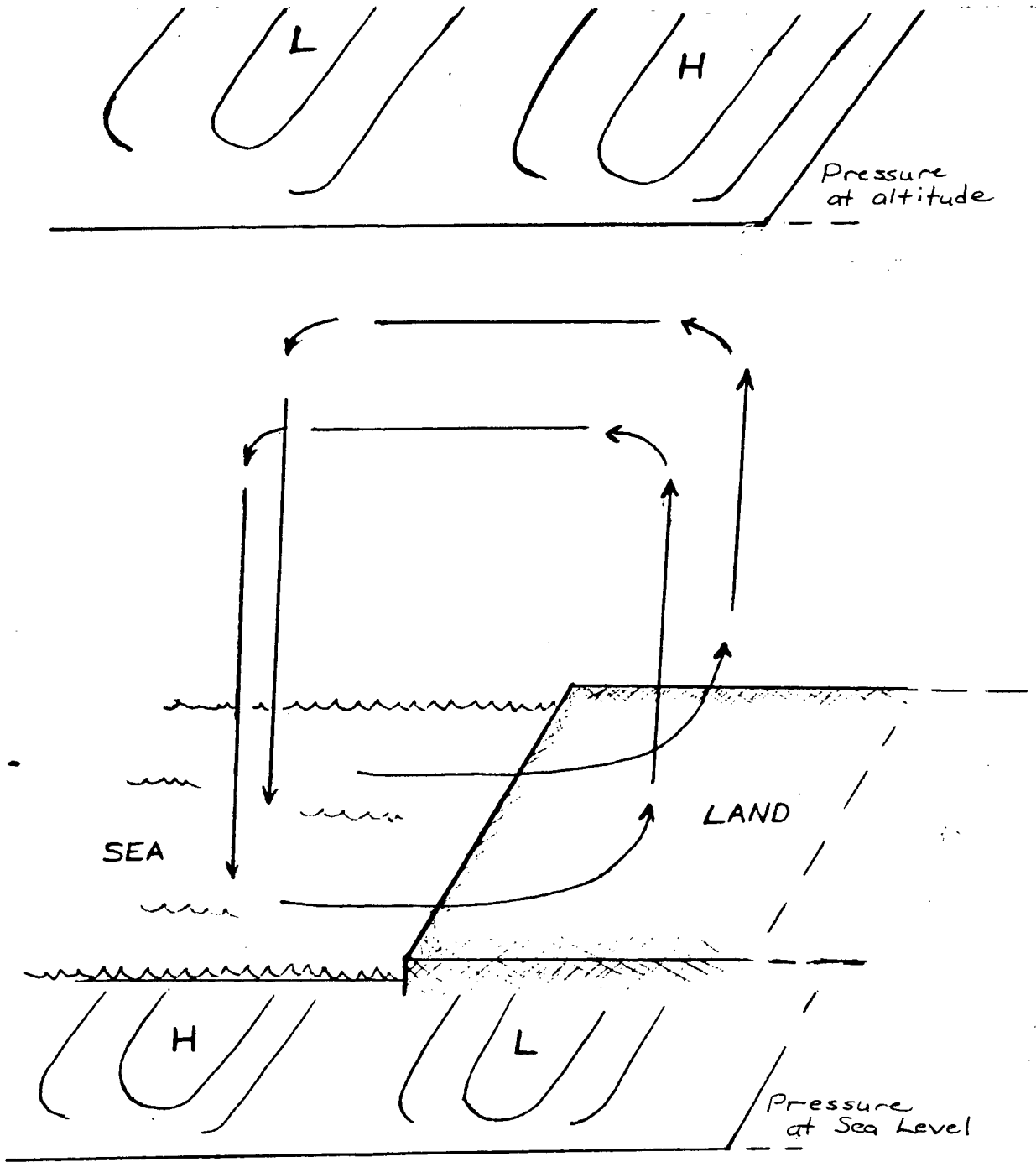

Fig. II.2. Schematic representation of a summer monsoon circulation.

Lim, 1982). The first two sources are important in Northern Hemisphere summer, while in winter the Borneo-Indonesia region

is by far the strongest of the three heat sources. It is in fact the large thermal contrast between the Borneo-Indonesia heat source and the immense cold source over northern China and Siberia which drives the East Asia winter monsoon. These sources contribute to the Walker circulation, illustrated in Fig.II.3.

Superimposed on the large scale features of the tropical circulation are certain distinct classes of disturbances. Before discussing the properties of the 40- to 50-day oscillation, I will now briefly review the information accumulated on other tropical disturbances. Boyd (1977), in reviewing equatorial waves in the atmosphere, considers the existence of 4 modes[1] to be well established:

(i) the 40- to 50-day oscillation we are interested in here. This wave is identified as a Kelvin mode of planetary wavenumber s=1 (one wavelength around the circumference of the earth $\cong$ 40,000 km).

(ii) tropospheric "5-day" waves[2] propagating as n=1 (lowest latitudinally symmetric) mode Rossby waves.

(iii) A stratospheric Kelvin wave with planetary wavenumber one to two and a period of 10-15 days.

(iv) A stratospheric mixed Rossby-gravity (Yanai) wave

---

[1] Refer to Fig. II.4 for identification of the equatorial modes in terms of their dispersive characteristics.

[2] The "5-day" waves discussed here are strictly tropical in nature and are not to be confused with the global-wide 5-day waves discussed by Madden and Julian, 1972b. The latter are westward propagating in the tropics with planetary wavenumber (as defined in (i) above) s=1, while the former are easterly waves with a planetary wavenumber of about s=12.

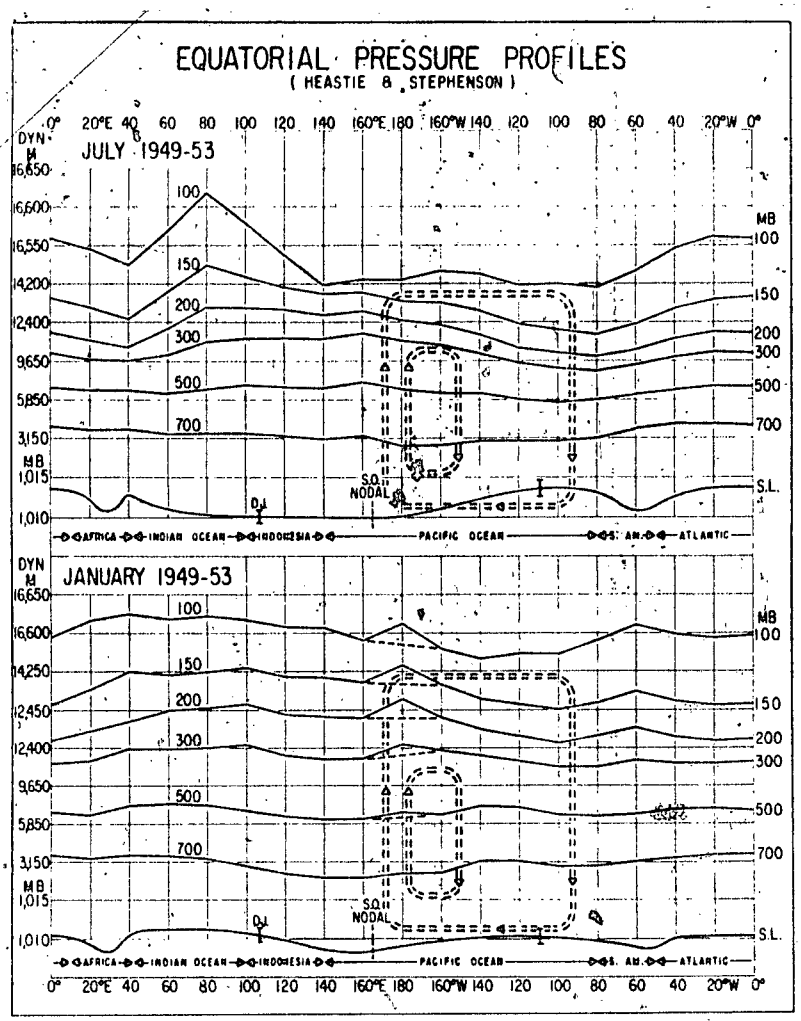

Fig. II.3. Profiles of dynamic height of standard isobaric surfaces along the equator. The Walker circulation is indicated by arrows. Note the reversal of pressure gradient with height responsible for the Walker circulation. (From Bjerknes, 1974).

of planetary wavenumber three to four and a period of about 5 days.

Boyd does not mention the observation of 3,4, and 5.5 day oscillations in sea-level records from the tropical Pacific, which correspond to the zeroes of the group velocity of the gravity modes for n=1,2,4. Also, Boyd omits reference to the

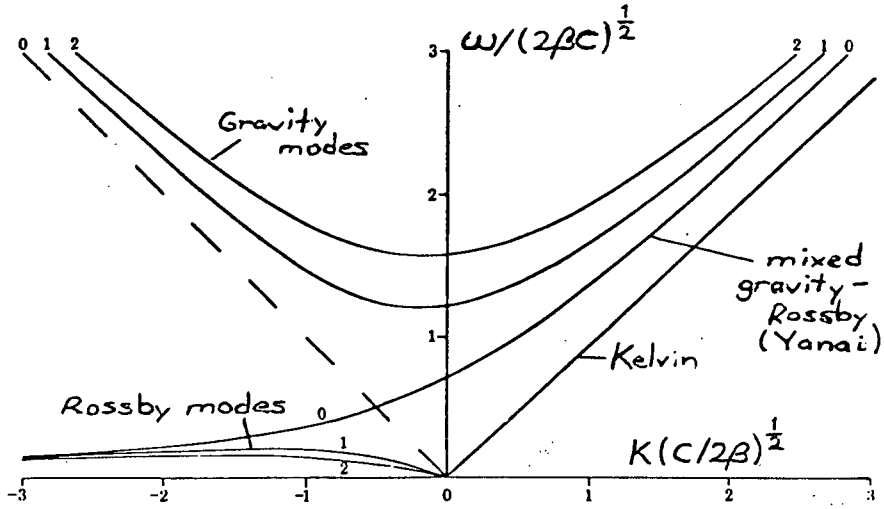

Fig. II.4. Dispersion curves for equatorial waves (adapted from Lighthill,1969).

easterly waves (discussed in the introduction to this chapter), presumably because they are not true equatorial waves, being associated with the ITCZ. The two stratospheric waves have been identified in the output of a general circulation model (Hayashi, 1974) and it is found that they are important in the general circulation: the Kelvin waves transport westerly momentum upward into the stratosphere, resulting in a westerly

acceleration of the zonal flow; the mixed Rossby-gravity waves transport sensible heat away from the equator in the stratosphere, implying an easterly acceleration of the zonal flow by the induced mean meridional circulation.

Given that the waves exist and may be important, what is their origin? Boyd (1977) suggests that the stratospheric waves are not generated by in situ instability, but rather are generated as by-products of the often vigorous weather of the tropical troposphere. Thus, understanding tropospheric dynamics should yield an accounting for all the modes discussed in this section. Holton (1979), discussing this problem, notes:

> "Some tropical disturbances probably originate as midlatitude baroclinic waves which move equatorward and gradually assume tropical characteristics. However, there can be little doubt that most synoptic scale disturbances in the equatorial zone originate in situ. Baroclinic instability cannot account for the bulk of these disturbances because, except in a few isolated regions such as North Africa and India, the meridional temperature gradient is very small. Thus, there is an insufficient source of available potential energy to account for the development and maintenance of equatorial disturbances."

Holton then goes on to discuss the role of barotropic instability in generating easterly waves. However, Holton notes that

> "Since tropical disturbances are observed to exist in the absence of strong lateral shear, it is unlikely that barotropic instability is the primary energy source for the maintenance of the waves over most of the oceanic equatorial zone."

This leaves as the only likely candidate for generating tropical waves the Conditional Instability of the Second Kind (CISK) mechanism. The notion of CISK was introduced by Charney (1964) to explain the growth of hurricanes. Charney noted that conditional instability is generally (in Holton's (1979) terminology) "released" on the scale of individual cumulus clouds, which is too small to account directly for the growth of large tropical storms. Thus, Charney suggested that a cooperative process takes place; the cumulus cell supplies heat energy to drive a (hurricane) depression, and the depression provides low level convergence of moisture to the cell in a surface Ekman layer. This positive feedback cycle apparently accounts for hurricane growth. However, a variation of this mechanism is needed to account for the existence of tropical waves , since they can exist at the equator while hurricanes cannot since as Linzden (1974) notes "the effectiveness of Ekman pumping close to the equator seems dubious." Accordingly, Lindzen (1974) has formulated a theory of wave-CISK, wherein the low-level convergence fuelling cumulus convection is provided by synoptic scale (~1000km) waves. Results of his calculation are shown in Fig.II.5. The dispersion curves correctly predict the

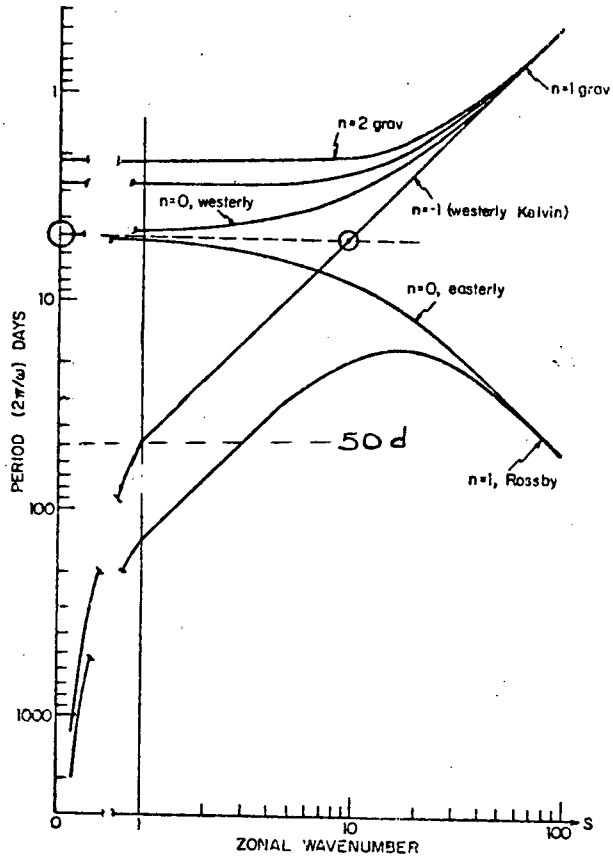

Fig. II.5. Wave period as a function of wavenumber for various wave types under conditions of neutral conditional instability of the second kind. (From Lindzen, 1974)

period of 50 days for a zonal wavenumber 1 Kelvin wave. However, Lindzen showed that the growth rate curves do not single out either this wavenumber or period, leaving the question of scale selection open.

II.3 Properties and Origin of the Atmospheric 40- to 50-day Oscillation

Kerr (1984) describes the discovery of the atmospheric 40- to 50-day oscillation as follows:

> "The 40- to 50-day oscillation was the serendipitous discovery of Roland Madden and Paul Julian (1971 and 1972a) of the National Center for Atmospheric Research (NCAR) in Boulder, Colorado. Not that it is a terribly subtle, difficult to detect phenomenon that might be swamped by all the other variability of the atmosphere. Fifteen kilometers over Canton Island in the central Pacific where the east-west or zonal wind may vary by 30 kilometers per hour from season to season, the 40- to 50-day oscillation can vary the wind over a range of 90 kilometers per hour, reversing the wind's direction in the process. In terms of wind changes, the oscillation is one-third to one-half as powerful as the changes accompanying a good-sized El Niño event.
>
> The problem with finding the oscillation was that whenever meteorologists studied a record long enough to contain a sufficient number of cycles, they usually worked with monthly averages that obliterated any sign of the oscillation. Madden and Julian stumbled on it in 1971 while broadening earlier studies of tropical atmospheric waves having periods of less than 14 days.

> They had no trouble tracing its variations in pressure and zonal wind from the Indian Ocean to the eastern Pacific and, at least at higher altitudes, all the way around the globe. They could not find any evidence of the oscillation extending much beyond 10° north or south of the equator, although they presumed such a strong oscillation must exist beyond the tropics."

Madden and Julian's (1971 and 1972a) analysis of wind and pressure variations showed the disturbance acts as a center of intensifying updraft (with corresponding clouds and precipitation) which propagates eastward from the Indian Ocean until it eventually dissipates over the eastern Pacific. This rising air would level off at the troposphere-stratosphere boundary and eventually fall back toward the lower troposphere, forming a closed circuit or convection cell (see Fig.II.6). The updraft is driven by surface heating; Madden and Julian (1972a) suggest the process is "associated with some sort of a feedback mechanism as that of sea-surface temperatures and atmospheric circulation". They were not able to definitively identify the mechanism of the 40- to 50-day oscillation .

After this pioneering work, the subject was neglected by the meteorological community for 8 years. Kerr (1984) notes that:

> "...Explanations for the hiatus vary. Madden and Julian had exhausted the available data. It was only a tropical phenomenon, at a time when many considered

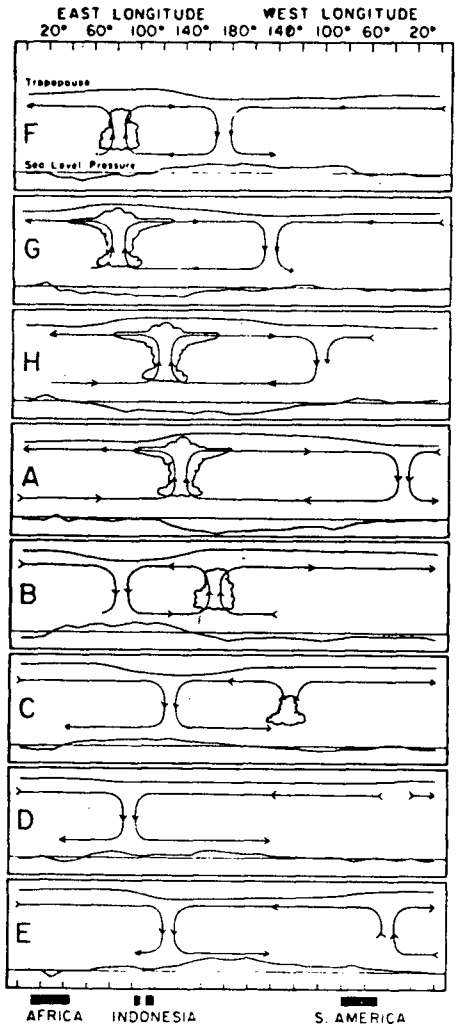

Increasing large scale convection over the Indian Ocean.

Eastern circulation cell spreading eastward.

Center of large scale convection over Indonesia.

The two circulation cells are now nearly symmetric.

Western cell is shrinking, convection weakening.

Increasingly weakened convection.

No enhanced convection remains.

Cells again symmetric.

Fig. II.6. Schematic evolution (from top to bottom) of the 40- to 50-day oscillation modifying the Walker circulation. (From Madden and Julian, 1972a).

the weather patterns of the mid-latitudes (where most meteorological research was done) and the tropics separate and independent. And fluctuations that were so much slower than day-to-day variability were not a hot topic among meteorologists.

In any case, things picked up around 1980.

Tetsuzo Yasunari (1981) of Kyoto University reported 40- to 50-day fluctuations in cloudiness over the bay of Bengal and adjacent India, prompting Julian and Madden (1981) to publish some old equatorial cloudiness data supporting their model of enhanced convection. Then Klaus Weickmann (1983) of the University of Wisconsin at Madison pointed to satellite observations of 30- to 60-day fluctuations in tropical cloudiness that tended to propagate eastward into the central Pacific.

Weickmann also found during some winters the cloudiness fluctuations were accompanied by fluctuations in the breadth of jet streams far to the north over East Asia, the North Pacific, and North America. John Anderson of the University of Illinois and Richard Rosen (1983) of Atmospheric and Environmental Research Inc., of Cambridge, Massachusetts, also found the association of tropical and mid-latitude oscillations by demonstrating that they work together through their variations in the zonal wind to slow and speed up the rotation of the earth by a few tenths of a millisecond."

Thus, a picture emerges of a tropical oscillation (equatorial circulation cells) with poleward propagating branches (as evidenced by Yasunari in the cloudiness fluctuations) which disturb mid-latitude weather systems (like the jet streams). The

tropical component with the poleward propagation has been modelled by Chang (1977) as a damped equatorial Kelvin wave in which the phase speed c depends on the damping factor D. This model explains the poleward phase propagation in the tropics. This is because the Gaussian trapping factor for equatorial Kelvin waves becomes complex when damping is included. Equation (18) of Chang (1977) takes the form

$$\exp\left(\frac{-\beta y^2}{2\hat{c}}\right) = \exp\left(-\frac{\beta}{2}\frac{c_r}{c_r^2+c_i^2}y^2\right)\exp\left(i\frac{\beta}{2}\frac{c_i}{c_r^2+c_i^2}y^2\right)$$

$$= \exp\left[-\left(\frac{y}{y_G}\right)^2\right]\exp\left(\frac{ic_i}{c_r y_G}y^2\right)$$

$$(\hat{c} = c_r + ic_i)$$

where

$$y_G = \left(\frac{2}{\beta}c_r\Big|_{D=0}\right)^{\frac{1}{2}}$$

The phase propagation is quantitatively in agreement with the observations of Madden and Julian (1972a) (see Fig. 7 in Chang (1977)). For the phase speed of the 40- to 50-day waves ($\approx$10 m/s), one finds y_G=1000 km, so that 20° from the equator ($\approx$2000 km) the wave amplitude is reduced by a factor $e^{-4}\cong 50$. Thus the tropical component clearly cannot account for the large amplitudes observed by Weickmann far north of the equator.

Various explanations have been advanced for the origin of the 40- to 50-day oscillation . Yasunari (1981) has explored the idea of a tropical-subtropical connection at a 40-day period. Yasunari's observations centered on the Monsoon active-break cycle. Active periods (heavy rain over India) alternate with break periods (less rain) at periods of about 40 days (as noted earlier, this pattern is particularly clear in cloud

observations). Yasunari notes that cloud variations over the equator occur in phase with cloud variations in the Southern Hemisphere (where a near-standing oscillation is dominant from the equator to 30°S). He suggests that the formation of major equatorial cloud disturbances over the Indian Ocean is closely linked with mid-latitude westerly disturbances and/or fronts in the Southern Hemisphere. The equatorial disturbances are in turn linked to the Indian Monsoon active-break cycles (see Fig.II.7).

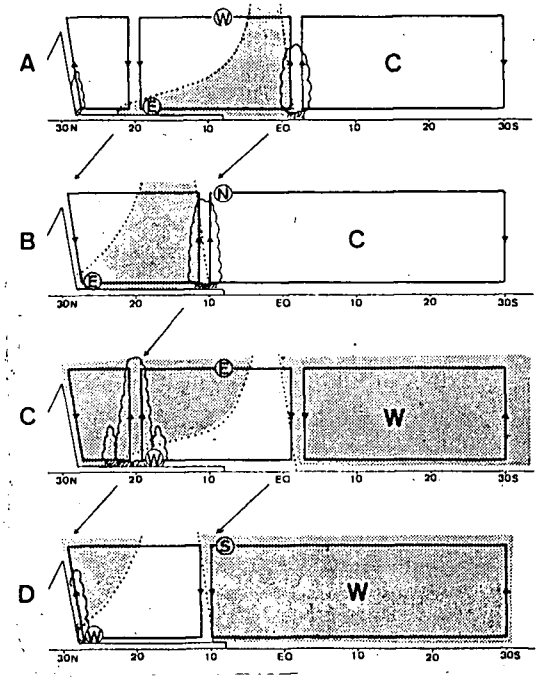

Cold air outbreak over Southern Hemisphere yields equatorial disturbances formed at the head of the cold air mass. India is dominated by a break condition.

Southern Hemisphere cell approaching India, equatorial disturbance moving eastward.

Maximum rainfall over India, Southern Hemisphere circulation changed.

Break condition over India once more- cycle starts over with outbreak from the Southern Hemisphere.

Fig. II.7. Schematic model of the 40- to 50-day period oscillation of the anomalous Hadley circulation. The maximum stage of the anomalous wind directions are indicated in the circles. Relatively warm areas are shaded. (From Yasunari, 1981).

An explanation emphasizing air-sea interaction has been offered by Goswami and Shukla (1984). Their model studies of the global atmosphere indicate that the Hadley cell may develop oscillations via its interaction with the sea. Air in the low-level, return flow toward the equator accumulates moisture from the ocean, which condenses and helps to drive the cell's circulation. The faster the air returns, the more moisture it will accumulate, further enhancing convection - but only up to a point. The returning air eventually moves through the return leg too quickly to pick up a full load of moisture, with a consequent diminution of convection. The model of this feedback process predicted the Hadley cell to oscillate with a period of between 20 and 40 days.

Anderson (1984) also believes the Hadley cell to be the source of this oscillation, but provides a model, predicting oscillations of this cell, which does not require the inclusion of moisture and condensation. In this model, the cell has a natural period between 30 and 60 days determined by the time it takes the cell's winds to carry the momentum added by a disturbance around the circuit. Neither Hadley cell mechanism explains why the disturbance propagates to the east. It is possible that Lindzen's CISK model (presented in the preceeding section; see Fig.II.5) might account for the eastward propagation of 40- to 50-day fluctuations initiated by "ringing" of the Hadley cell at its natural frequency.

I now conclude this section with a discussion of Murakami, Nakasawa, and He's (1984) analysis of the 40- to 50-day

oscillation, which will prove to be very important to the considerations of Chapter IV. In Fig.II.8 one sees the results of their analysis of phase propagation of the 40- to 50-day

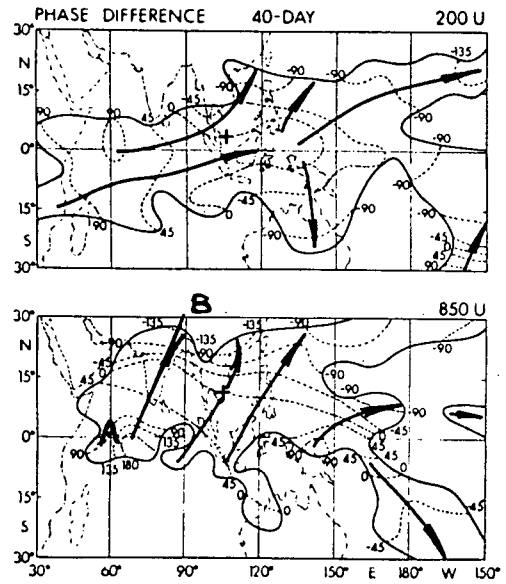

Fig. II.8. Constant phase contours (in degrees) for the zonal velocity perturbation at 200 mb and 850 mb in the Indian and western Pacific Oceans (From Murakami, Nakazawa, and He, 1984). The line AB has been drawn for purposes of wavelength estimation (see Fig.II.9).

zonal velocity anomaly over the Indian Ocean. The important result for the work here is that the 850 mb perturbations propagate roughly parallel to the African coast in the Western Indian Ocean, and that the (northward) propagation starts well south of the equator. In Fig.II.9 I have plotted the phases

shown in Fig.II.8 along line AB, as a function of distance along line AB, to establish the wavelengths of the perturbation. The estimated slope of the line gives a value of λ =3200 km; I will present an original analysis of data from the Western Indian Ocean in Chapter III which supports this wavelength estimate.

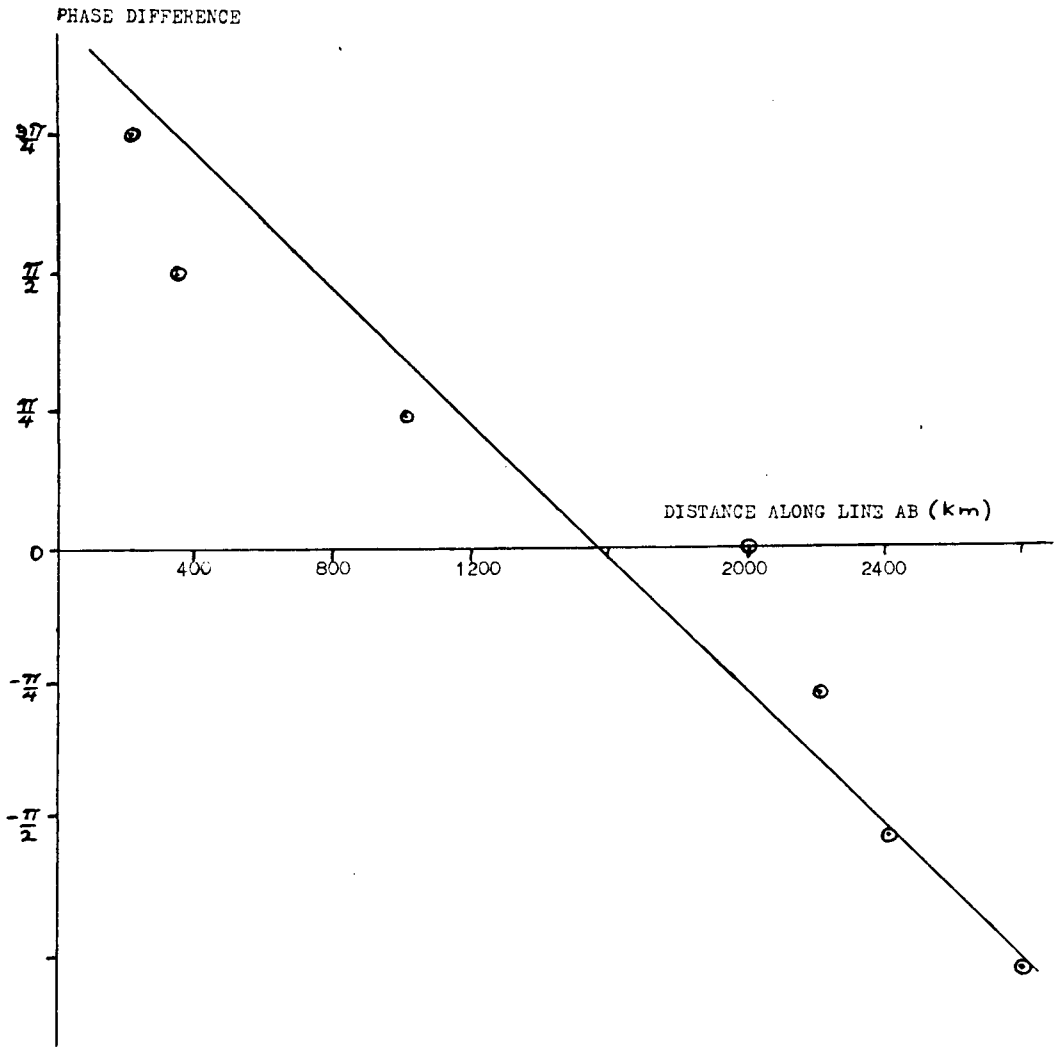

Fig.II.9. Phase difference versus distance along the line AB in Fig.II.8.

II.4 Oceanographic Background

I noted in Section II.2 that much of the tropical atmospheric circulation is driven by diabatic heating provided by land-sea temperature contrasts. These contrasts reverse seasonally and give rise to monsoon variability. The Indian Ocean, being completely bounded to the west and north by land, exhibits perhaps the most dramatic seasonal variations of any ocean. Accordingly, I will concentrate in this section on the Indian Ocean [the material of this section also provides background for the discussion of the Somali Current region given in chapter III]. Regarding these monsoonal changes, Düing (1970) has noted:

> " Since classical times it has been recognized that the winds over the northern Indian Ocean reverse semiannually. It is a well known fact that the monsoons were used to great advantage by the Greek seafarers in the first centuries A.D. in carrying out their extensive Arabian Sea trade with India. From Arabic documents of the medieval period, however, we know that the semiannual reversal of the surface currents was discovered only in the ninth or tenth century...
>
> ...The periodical reversal of the wind and of the surface circulation over such an extended area is outstanding when compared to that of the Atlantic Ocean or the Pacific Ocean. The large-scale

circulation in the northern part of the Indian Ocean (north of 20°S) has an essentially nonstationary character, whereas the large-scale circulation in the great Atlantic and Pacific gyres shows an essentially stationary behavior."

The large-scale, seasonal changes are illustrated in Fig.II.10. The maps marked February typify the Northeast Monsoon. During this period (Northern Hemisphere winter) the Northeast Monsoon winds traverse the equator to about 3°S, followed by a belt of doldrums to about 10°S, Further south, the Southeast Trade winds blow quite steadily throughout the entire year. This wind system causes a zonal current system, consisting of the North East Monsoon Current north of about 3°S, an Equatorial Counter Current between 3°S and 10°S and the South Equatorial Current south of 10°S. Water carried westward by the NE Monsoon Current flows southward along Somalia, and subsequently into the Equatorial Countercurrent located in the doldrum region. West of the northern tip of Madagascar, the South Equatorial Current branches into the southward-flowing Mozambique Current and into the northward flowing East African Coast Current. Near 2°30'S the East African Coast Current converges with the southward flowing (weak) Somali Current. This convergence zone constitutes the root of the equatorial Countercurrent. This zone shifts from year to year; southward flow has been seen as far south as Zanzibar.

The maps marked August typify the Southwest Monsoon. Under these (Northern Hemisphere) summer conditions the belt of

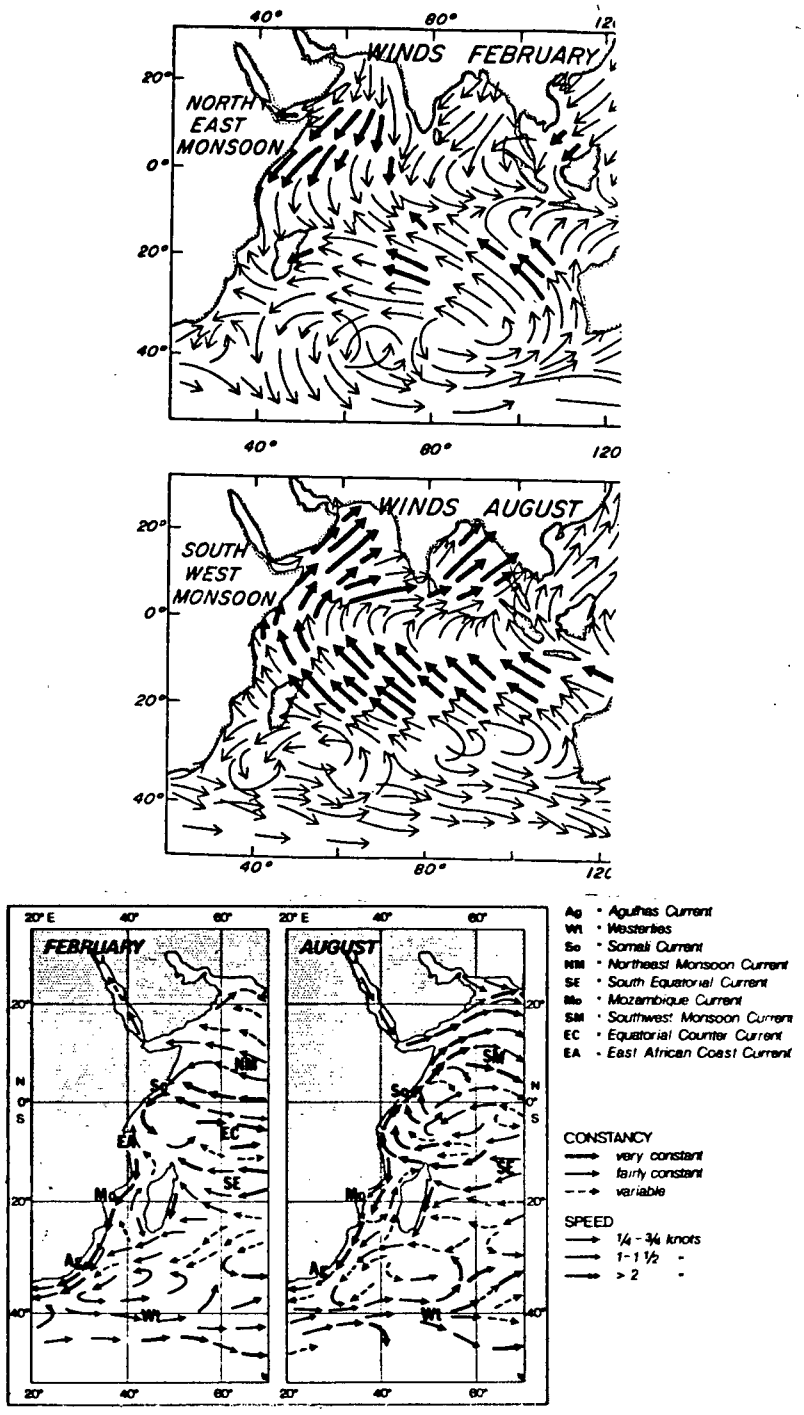

Fig.II.10. Surface winds (from Düing, 1970) and surface currents (from Düing and Schott, 1978) of the monsoon regime of the Indian Ocean.

doldrums shifts to the north, and north of the equator the winds have reversed against the winter situation toward the northeast.

The Southeast Trades have strengthened and penetrated into eastern Africa as a strong narrow jet which, blocked by high ground at its western boundary (the East African Highlands), curves into a southerly direction, across the equator, and then to a southerly jet which crosses the Arabian Sea flowing toward India. This is the Somali jet (or the East African jet). The oceanic current system now consists of the South West Monsoon Current down to about 8°S, and south of it again the South Equatorial Current. There is no Equatorial Counter Current during this season. The South Equatorial Current is stronger owing to the strengthening of the Southeast Trade winds. During both seasonal transitions (May and October) a narrow eastward equatorial jet develops. This jet is generated by westerly winds blowing in the equatorial region during the transition periods. This is the only surface current in any ocean which flows eastward at the equator. The reversal (onset) of the Somali Current south of the equator occurs about one month before the onset of the SW Monsoon over the interior of the northern Indian Ocean. Leetmaa (1972,1973) argues that this southerly onset is caused by local winds and a switching action of the East African Coast Current. Düing and Schott (1978) show that the Somali Current south of the equator sets in as a rather shallow, intense, northeastward flow extending only gradually to below the thermocline. It appears that northward flow starts at any latitude along the Somali Coast a few days after the local wind possesses a southerly component. Numerical modelling by Cox (1976) suggests that after the initial, local response the

arrival of oceanic Rossby waves, generated by the large-scale (monsoon) wind shift throughout the Indian Ocean, enhances the current buildup (the Lighthill (1969) mechanism).

II.5 Properties and Origin of the 40- to 50-day Oceanic Oscillation

There has been, to date, considerably less observational work done on the oceanic 40- to 50-day oscillation compared to that on its atmospheric counterpart. Only recently has the link between the oceanic and atmospheric oscillations been elucidated. Erikson, Blumenthal, Hayes, and Ripa (1983) have shown that the oceanic 40- to 50-day oscillation in the Pacific appears to be generated by zonal wind fluctuations with this period range. In this section I will briefly review the results of previous observational programs concerned with the oceanic 40- to 50-day oscillation .

There is little evidence for the existence of the 40- to 50-day oscillation in the Atlantic Ocean. Weisberg, Horigan, and Colin (1979) found a significant but rather broad-banded peak centered on 31 days in velocity and temperature spectra from data acquired in the Gulf of Guinea [00°01.1'N, 04°16.0'W]. These fluctuations are, however, probably generated by surface current instabilities (e.g., see Philander, 1976,1978). There are, perhaps, two reasons for this lack of evidence:

(i) The atmospheric 40- to 50-day oscillation is apparently weak over the Atlantic Ocean;

(ii) Most of the observational programs concentrating on the equatorial Atlantic (such as the GATE[3] experiments)

---

[3] GATE is the GARP Atlantic Tropical Experiment, where GARP is the Global Atmospheric Research Program.

were of relatively short duration and generally concerned with higher frequency motions.

The existence of the 40- to 50-day oscillation in the Pacific Ocean has been established by Luther (1980). In his Ph.D. thesis, Luther discusses the oceanic 40- to 50-day oscillation in some detail and finds:

(i) The atmospheric oscillation exists as an eastward propagating wave of planetary wavenumber 1 to 2.

(ii) The oceanic oscillation in the tropical Pacific Ocean is eastward propagating with a wavelength of about 11,000 km.

(iii) The 40- to 50-day sea level fluctuations from stations within 3° of the equator are not coherent with 40- to 50-day sea level fluctuations outside the equatorial waveguide.

(iv) Points (ii) and (iii) suggest that the oceanic oscillation is an equatorial Kelvin wave since the only other eastward propagating modes (inertia-gravity waves) would have sea level displacements of about 2×10^{-4}m and would thus be undetectable.

(v) Luther finds the equivalent depth (h_n) for this wave to correspond to the equivalent depth for the first baroclinic mode (n=1) in the equatorial Pacific ($h_1 = .71$m implying a phase speed of $\sqrt{gh_1} = 2.68$ m/s).

(vi) The rms amplitude of the sea level deflection (~2cm) gives a corresponding rms surface zonal current

of ~8cm/s.

There are observations of the 40- to 50-day oscillation in the Indian Ocean which may be consistent with Kelvin wave propagation. McPhaden (1981) discusses wind stress, ocean temperature and velocity time series from the island of Gan (00°41'S, 73°10'E) in the Equatorial Indian Ocean for the period January 1973 - May 1975. McPhaden concludes that "zonal winds at periods 30-60 days are highly coherent with zonal currents down to 100 m" and that "these coherence and phase structures may indicate the presence of an atmospherically forced oceanic Kelvin wave similar to that described by Luther (1980)". The power spectra of the oceanic velocity measurements are shown in Fig.II.11. Only the eastward (zonal) velocity component at 0-20m depth shows evidence of a spectral peak in the 6-12 cpy (cycles per year) band (30 to 60 days period). This feature is consistent with the notion of an oceanic Kelvin wave being responsible for the velocity fluctuations (i.e., the meridional component is very small). The power in this band (at 0-20m depth) is

$10^2 cm^2 s^{-2} cpy^{-1} \times bandwidth$

$= 10^2 cm^2 s^{-2} cpy^{-1} \times 6cpy$

$= 600 cm^2 s^{-2}$.

The corresponding velocity amplitude in this 30- to 60-day band is $\sqrt{600 cm^2 s^{-2}} \cong 25 cms^{-1}$. The implications of this large velocity will be discussed later.

Luyten and Roemmich (1982) made current measurements in the western equatorial Indian Ocean from April 1979 to June 1980.

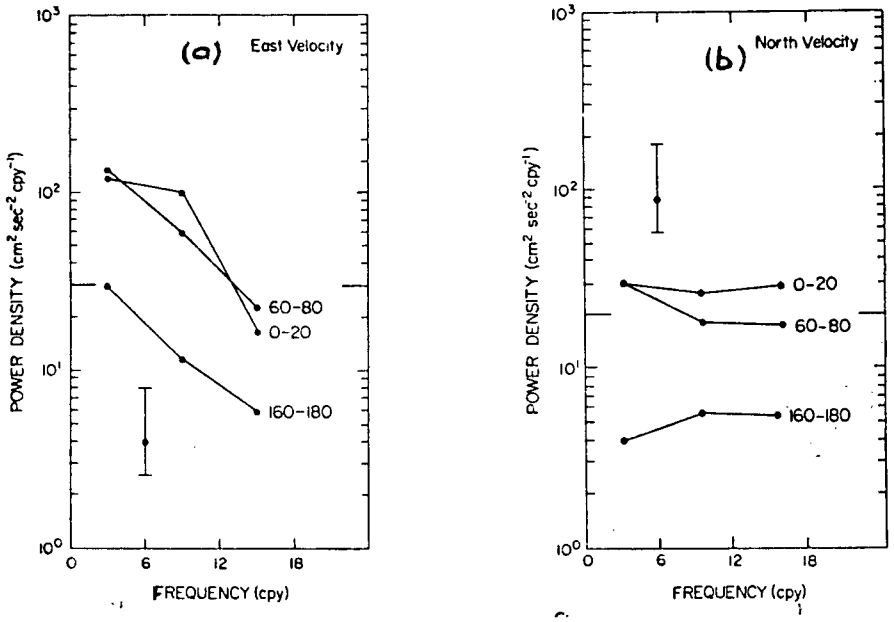

Fig.II.11. Power spectra of (a) velocity, and (b) meridional velocity, measured on the Island of Gan. (From McPhaden, 1982).

Results of these current measurements are summarized in the spectra of Fig.II.12. Referring to this figure, one can calculate the power in the 50-day band at the 200 meter depth. This power for both east (Fig.II.12a) and north (Fig.II.12c) spectra is

$$200\text{cm}^2\text{s}^{-2} \times \Delta\omega/\omega \quad (\Delta\omega \text{ is the bandwidth})$$

$$= 200\text{cm}^2\text{s}^{-2} \times 3\times10^{-7}\text{s}^{-1}/1.2\times10^{-6}\text{s}^{-1}$$

$$= 60\text{cm}^2\text{s}^{-2}.$$

The velocity amplitude corresponding to this power is $\sqrt{60\text{cm}^2\text{s}^{-2}} \cong$ 8cm/s. Note that in this case the north and east components of the velocity are approximately equal , implying that the fluctuations cannot be of a Kelvin wave nature. Reference to

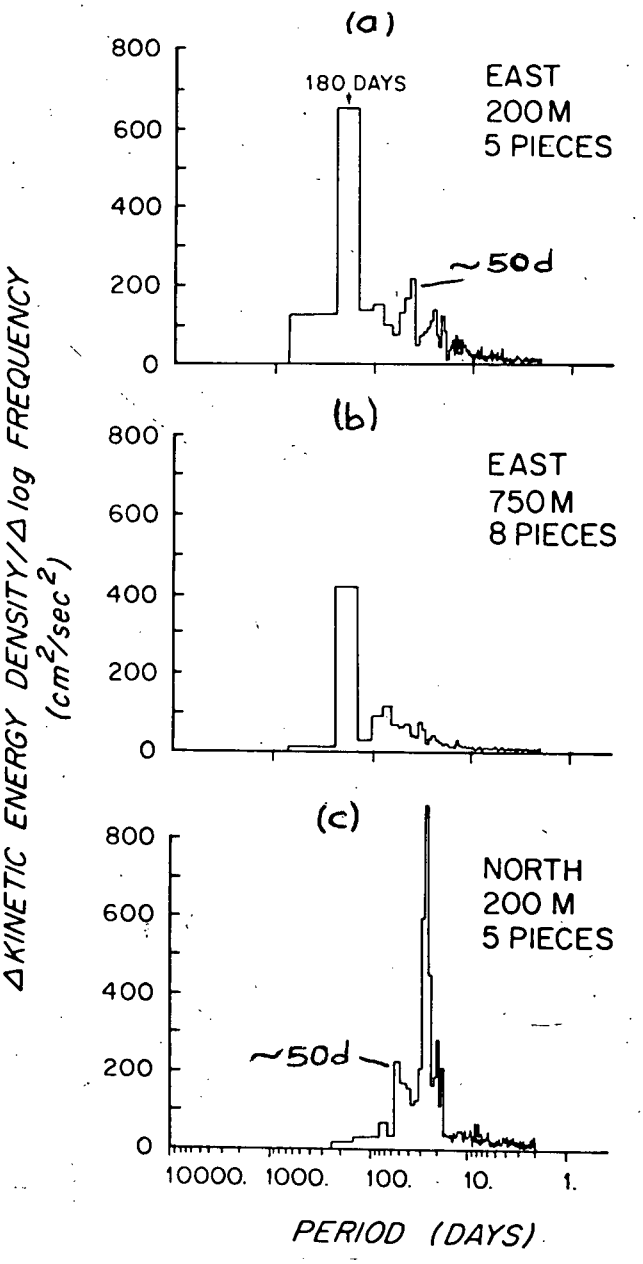

Fig.II.12. Power spectra from the Indian Ocean array for:
(a) zonal velocity at 200m,
(b) zonal velocity at 750 m,
(c) meridional velocity at 200m.
(From Luyten and Roemmich, 1982).

Fig.II.4 shows that the fluctuation observed by Luyten and Roemmich (1982) could still be eastward propagating if it is a Yanai wave ("0" mode in Fig.II.4. Near the equator, a Yanai wave

can have a zonal velocity component only if $k \cong \omega$, that is, the dispersion relation is approximately that for a Kelvin wave.

Perhaps the most remarkable observation of the oceanic 40- to 50-day oscillation is that due to Quadfasel and Swallow (1984). Their investigation, consisting of current meter measurements during 1975 (see Fig.II.13) and satellite tracking of buoys during 1976 and 1977 (see Fig.II.14). Their 1975 measurements reveal fluctuations with a 50-day period having an amplitude of 20cm/s at depths down to 500m (site "188" in Fig.II.13) and surface values of 45cm/s ! By way of comparison, the strongest current fluctuations seen in the 1976 Somali Current program were about 10cm/s at a depth of 125m (see Chapter III), at least a factor of two weaker than the currents observed by Quadfasel and Swallow. In addition to these 1975 observations, the authors have found 50-day variability of the South Equatorial Current in the tracks of satellite-tracked drifters in the interior of the Indian Ocean (see Fig.II.14) during the 1976-77 program. Evidence is presented to show that the fluctuations exhibit westward wavelike propagation (with λ =400km in the 1975 experiment, λ =1100km in the 1976-77 observations). The detection of these strong oscillations is potentially very significant in that:

(i) The westward propagating waves, upon running into the coast, could leak energy into the coastal waveguide, and these (shear and topographic) modes could be responsible for the fluctuations in the Somali Current observations discussed in Chapter III.

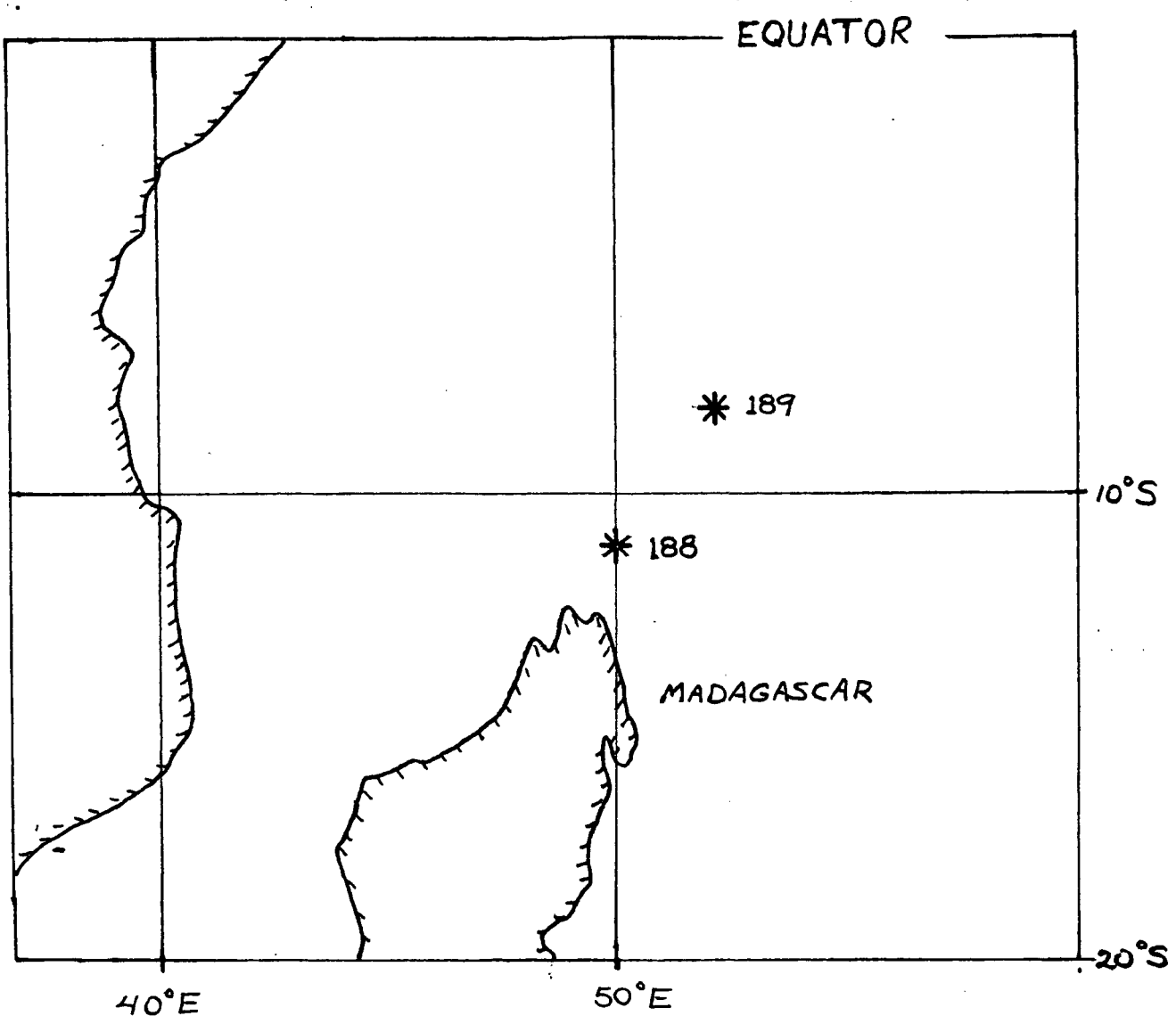

Fig.II.13. The area of Quadfasel's and Swallow's 1975 observations. Sites 188 and 189 are positions of moored current meters. (Redrawn from Quadfasel and Swallow, 1984).

(ii) Such strong current oscillations at 50-days have only been observed in the Southern Hemisphere.

This could be indirect evidence for the Southern Hemisphere origin of the atmospheric 40- to 50-day oscillations , discussed in section II (the idea of "cold surges" in the Southern Hemisphere modulating the tropical circulation).

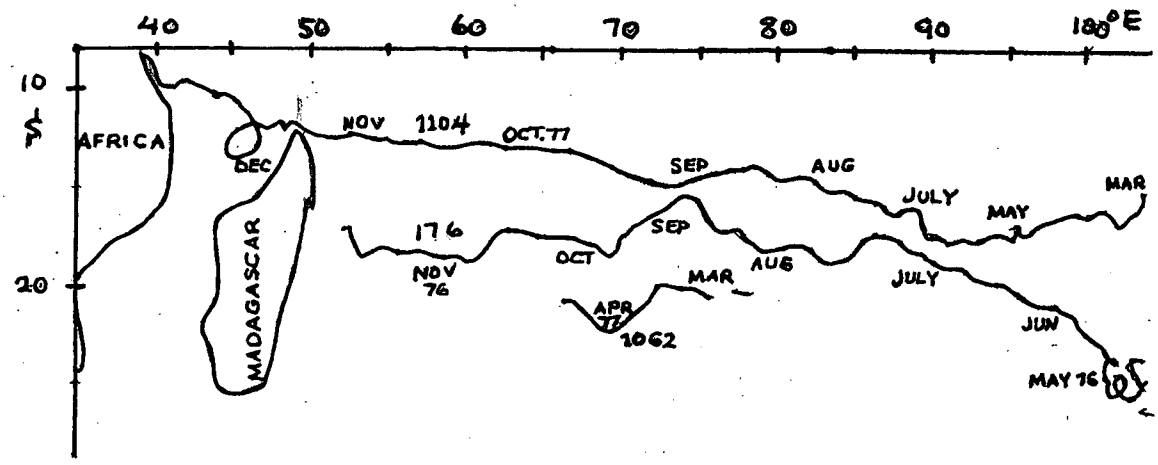

Fig.II.14. Meandering of satellite-tracked buoys in the South Equatorial Current during 1976 and 1977. The wavelength of the meanders (1000 to 1300km) corresponds to about a 50-day oscillation at the average drift speed of the buoys. (From Quadfasel and Swallow ,1984).

A possible explanation for the strength of the noted current fluctuations lies in the material presented in the meteorological observations discussed in Chapter II. It was noted that the tropical component of the 40- to 50-day oscillation can be modelled as an equatorial Kelvin wave (Madden and Julian, 1971; Chang, 1977). That is, the zonal velocity of the wind (u) satisfies

$$u = u_o e^{-\left(\frac{y}{y_o}\right)^2} \qquad \text{(II.1)}$$

where y_o is the width of the gaussian envelope estimated by Chang to be about 1000km (Section(II.3)). Thus the zonal wind stress is given by

$$\tau^{(x)} = \rho_{AIR} C_D u^2 = \rho_{AIR} C_D u_0^2 \exp\left[-2\left(\frac{y}{y_0}\right)^2\right]$$
$$= \tau_0 \exp\left[-2\left(\frac{y}{y_0}\right)^2\right] \qquad \text{(II.2)}$$

(C_D is a drag coefficient, $\tau_0 \equiv \rho_{AIR} C_D u_0^2$)

Thus the wind stress curl is given by

$$curl_z \underset{\sim}{\tau} = -\frac{\partial \tau^{(x)}}{\partial y} \qquad \text{(no meridional component of } \underset{\sim}{\tau} \text{)}$$

$$= 4 \frac{y}{y_0^2} \tau_0 \exp\left[-2\left(\frac{y}{y_0}\right)^2\right]$$

$$= (curl_z \underset{\sim}{\tau})_0 \left(\frac{y}{y_0}\right) \exp\left[-2\left(\frac{y}{y_0}\right)^2\right] \qquad \text{(II.3)}$$

where $(curl_z \underset{\sim}{\tau})_0 = 4\tau_0 / y_0$

Note that relatively weak (10cm/s) curent fluctuations are observed off the Kenyan Coast at $y=y_s=250$km (see Chapter III). Denoting the strength of the wind stress curl at this point by C_s , I find

$$(curl_z \underset{\sim}{\tau})_0 \frac{y_s}{y_0} \exp\left[-2\left(\frac{y_s}{y_0}\right)^2\right] = C_s \qquad \text{(II.4)}$$

Since $\exp\left[-2\left(\frac{y_s}{y_0}\right)^2\right] = \exp\left[-2\left(\frac{250}{1000}\right)^2\right] \tilde{=} 1$, one has

$$(curl_z \underset{\sim}{\tau})_0 = \frac{y_0}{y_s} C_s \approx 4 C_s \qquad \text{(II.5)}$$

Arbitrarily setting $C_s=1$, I now plot the theoretical wind stress curl (Equation (II.3)) as a function of latitude in Fig.II.15a.

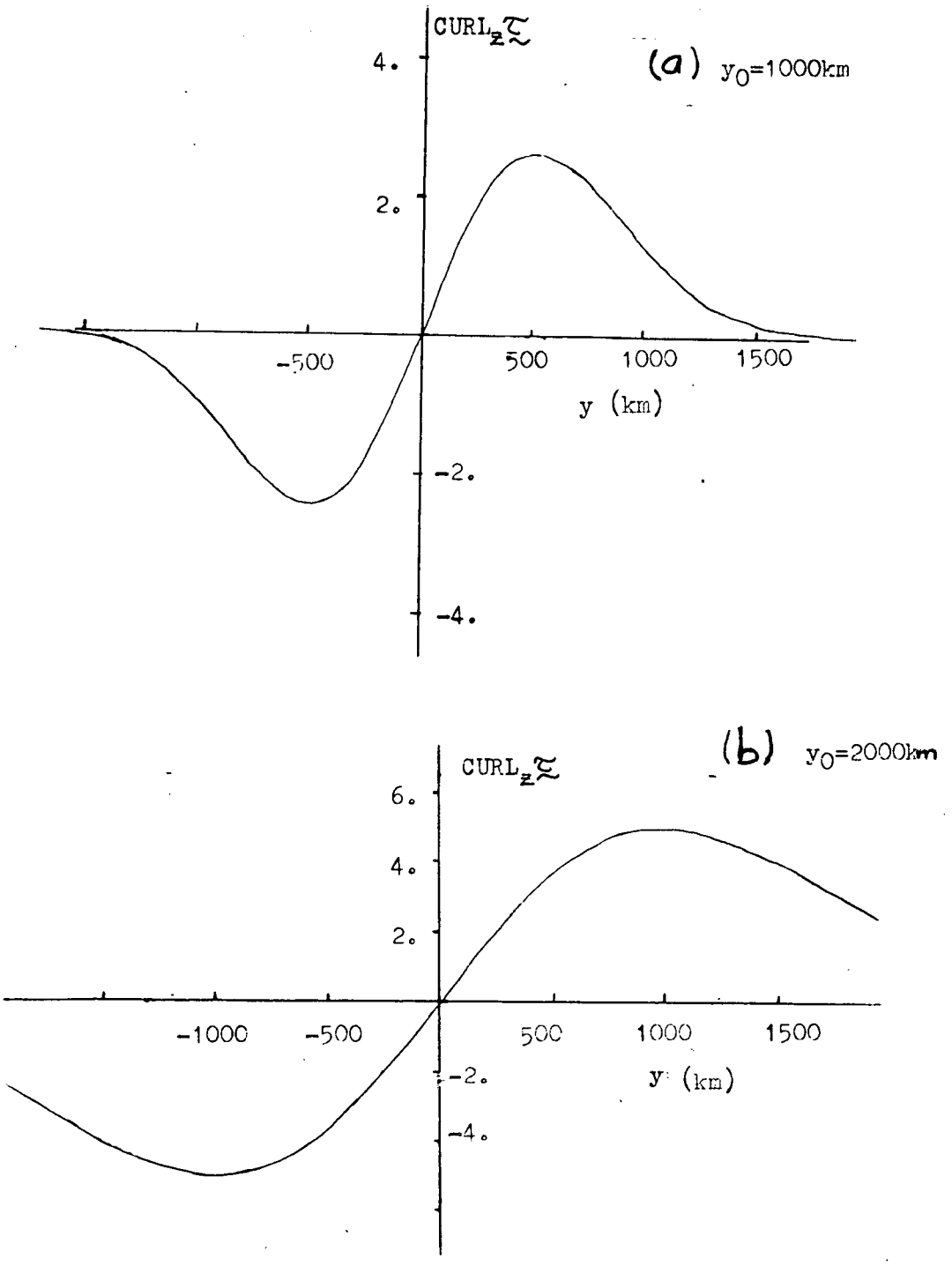

Fig.II.15. The theoretical wind stress curl specified by equation(II.3) for (a) y_o=1000km, and (b) y_o=2000km.

Note that the peak wind stress curl value occurs at y/y_o=0.5 (about 5°S) and at this peak the curl is more than twice as

strong as it is at the point of observation (y_s). Further, if I take y_o =2000km (possibly not inconsistent with the rough estimate of y_o provided by Chang), then

$$\left(curl_z \tilde{\tau}\right)_o = \frac{y_o}{y_s} C_s \cong 8 C_s \qquad \text{(II.6)}$$

and Fig.II.15b results. Now, the peak occurs closer to $y/y_o = 1$ (about 10°S) with a strength of over 5 times the value off Kenya. Wind stress curl strengths of this magnitude might explain the strikingly large oceanic current fluctuations (up to 45cm/s) observed by Quadfasel and Swallow. Further, with y_o=2000km, the belt of peak wind stress curl lies at about the same latitude as the strong current oscillations observed by Quadfasel and Swallow.

In the next chapter I will examine some equatorial measurements which support the idea that an atmospherically forced equatorial Kelvin wave gives rise to observed current and sea-level fluctuations. The extremely energetic disturbances seen by Quadfasel and Swallow could be the ultimate source of the equatorial oscillation via a leakage from the westward propagating South Equatorial Current oscillations into the coastal waveguide, from where the coastal oscillations leak into the equatorial waveguide. I will discuss this notion in more detail later.

Another set of observations which, however, cannot be explained by an equatorial Kelvin wave model are those due to

Hayes (1979). Hayes observed benthic currents in the tropical north Pacific Ocean (see Fig.II.16). He found that current meters 30m above the bottom (at depths of about 2500 fathoms)

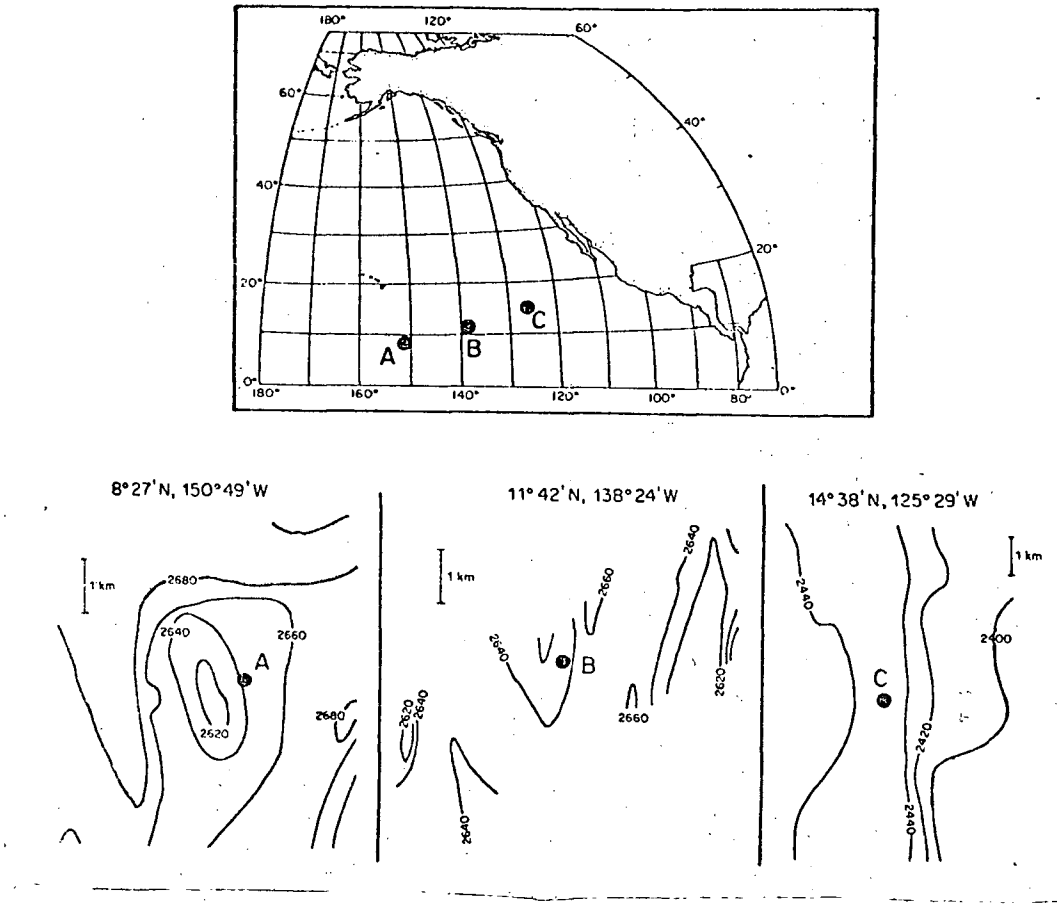

Fig.II.16. Locations of moored current meters in the tropical Pacific Ocean with nearby bathymetry. Contours are in fathoms. (From Hayes, 1979).

detected a near 50-day oscillation strong enough that "...low frequency fluctuations dominated all the records. These fluctuations had dominant periods for the meridional component of two months at all sites...". Specifically, relatively little 50-day energy was found at site A, while 50-day fluctuations of 2 to 3cm/s amplitude were found in the meridional component of

the velocity at sites B, C, with the zonal velocity component at 50-days very weak. Since the 50-day fluctuations are found in mid-ocean well outside the equatorial waveguide (which Luther estimates to be about 3° wide) dynamics other than Kelvin wave must be invoked to explain these observations. I will return to this point in Chapter IV.

III. The 40- to 50-day Oscillation in the Source Region of the Somali Current during 1976 and 1979

III.1 Introduction

In this chapter the emphasis changes from global-scale to an examination of the oceanic and atmospheric 40- to 50-day oscillations near the source region of the Somali Current (2°S, 42°E). This region has been of longstanding interest to oceanographers due to the annual reversal of the Somali Current (and thus considerable amounts of data have been gathered there). From the point of view of a study of the 40- to 50-day oscillation, this region is also of great interest. For example, the Western Indian Ocean is a region of strong land-sea contrast, which is important in driving monsoons and other convective phenomena. The Indian Ocean and/or the Western Pacific Ocean are thought to be the origin of the 40- to 50-day oscillation, so it is important to determine what happens to the oscillation on the western boundary of the Indian Ocean. A large mountain range which lies near the east coast of Africa (the East African Highlands) is known to profoundly affect the general atmospheric circulation of the region and likely also affects the atmospheric 40- to 50-day oscillation in this region. The coast itself must modify the propagation of any oceanic 40- to 50-day fluctuations here, making an analysis of oceanic data from this region distinct from the earlier work. In previous studies, the 40- to 50-day oscillation has been

examined in "unbounded", mid-ocean equatorial regions.

III.2 The 40- to 50-day Oscillation over the Western Indian Ocean during 1976 and 1979

In this section I will present new evidence of the 40- to 50-day atmospheric oscillation. This evidence comes from an analysis of data contained in Fernandez-Partagas and Düing (1977), and Fernandez-Partagas, Samuels and Schott (1980). The 1977 report contains one hundred three-day surface wind maps, as shown in Fig.III.1, extending from January to October 1976. These wind maps were compiled primarily from wind reports from ships (on record at the U.S. National Climatic Center, Asheville, North Carolina), and were supplemented with coastal and island station reports. The Western Indian Ocean is best covered, due to the presence of tanker lanes off the African Coast. The maps were compiled to aid in the understanding of the oceanic Monsoon processes, as represented by data accumulated in various INDEX studies. The analysis presented in this thesis is motivated by the observation of the 40- to 50-day oscillations in the Somali Current in its source region (3°S,41°E) during 1976. Accordingly, Southern Hemisphere wind data were analyzed on the grid (points A,B,C,D,E) shown in Fig.III.1. The 1980 report contains ninety three-day wind stress maps (covering January to September 1979) which were analyzed at different spatial locations (see points A',B',....H' in Fig.III.2). In both cases I will analyze the zonal and meridional components of the wind stress. The spectra are calculated via the maximum

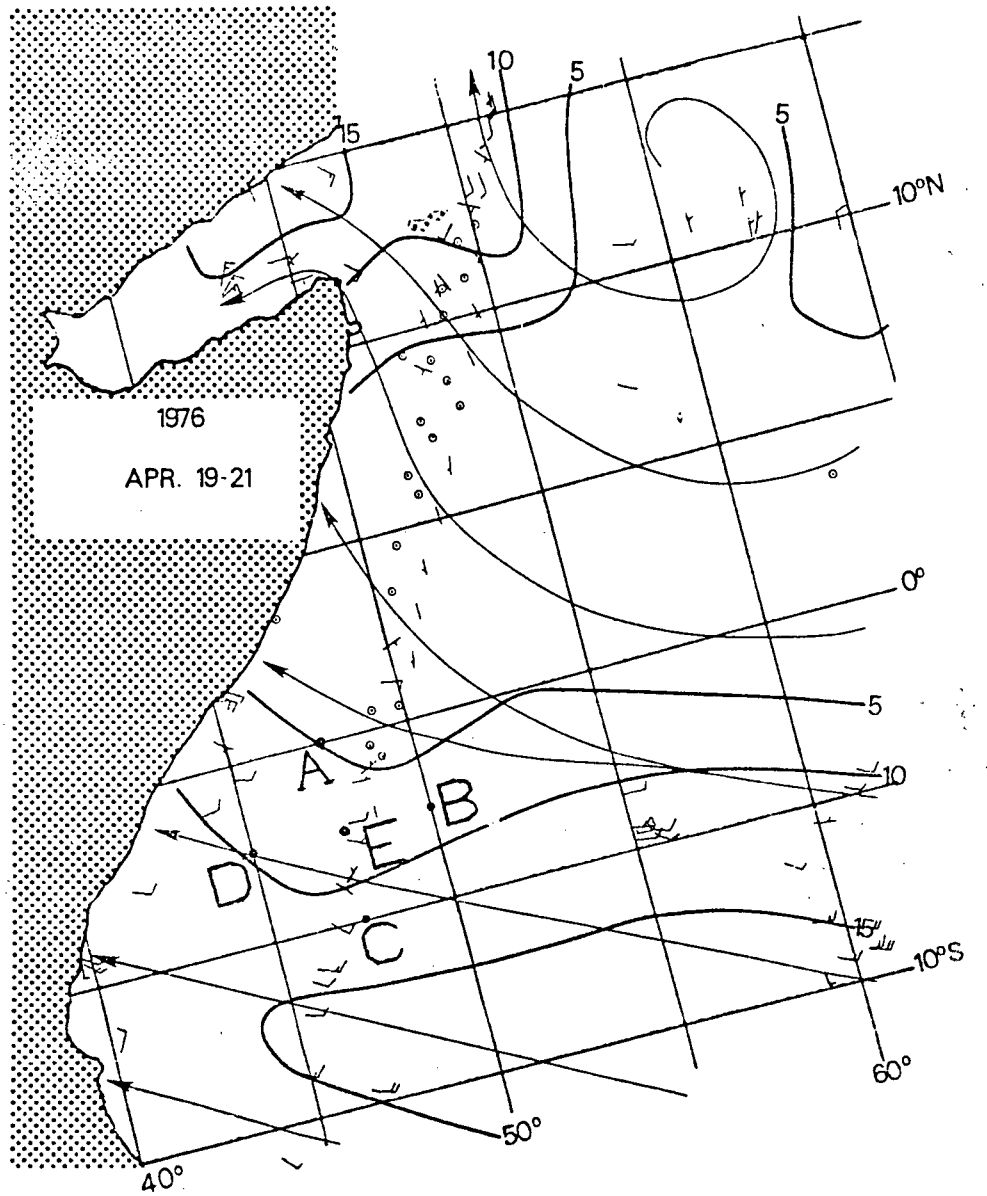

Fig.III.1. Sample surface wind map from Fernandez-Partagas and Düing (1977). Isotachs are in knots.

likelihood technique, as is discussed in Appendix I.

The grid (A,B,C,D,E) in Fig.III.1 was used to calculate the zonal and meridional components of the wind stress at each of the points A, B, C, D, E and the curl of the wind stress (and

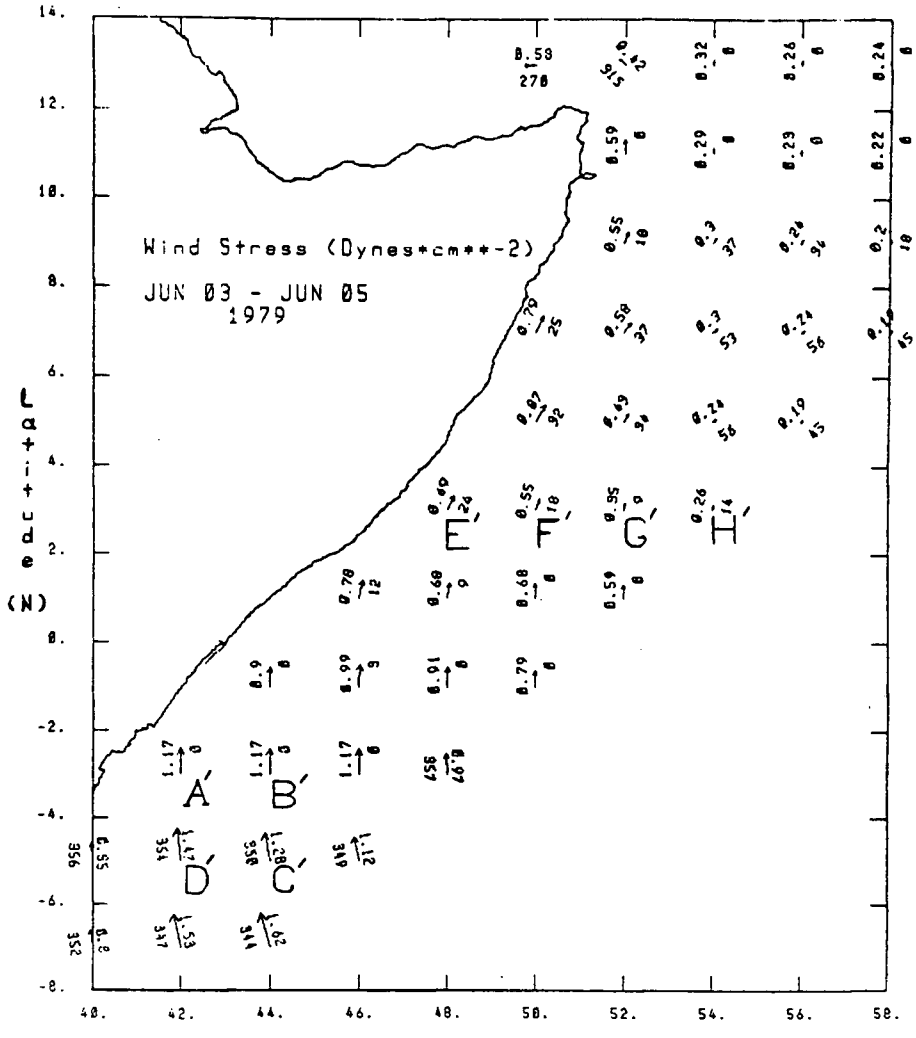

Fig.III.2. Sample surface wind stress map from Fernandez-Partagas, Samuels and Schott (1980). Arrows indicate the wind stress at each point on the 2° grid; the wind stress magnitudes are in dynes/cm², the directions (forward) are given in degrees from true north.

its spectrum) at the point E. The wind stress curl calculation is based on a finite difference approximation on the grid A,B,C,D,E specified by the formula

$$curl_z \tau \approx \frac{\tau_B^{(y)} - \tau_D^{(y)}}{\Delta_{BD}} - \frac{\tau_A^{(x)} - \tau_C^{(x)}}{\Delta_{AC}}$$

where $\tau_A^{(x)}$ is the x-component of the wind stress at point A, etc., Δ_{BD} is the separation between points B and D, and Δ_{AC} is the separation between the points A and C. Time series of the zonal and meridional stress components for the point E are shown in Fig.III.3a,b. The long period trends (seasonal or Monsoonal effects) are removed via a spline-fit routine, and the resulting de-trended time series are analyzed. The corresponding spectra are shown in Fig.III.4a,b. The only major peak in the zonal wind stress is at 60 days, which roughly corresponds to the 40- to 50-day oscillation found by Madden and Julian (1971, 1972a). As expected there is no significant 60-day energy in the spectrum of the meridional component of the wind stress. I find the same results at each of the points A, B, C, D; that is, a strong peak near 60 days for the zonal component with little or no energy at this time scale in the meridional component of the wind stress. The wind stress curl also shows a strong peak in this same frequency regime (Fig.III.5). Madden and Julian (1971) present evidence of a modulation in the amplitude of the 40- to 50-day oscillation with a noticeable increase in amplitude (in Fig.III.6) in January to April of the years 1961, 1962, and 1964. I have investigated this possibility by low passing the zonal stress and stress curl records (with a cutoff period of 25 days). The results, shown in Fig.III.7, do indicate the presence of a modulation; this is particularly evident in the low-passed wind stress curl record during days 100 to 200.

I have also analyzed the 1979 data, illustrated in Fig.III.2. Initially, I analysed data on the grid A', B', C', D'

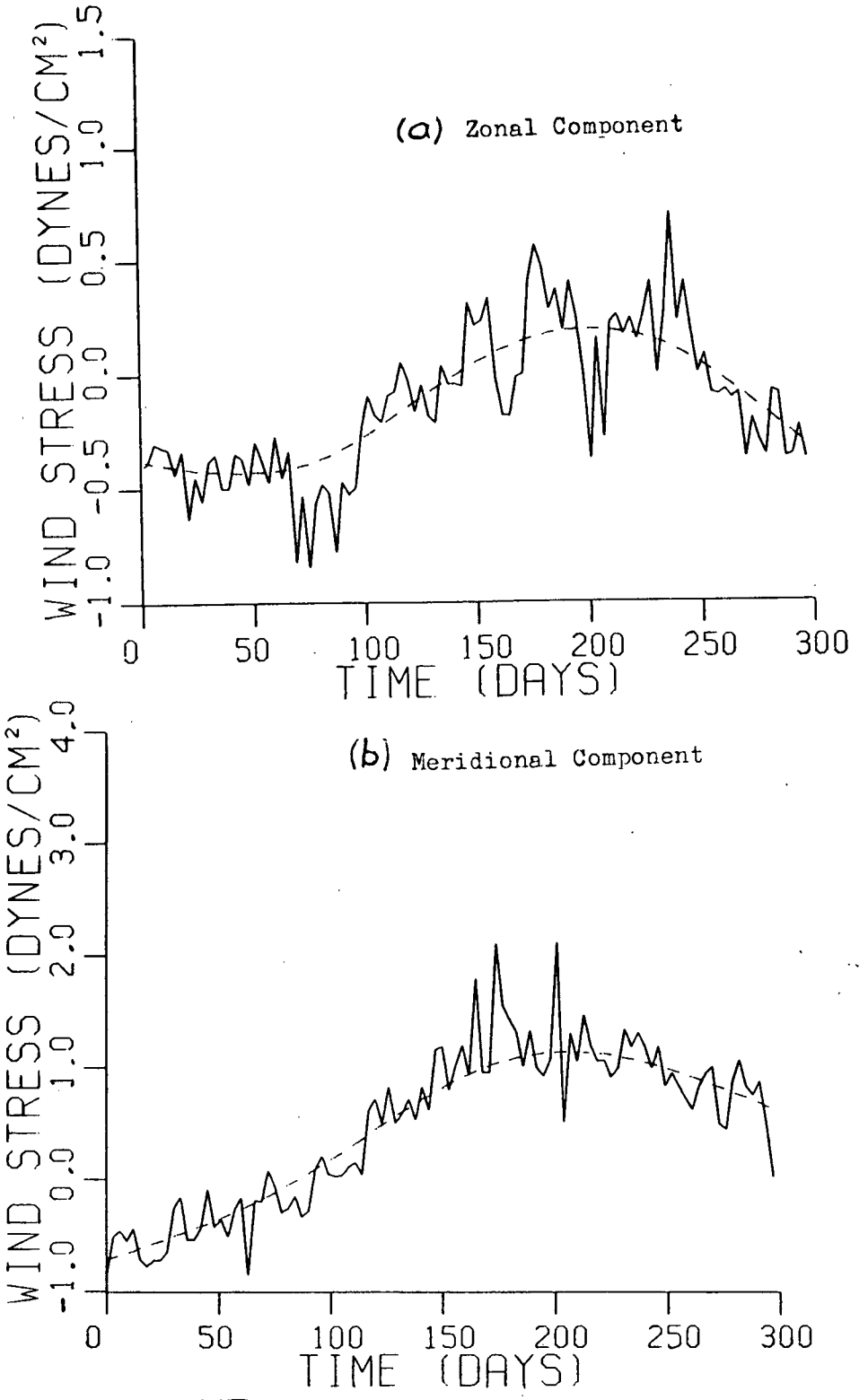

Fig.III.3. Components of the wind stress field at point E. Dashed lines represent a spline-fit to the mean stress field.

(of Fig.III.2), in a similar spatial region as the grid in Fig.III.1. However, it proves difficult to obtain good zonal

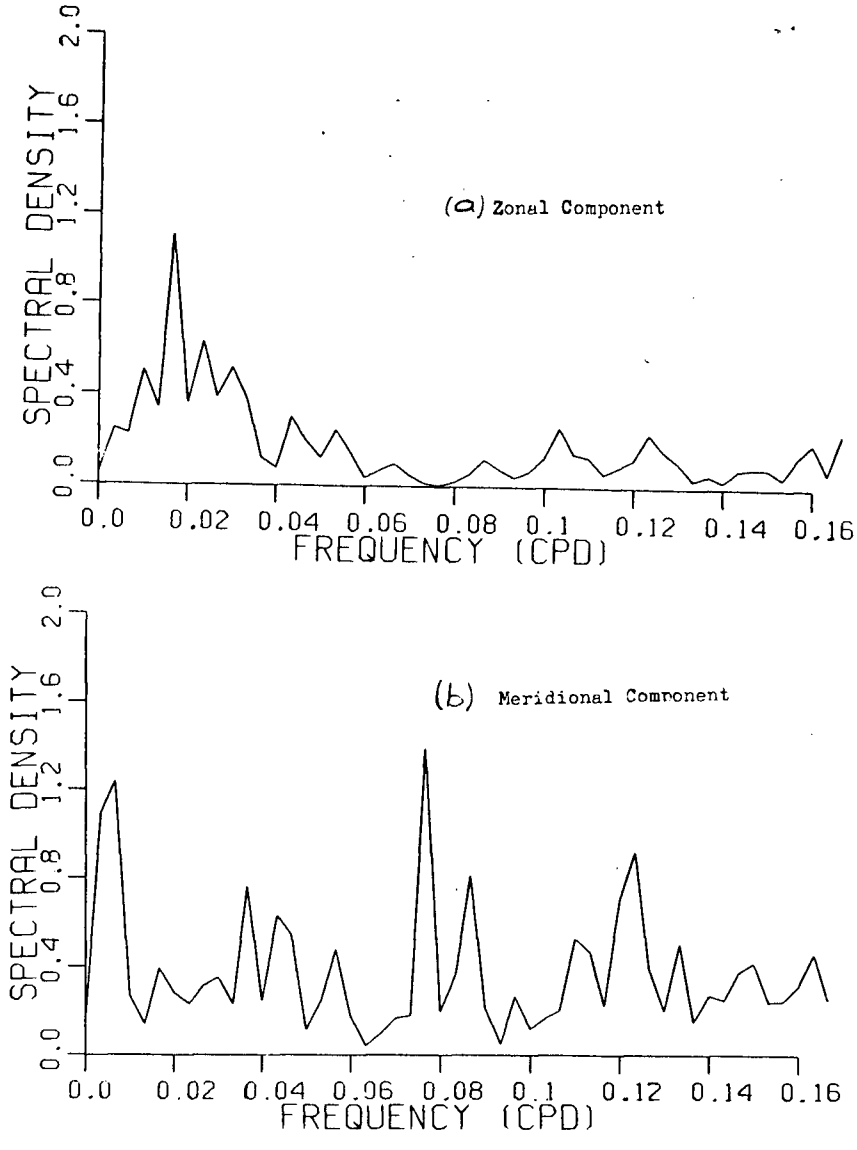

Fig.III.4 Autospectra of the components of the wind stress field at point E. The spectral density is in units of $(\text{dynes/cm}^2)^2/\text{cpd}$. For a discussion of confidence limits, see Appendix I.

spectra in this region, because the wind blow is almost meridional during large parts of the record, and when the wind

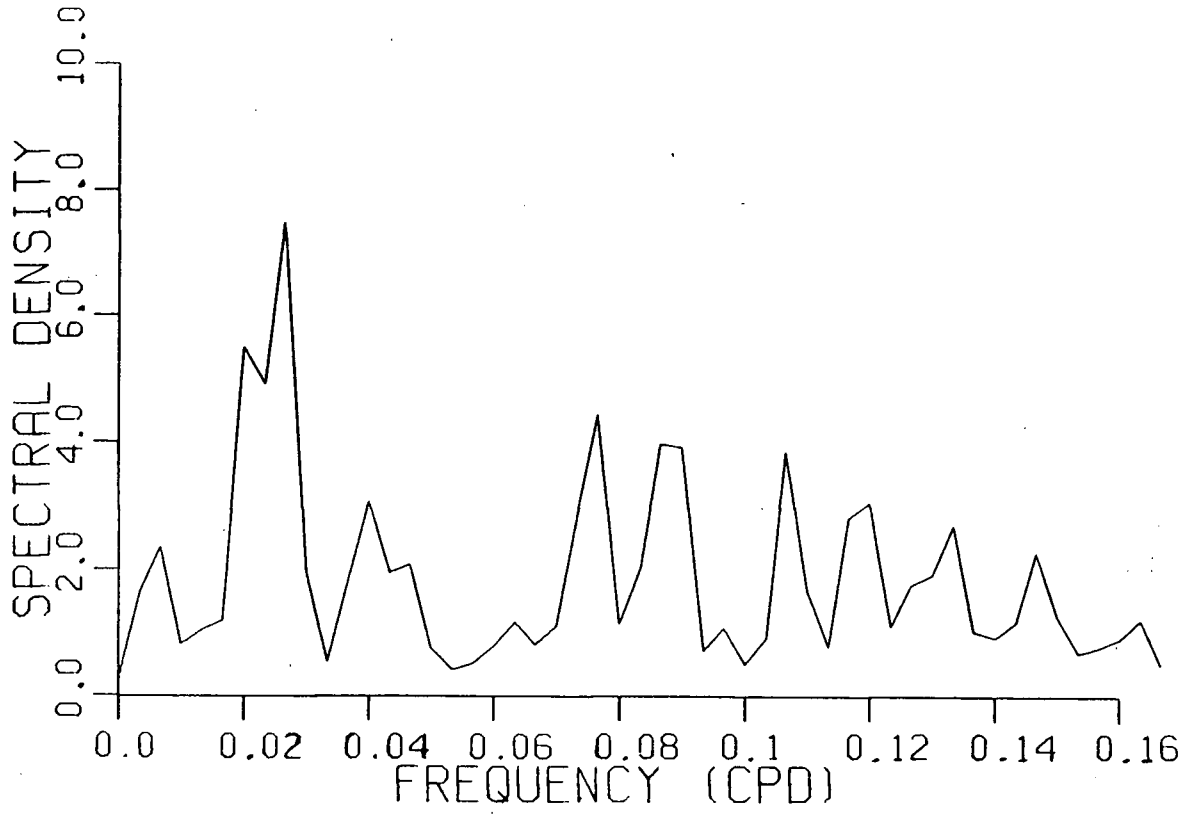

Fig.III.5. Autospectrum of the curl of the wind stress calculated about point E. The spectral density is in units of $10^{-14}(N/m^3)^2$/cpd.

is near north, there seems to be a tendency to round out the direction to zero degrees (due north). That is, angles of zero degrees are over-represented in the record, resulting in large "flat spots" in the zonal wind stress record. Good zonal records can, however, be obtained in more northern regions, where the wind almost always has a strong zonal component. Accordingly, I analyzed the stress components at the points E', F', G', H' of Fig.III.2 (which are still relatively near the equator). The resulting spectra are shown in Fig.III.8a,b,c,d for points E' and H'. The 40- to 50-day oscillation now appears somewhat more broad-banded, but it still dominates the zonal spectra.

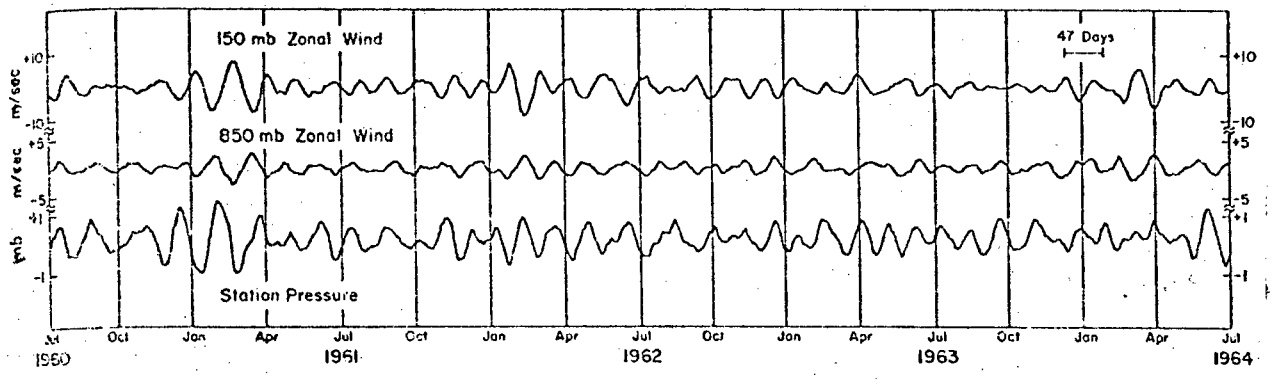

Fig.III.6. Zonal wind and station pressure from Canton Island treated with a 47-day band pass filter. (From Madden and Julian, 1971).

Surprisingly, I find a strong meridional component of the stress at point E'; there is little or no meridional energy evident at point H'. In fact, I find that the meridional component generally weakens in comparison to the zonal component as one moves eastward from station to station along the line E'-H'. This may indicate a deflection or distortion of the cells near the East African Highlands, which are known to affect profoundly the general atmospheric circulation in this region. In Fig.III.8(d), one sees a strong peak centered on 11 days period. This may be the oscillation described by Krishnamurti et al. (1985) as "a 10 to 20 day westward propagating wave....noted to influence monsoon activity". Finally, I examine the low-passed record of the zonal wind stress component from the point H', in Fig.III.9. I note that there is again an amplitude modulation during days 100 to 200.

In conclusion, the 40- to 50-day oscillations discovered by

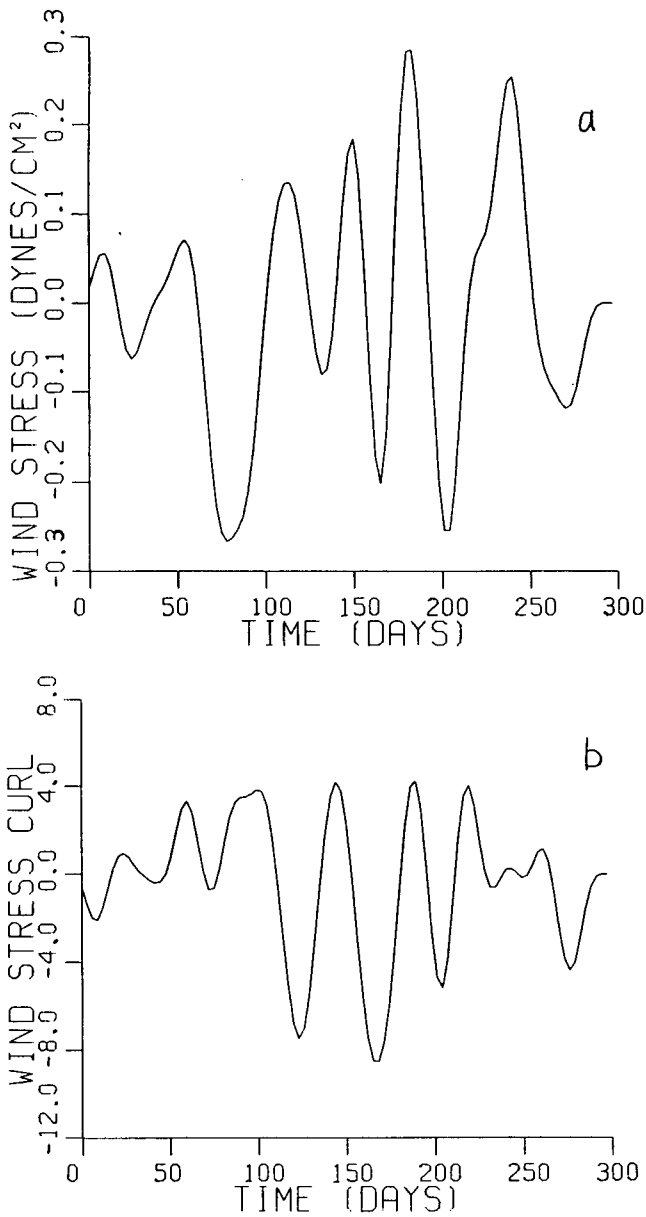

Fig.III.7. (a) Low passed wind stress record from point E.
(b) Low passed wind stress curl record (in units of 10^{-8} N/m^3).

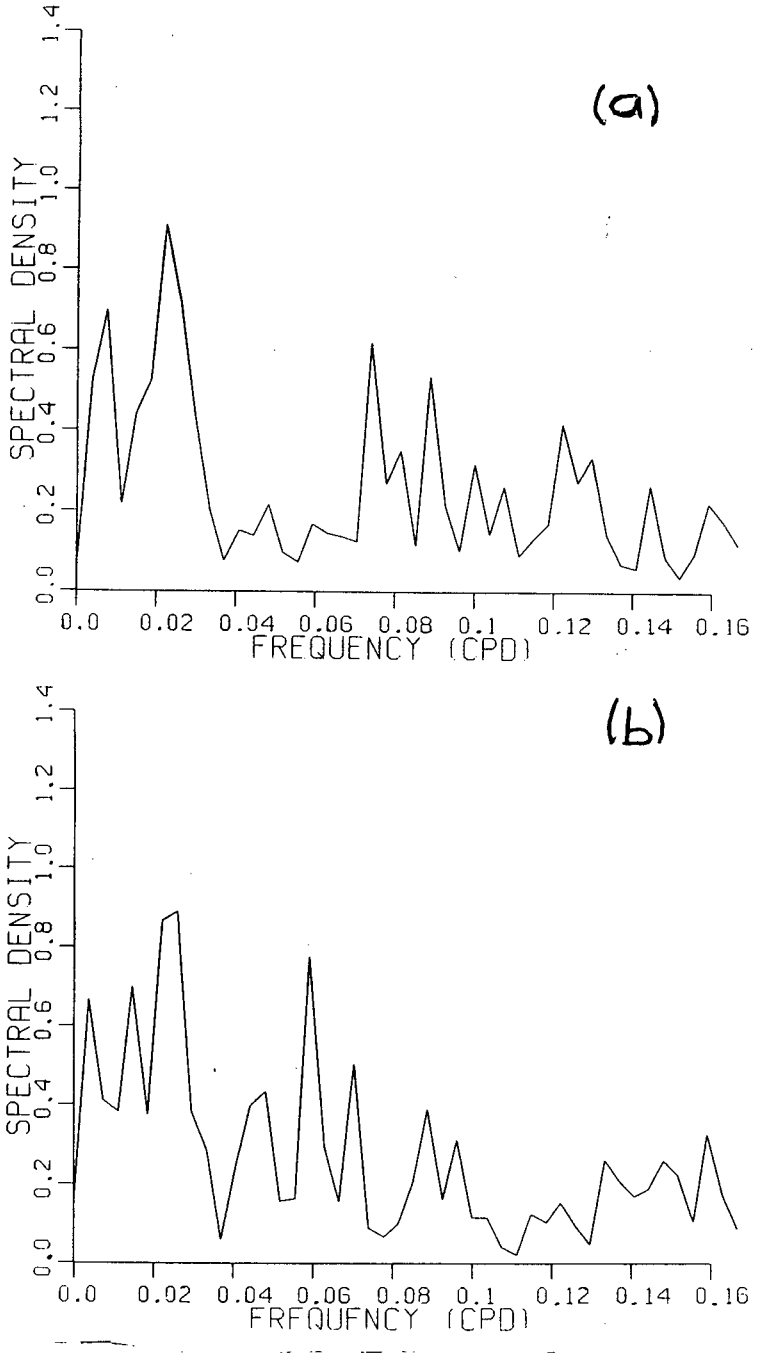

Fig.III.8. (a) Autospectrum of the zonal component of the wind stress at point E'. The spectral density is in units of $(\text{dynes/cm}^2)^2/\text{cpd}$.
(b) As in (a), except for the meridional component.

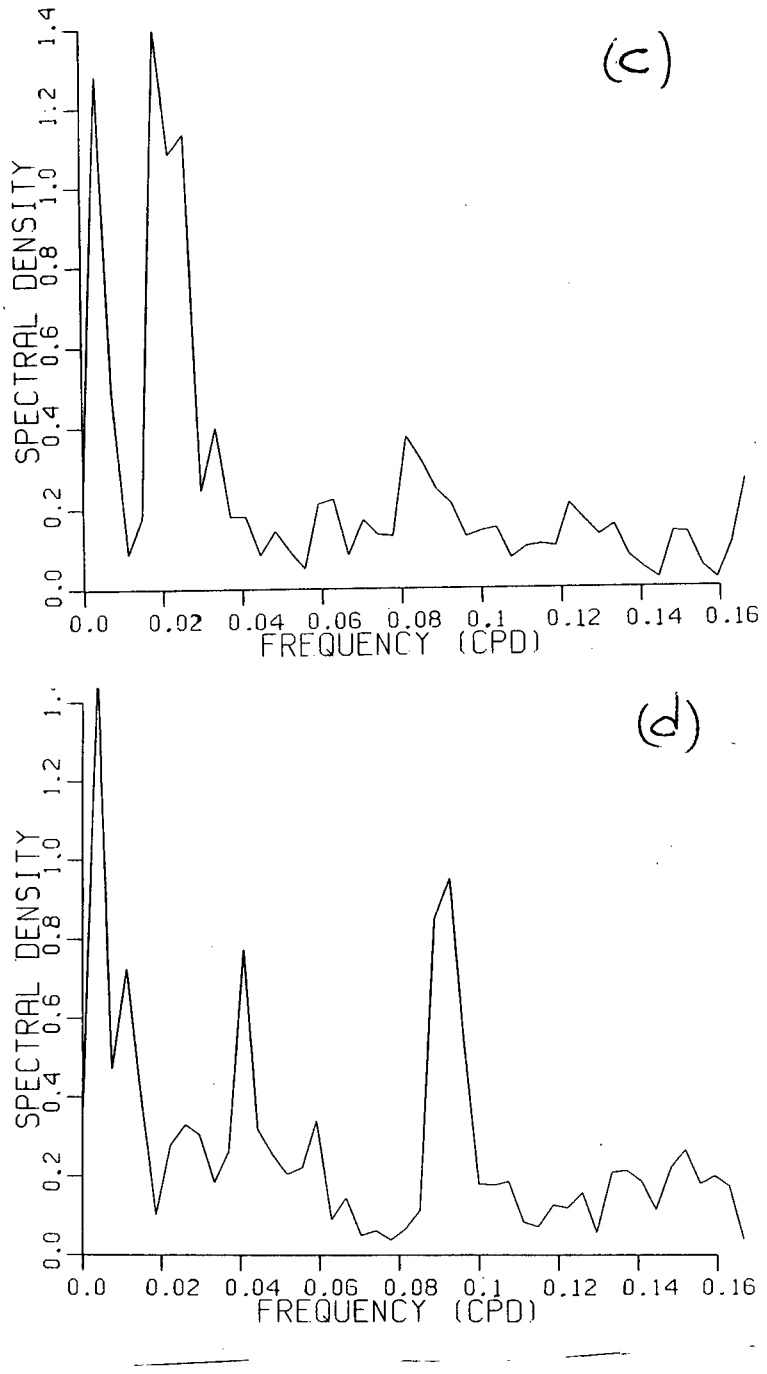

Fig.III.8 (cont.)
(c) Autospectrum of the zonal component of the wind stress at point H'. Units as in (a).
(d) As in (c), except for the meridional component.

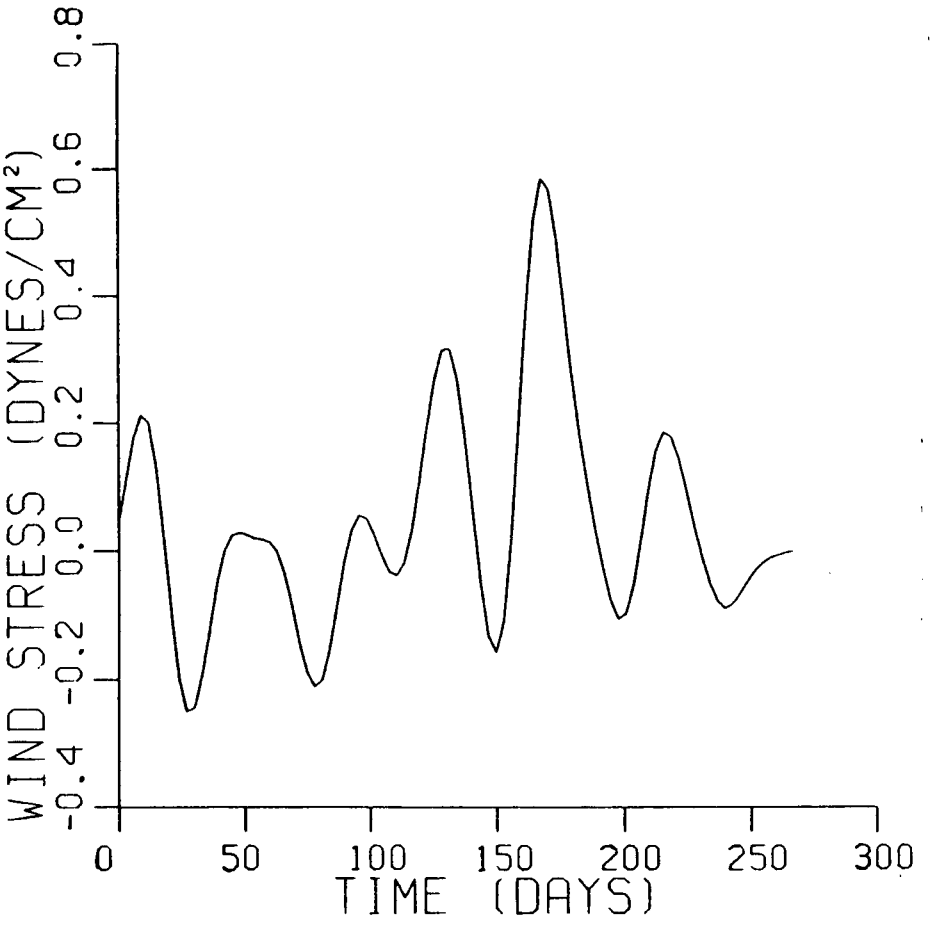

Fig.III.9. Low passed zonal wind stress record from point H'.

Madden and Julian (primarily in atmospheric data from the equatorial Pacific Ocean region for years from 1957 to 1967) were also present in the zonal wind stresses over the Western Indian Ocean in the years 1976 and 1979.

III.3 Fluctuations of the Western Indian Ocean

The world's oceans exhibit fluctuations of their characterizing fields on a wide variety of time scales. One of the most significant signals is that on the interannual time scale. The variations so described tend to be quasiperiodic in nature. For example, the Southern Oscillation-El Niño phenomenon is marked by unusually high sea-surface temperatures and rainfall and unusually weak tradewinds over the tropical Pacific Ocean, recurring at 2 to 10 year intervals. Annual variations of oceanic fields are prominent in Monsoonal regions, particularly the Indian Ocean. Fluctuations at shorter time scales are often described by relation to the local inertial frequency. At periods longer than inertial, one has subinertial fluctuations, which often propagate as waves of the second class (depending on rotation for their existence). At periods shorter than inertial, one has superinertial fluctuations, which often propagate as waves of the first class (not dependent upon rotation for their existence). In this chapter I will analyze variations of western Indian Ocean fields on annual, subinertial and superinertial timescales, with emphasis on the 40- to 50-day (subinertial) fluctuations. The discussion of the annual variations will be general, largely based on the oceanographic literature. The analysis of the subinertial and superinertial fluctuations will be based on the observations of Düing and Schott (1978) in the source region of the Somali Current.

Düing and Schott (1978) made extensive current and

temperature measurements in a region centered at 3°S and 41°E (see Fig.III.10) and extending over a six-month period (January-July, 1976) which spans the springtime monsoon reversal. During this period the large-scale (monsoon) winds change from northeast to southwest and the intense northward flowing Somali Current is formed (see Fig.III.12 below). The data used in this study were obtained from the southern moorings K1 and K2 (Fig.III.10); the mooring details are given in Table 1. A summary of the current measurements from these two moorings is given in Fig.III.11 in the form of stick diagrams, which were obtained from daily averages.

The stations K1 and K2 represent quite different regimes for three reasons:

1) The bathymetry changes considerably in going northward from K1 to K2. For example, Fig.(III.10) reveals a much greater bottom slope at K2.

2) The Coriolis parameter at K1 is about 50% larger than at K2.

3) The mean flow conditions at the two stations differ considerably (see Fig.III.11). Station K1 is located at the northern end of the northward-flowing East African Coast Current, which is relatively steady throughout the six-month observation period. At K2 on the other hand, the current is weak and variable (that is, the fluctuations are comparable to the mean) up to the middle of April. After this, in response to the Monsoon reversal, the near-surface, northward-flowing

Table 1 Details about moorings and instrument performance
(from Düing and Schott, 1978)

Mooring identification	Position and water depth	Mooring (1976) Deployed	Recovered	Instrument depths (m) Mean	Min/Max.	Pressure Yes/No	Malfunctions
K1	ϕ = 3°58.1'S	Jan 11	June 21	180	159/264	yes	rotor lost on March 13
	λ = 40°20.0'E			235		no	none
	z = 885m			445		no	vane broken on May 1
K2	ϕ = 2°46.5'S	Jan 11	July 8	125	124/128	yes	none
	λ = 41°1.3'E			176		yes	none
	z = 286m			261		no	none

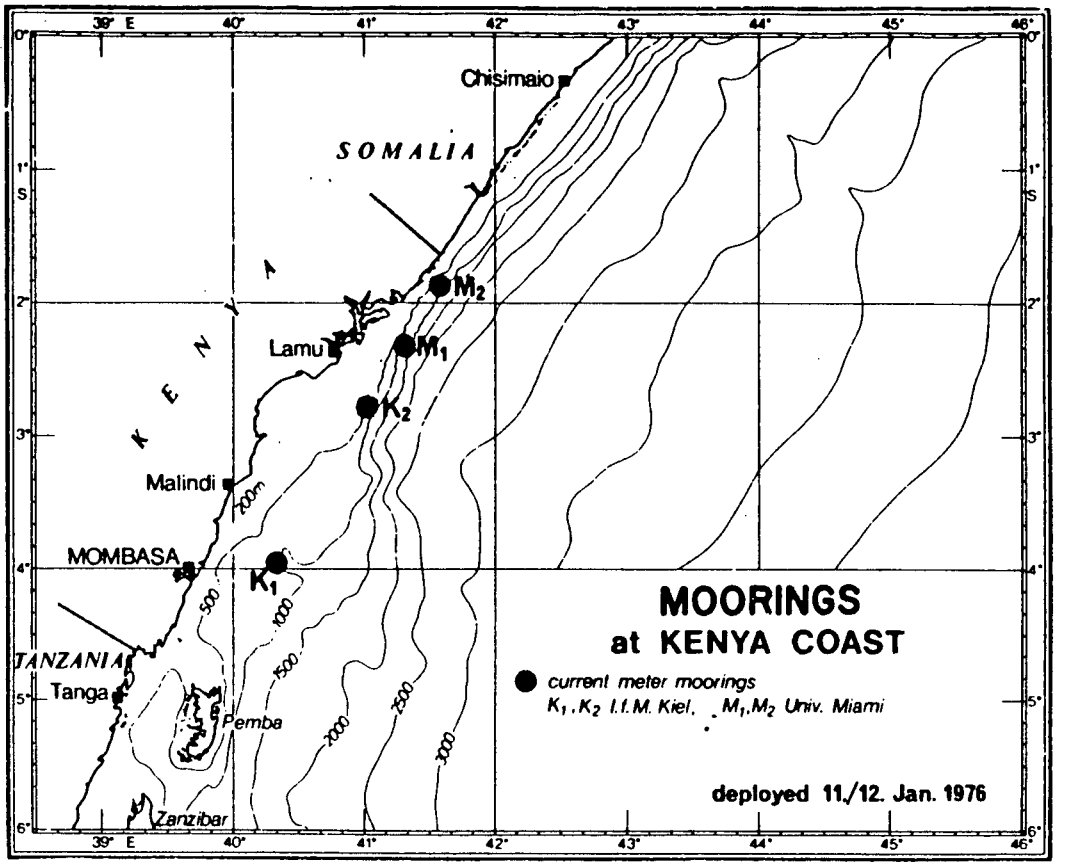

Fig.III.10. Mooring array off Kenya from mid-January to mid-July, 1976 (from Düing and Schott, 1978).

Somali Current is formed (see Fig.III.12).

Apparent in the stick diagrams of Fig.III.11 are fluctuations with time scales shorter than the seasonal variations. Autospectra of the current fluctuations show that most of the variance is at subinertial frequencies, with distinctive peaks at around 50 and 17 days. The analysis of the wind stress data contained in Fernandez-Partagas and Düing

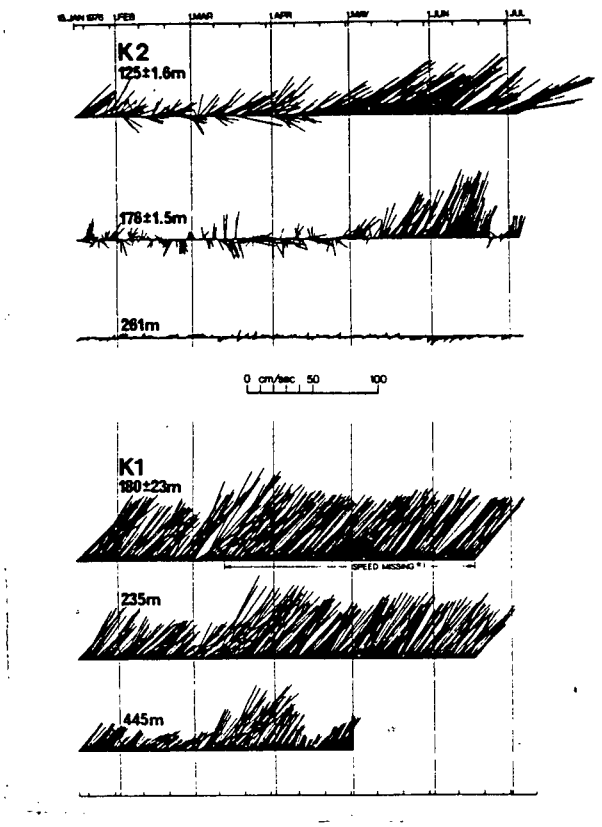

Fig.III.11. Vector time series of currents at locations K2 and K1. Vectors point in direction of flow with north upward. Average depth and standard deviation of individual sensors are indicated. For cases where the speed is missing an asterisk indicates that the values are obtained from regression with speed record at level below (from Düing and Schott, 1978).

(1977) indicates that the 50-day oceanic signal is probably forced by wind fluctuations of this time scale (see Fig.(III.1)).

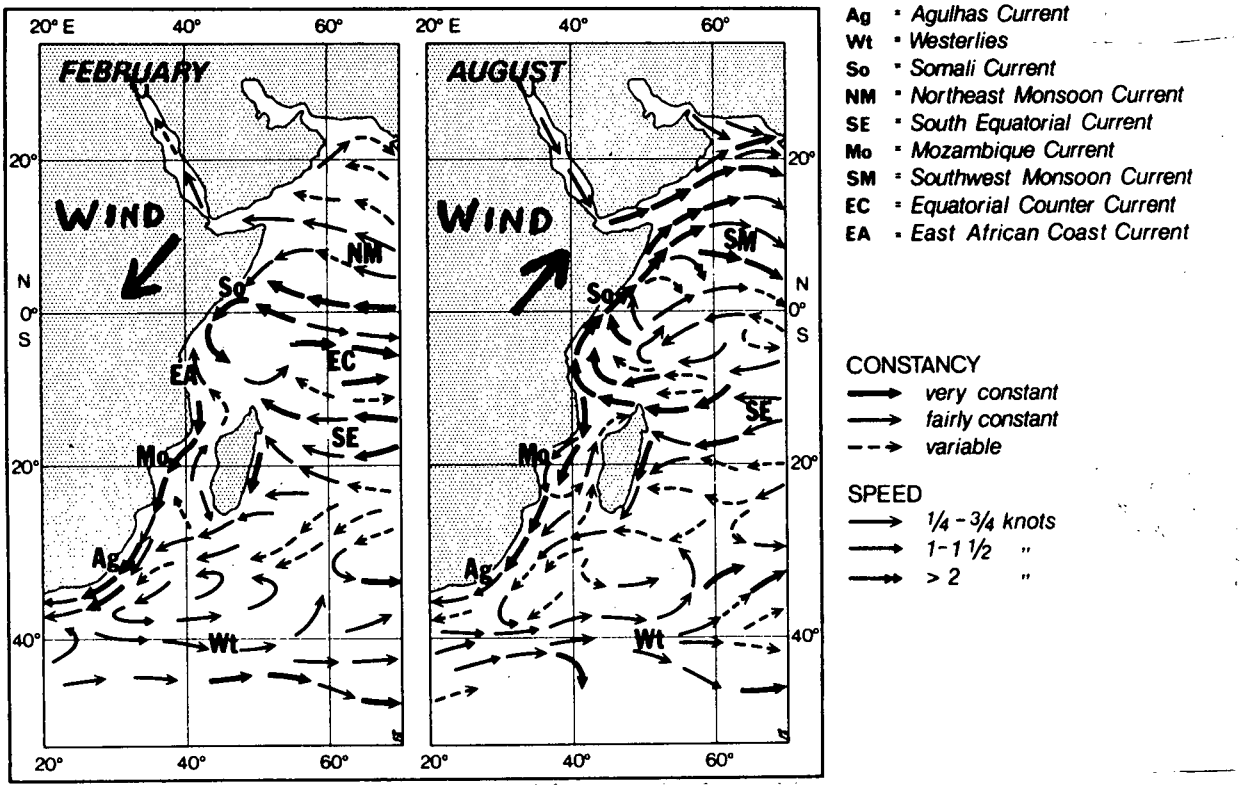

Fig.III.12. Schematic distribution of surface currents in the western Indian Ocean during both monsoons and related nomenclature (from Düing and Schott, 1978).

Fluctuations in the Somali Current During 1976

In this section I will describe the fluctuations referred to in the introduction to this chapter (see Fig.III.11). I am primarily concerned with the 40- to 50-day fluctuations, but will briefly discuss the subinertial 17-day oscillation as well as the 3- to 5-day (subinertial) fluctuations. The discussion to follow will be based on an analysis that employs filtering and spectral techniques. The filtering is accomplished in a conventional manner, viz., using a Butterworth filter (see e.g. Kanasewich, 1977). Because the records are short, maximum

likelihood has been used in the spectral analysis; the merits of this technique are discussed in Appendix I.

Description of the Data

The current and temperature data were acquired jointly by the Universities of Kiel and Miami, as part of the INDEX pilot studies. A description of the (1976) experiment is found in Düing and Schott (1978).

The current and temperature data from moorings K1 and K2 supplied to the author were half-daily means which were interpolated from low-passed data (in which tidal energy was removed). The K1 records analyzed started on January 15 (1976) and extended to June 18 (1976), yielding approximately a 5-month time span. The records from K2 started January 16 and extended to July 3. Note, however, that some current records from K1 are truncated due to rotor malfunction (see Table 1). The rotor loss at the top sensor of K1 was due to a "high speed burst" of current that induced sufficient mooring tilt to lift the rotor out of its bearings. Thus, at K1, the possibilities for comprehensive data analysis are limited, not only due to data loss, but also due to contamination of the records by the burst and its transient effects. In fact, the burst appears in the longshore current at all sensor depths, causing a sudden

temperature drop at each sensor; only the offshore component of the current was unaffected by the burst. In the discussion to follow, I will concentrate on the data from station K2.

Physical Situation at K1 and K2

Stations K1 and K2 span an area known as the source region of the Somali Current. The climatic mean surface current field near K1 and K2 is shown in Fig.III.12. During the Northeast Monsoon (February in Fig.III.12), K1 is in the zone of the East African Coast Current, which has a strong northward flow throughout the observation period. During this period, station K2 is near the convergence zone of the East African Coast Current and the southward flowing Somali Current. However, after the transition to the Southwest Monsoon (August in Fig.III.12) the flow at both stations becomes part of the strong, northward flowing Somali Current system.

The analysis of the 1976 records shows that the deep flow at K1 is weaker than the surface flow, but is always northward in direction. The deep flow at K2 is, however, somewhat more complicated. In Fig.III.13 one sees that the longshore mean flow at K2 is always northeast at the top sensor, occasionally southwest at the middle sensor, and almost steadily southwest at the bottom sensor. Fig.III.14 shows this southwest flow

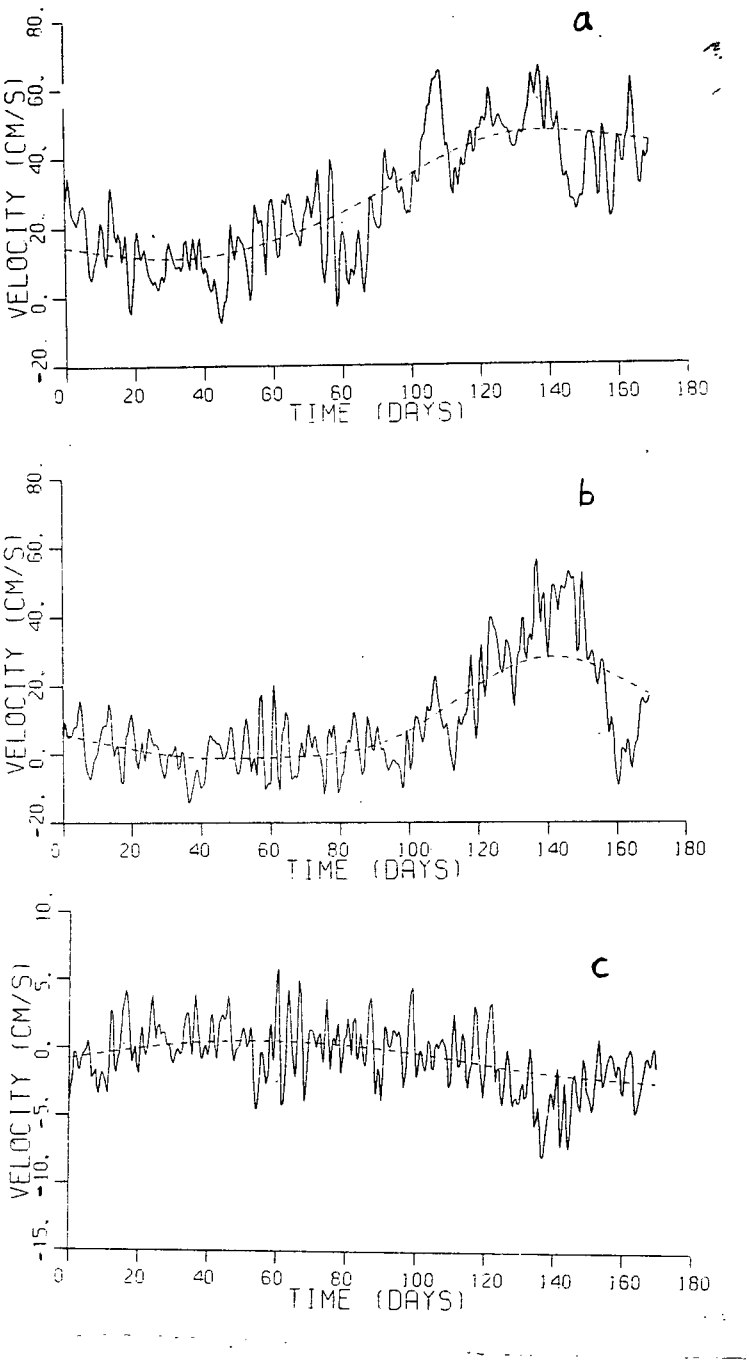

Fig.III.13. (a) The longshore velocity record from the top sensor of station K2. The dashed line represents a spline-fit to the mean current.
(b) As in (a), except for the middle sensor at K2.
(c) As in (a), except for the bottom sensor at K2. Note that the vertical scale is one-quarter that in (a).

condition to be typical of the deep flows near K2 (we see a reversal in the profile at about 250m, which is similar in depth

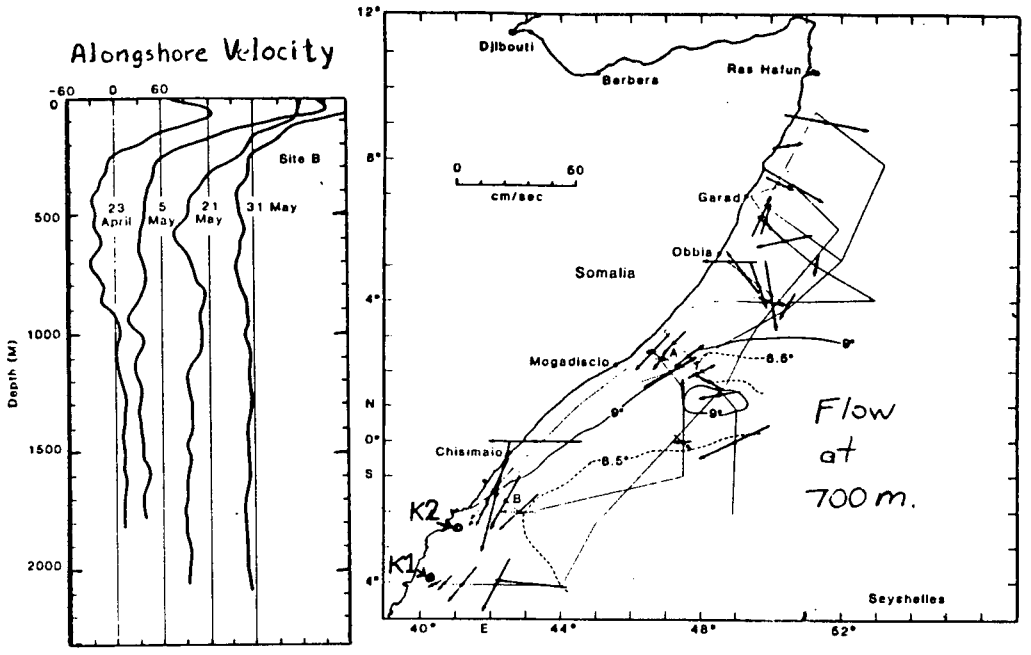

Fig.III.14. Current profiles (left) and lateral distribution (right) of the deep flows at site B, a station not far from K2. Each consecutive profile has been shifted by 60 cm/s to the right of the previous profile. The data were collected during INDEX (1979). (From Leetmaa, Rossby, Saunders, and Wilson, 1980).

to the bottom sensor of K2). It is suggested here that the deep southwest flow is topographically deflected seaward before reaching K1. One sees in Fig.III.15 that station K2 is near the shelf break; the flow at the upper sensor is characteristic of the continental shelf regime (northeast flow), while the flow at the bottom sensor seems to represent the shelf/slope flow regime. An idealized impression of the situation is given in Fig.III.16.

I will return to these considerations in Chapter IV when model parameter fitting is discussed.

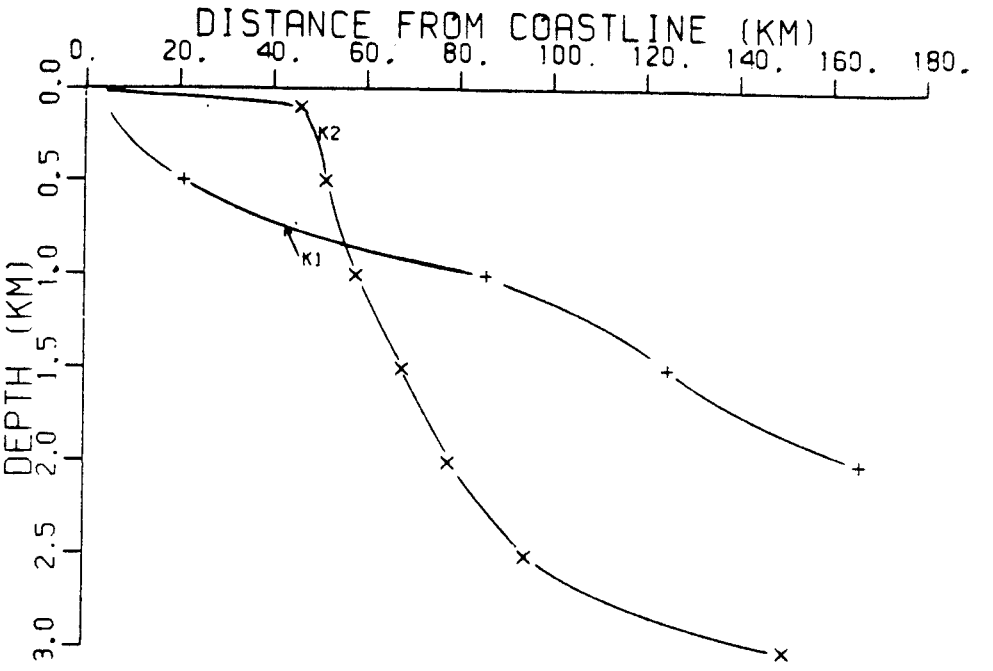

Fig.III.15. The bottom topography at stations K1 and K2.

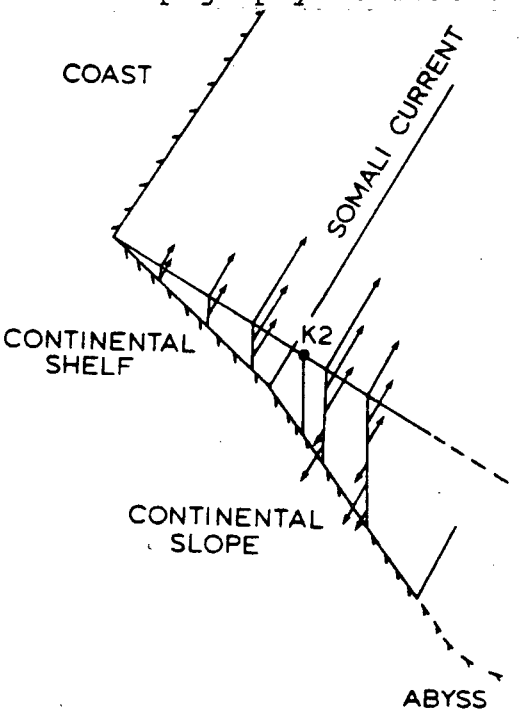

Fig.III.16. A conceptual model of the mean flow near station K2 during the period of strongest flow (late May).

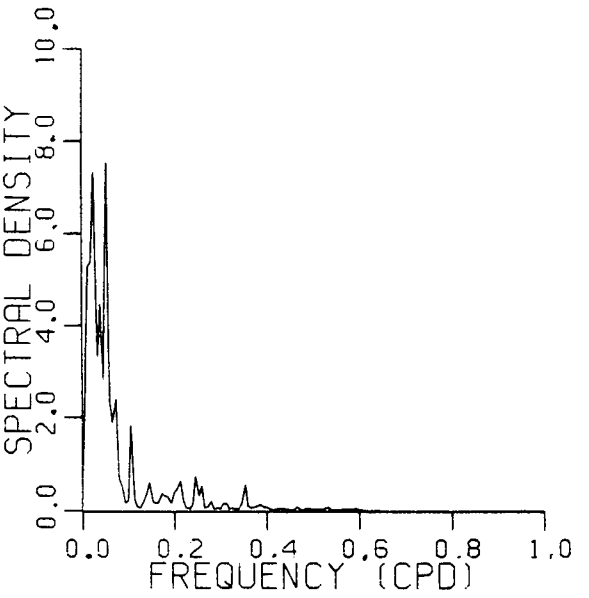

Fig.III.17. Autospectrum of the temperature fluctuations at the top sensor of station K1. The spectral density is in units of $(°C)^2$/cpd.

Fluctuations at K1

At the beginning of Section 2, I noted that the "high speed burst" at K1 in early March caused data loss and complicates the data interpretation. Thus, although I find spectral evidence for low-frequency fluctuations (in a 30- to 75-day band; see Fig.III.17), it is not clear whether or not these low-frequency oscillations are just transients associated with the burst. To clarify matters, it is useful to examine the low-passed (again using a Butterworth filter) temperature and current records. Fig.III.18a,b,c,d,e,f shows the low-passed (cutoff period of 25

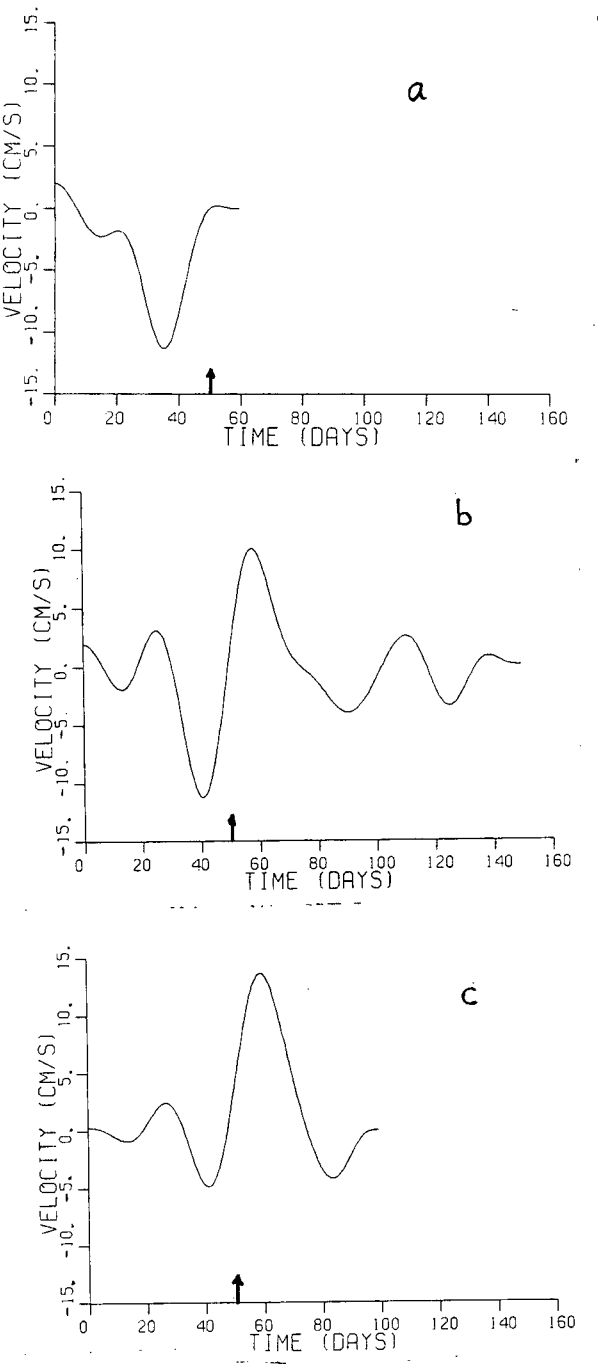

Fig.III.18. (a) Low-passed longshore velocity record from the top sensor at station K1. The time of the high speed burst is indicated by an arrow.
(b) As in (a), except for the middle sensor at K1
(c) As in (a), except for the bottom sensor at K1

days) longshore velocity and temperature records. The longshore velocity records (Fig.III.18a,b,c) show evidence of a long

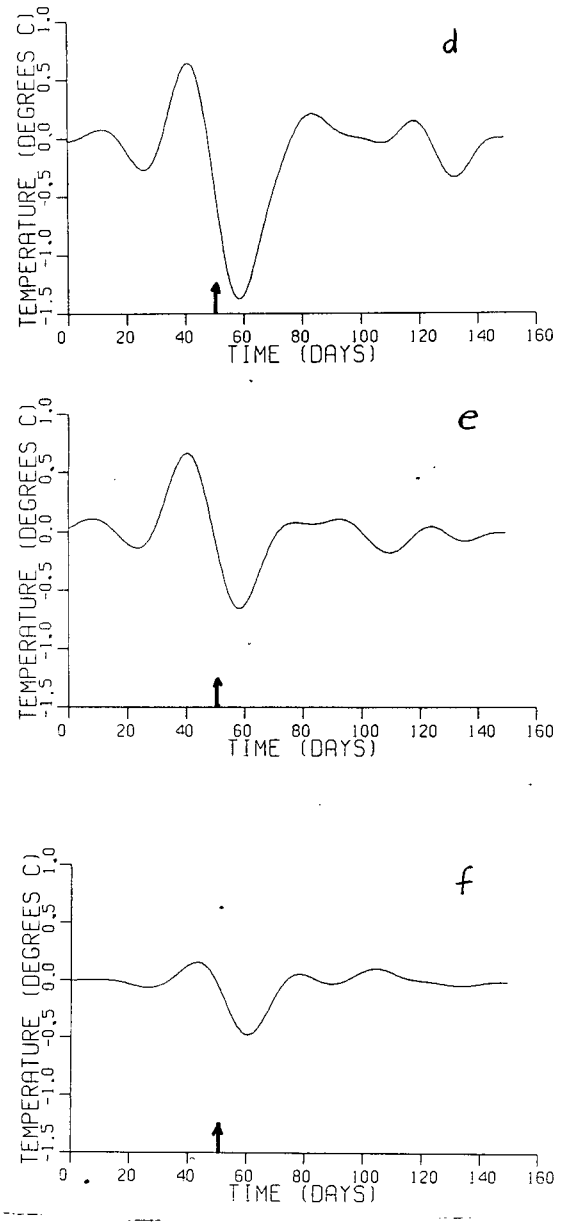

Fig.III.18 (cont.).
(d) Low-passed temperature record from the top sensor at station K1. The time of high speed burst is indicated by an arrow.
(e) As in (d), except for the middle sensor at K1.
(f) As in (d), except for the bottom sensor at K1.

period fluctuation before the high-speed burst (which occurs after about 50 days have elapsed from the start of the record). The oscillations are best seen in the records from the middle

and bottom sensors which both show about a 4 cm/s amplitude with no apparent phase shift between these sensors. The low-passed temperature records clearly show a constancy of phase with depth in the pre-burst fluctuations. These fluctuations may be wind-induced; the strong longshore velocity fluctuations seen at the bottom sensor (at a depth of 445m) indicate a barotropic response. The relatively weak current shear at station K1 may allow this apparent barotropic response, in contrast to the situation at station K2 where the current shear is stronger and the response is definitely not barotropic.

Fluctuations at K2

Evidence for a 40- to 50-day oscillation is most clearly found in the K2 temperature spectra (Fig.III.19a,b,c). These spectra are calculated over the first 150 days of the 170 day records (150 days yields a spectral band centered on 50 days). This figure shows that the temperature records have their variance concentrated at low frequencies: the dominant spectral peaks occur at periods of 38 days, 50 days and 50 days in the records of the top, middle and bottom sensors, respectively. [I will refer to the low-frequency peak, defined in frequency only approximately, as the 40- to 50-day peak].

To aid in interpretation of these low-frequency fluctuations, it is helpful to examine the low-passed versions of the records under consideration. The low-passed temperature time series are shown in Fig.III.20a,b,c for each sensor depth at station K2. The low-frequency temperature fluctuations are apparently quite transient at the top sensor; the lower two sensors show a comparatively steady low-frequency record. The bottom sensor shows four peaks over an approximate 150-day span, implying an average 50-day period for the fluctuations.

One expects the low-frequency temperature fluctuations to be related to any low-frequency velocity fluctuations present; to this end I now examine the low-passed longshore velocity records (Fig.III.21a,b,c). At the top sensor, the longshore velocity record, unlike the corresponding temperature record, initially shows little low-frequency fluctuation, with a rapid

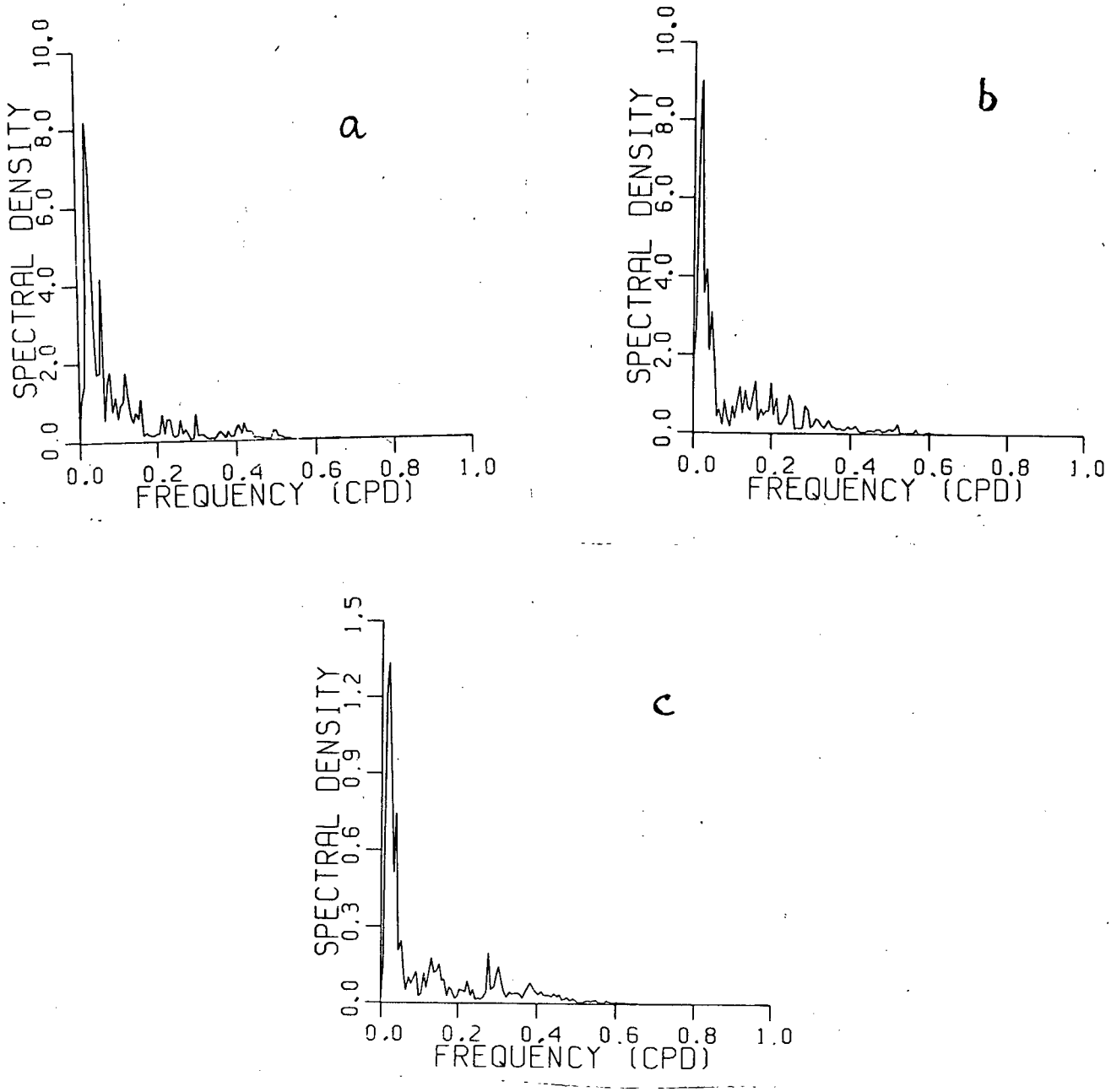

Fig.III.19. (a) Autospectrum of the temperature fluctuations at the top sensor of station K2. The spectral density is in units of $(°C)^2$/cpd.
(b) As in (a), except for the middle sensor at K2.
(c) As in (a), except for the bottom sensor at K2. Note that the vertical scale is about one-sixth that in (a).

build up of low-frequency energy about 50 days into the record.

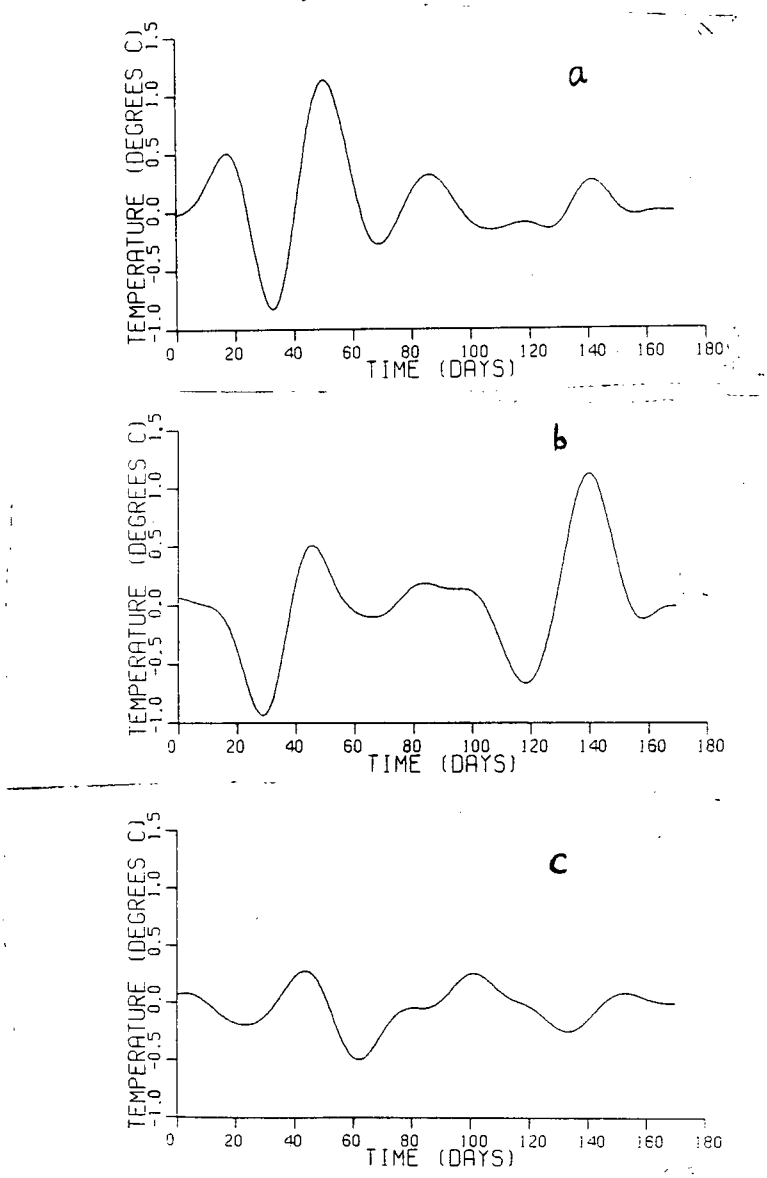

Fig.III.20. (a) Low-passed temperature record from the top sensor at station K2.
(b) As in (a), except for the middle sensor at K2.
(c) As in (a), except for the bottom sensor at K2.

The middle and bottom sensors show a rapid increase in low-frequency variance at considerably later times. The power spectrum of the longshore velocity fluctuations at the top sensor (Fig.III.22a, calculated over the same 150-day segment as the temperature fluctuations, shows a strong 40- to 50-day peak. The 40- to 50-day peak also appears in the spectra of the last

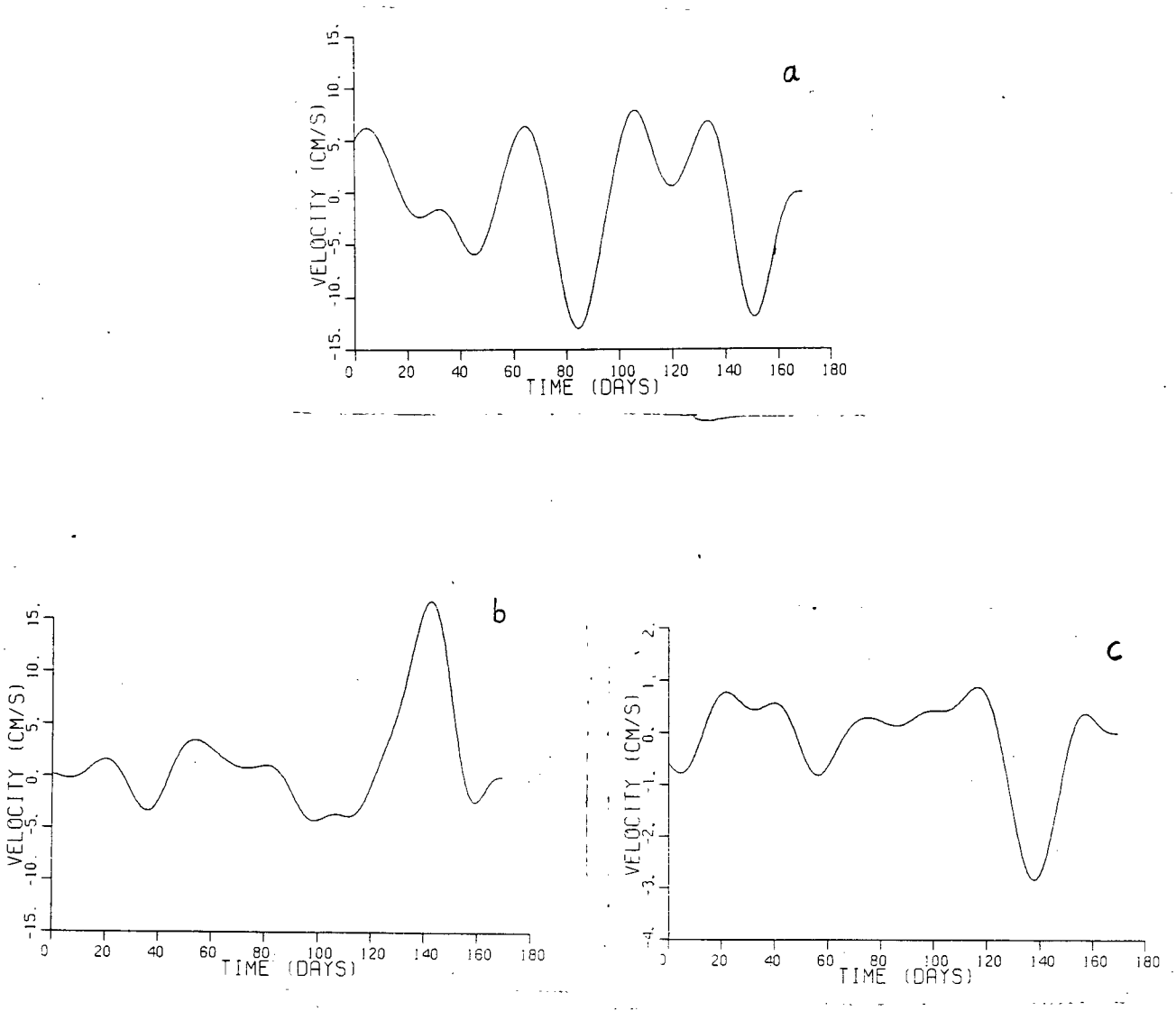

Fig.III.21. (a) Low-passed longshore velocity record from the top sensor at station K2.
(b) As in (a) , except for the middle sensor at K2.
(c) as in (a), except for the bottom sensor at K2. Note that the scale is one-fifth that in (a).

100 days of the lower two longshore velocity records (Fig.III.22b,c).

Apparent in Fig.III.22a is evidence for fluctuations at a

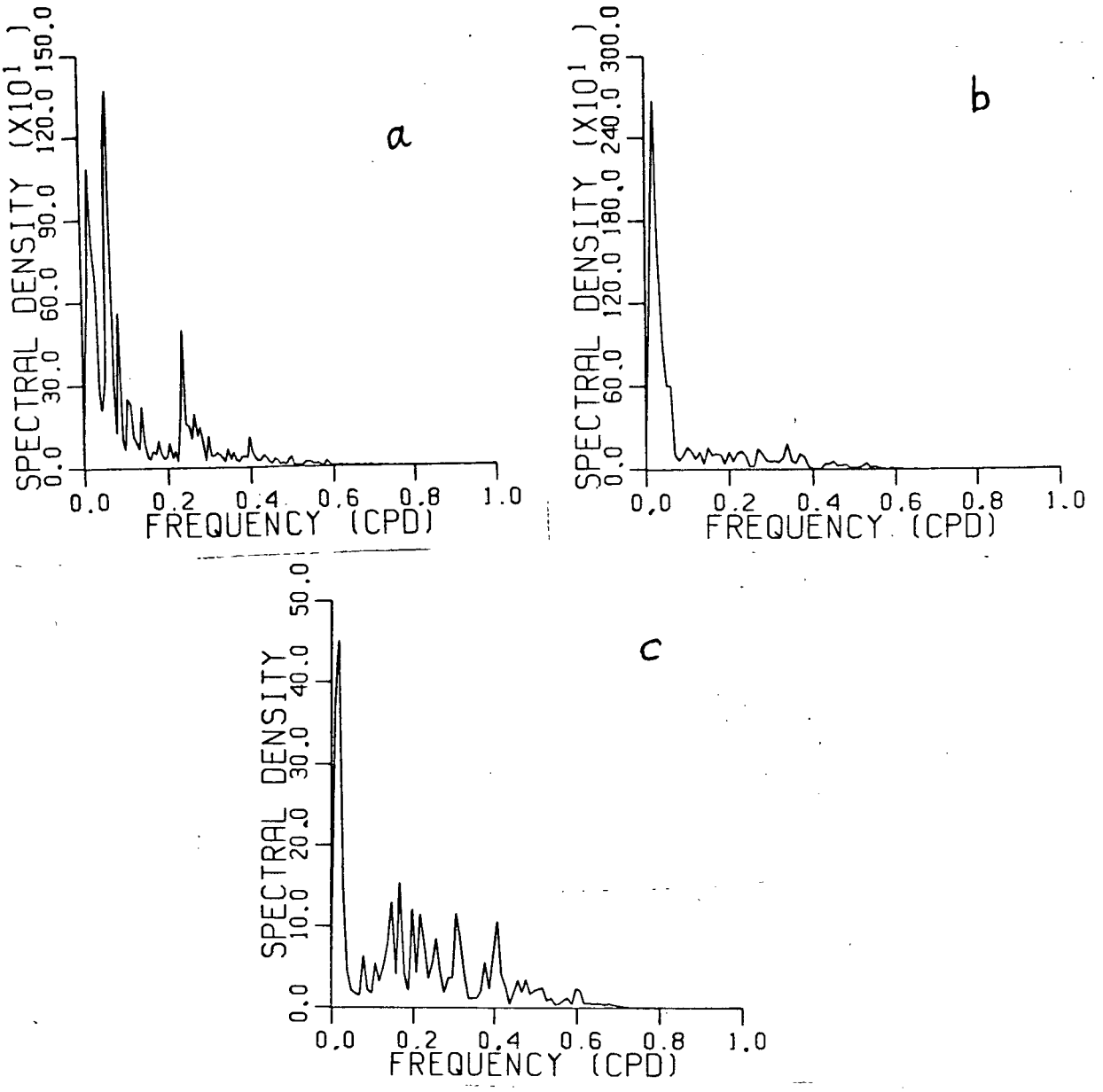

Fig.III.22. (a) Autospectrum of longshore velocity fluctuations at the top sensor of station K2. The spectral density is in units of $(cm/s)^2/cpd$.
(b) As in (a), except for the middle sensor at K2. Note that the vertical scale is twice that in (a). The spectrum was calculated over the last one hundred days of the record.
(c) As in (a), except for the bottom sensor at K2. Note that the vertical scale is one-thirtieth that in (a). The spectrum was calculated over the last one hundred days of the record.

period of 4 days. These oscillations would be superinertial at the latitude of K2, where the inertial period is 10.3 days. Schott and Quadfasel (1982) have found evidence for the

existence of 3- to 5-day oscillations at stations several hundred kilometers north of K2 (about 5°N). The authors suggest that these oscillations are due to barotropic instability of the mean current. One also sees in Fig.III.22a an additional prominent low-frequency peak at about 17 days. This peak also seems to be present in the spectrum of the top sensor temperature fluctuations (Fig.III.19a), and it appears clearly in the band-passed (12.5 to 25 days) top sensor longshore velocity records (Fig.III.23). These fluctuations have been

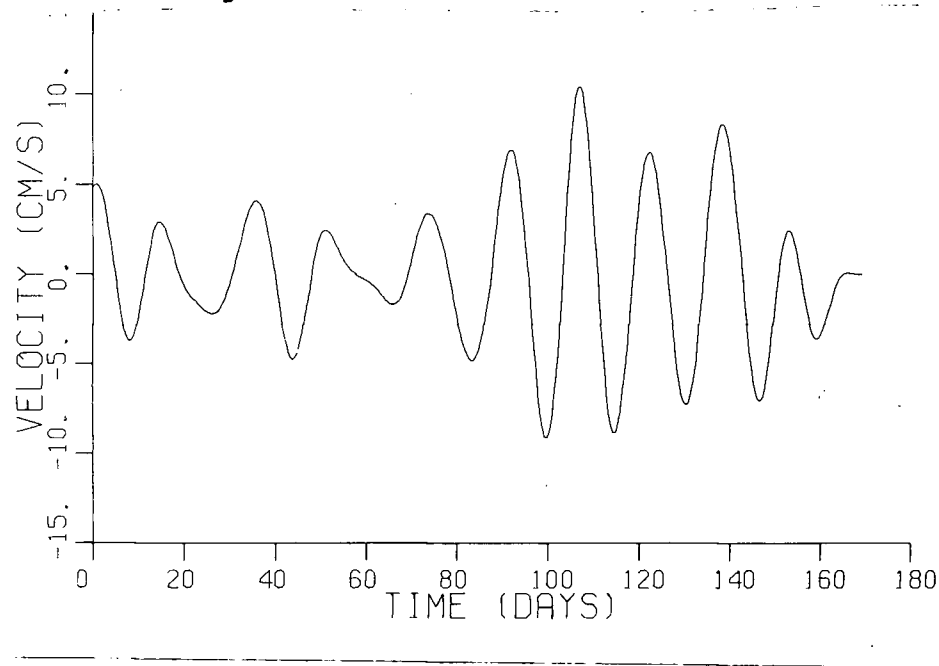

Fig.III.23. Band-passed (12.5 to 25 days) longshore velocity record from the top sensor at station K2.

observed by Schumann (1981) at various sites off the Natal coast (see Fig.III.24). As shown in Fig.III.25, the 17-day signal is strongly coherent, for the temperature and offshore velocity fields, between stations along the coast. The signal also shows strong coherence between the longshore wind velocity and the offshore current velocity. Schumann also shows that the 17-day

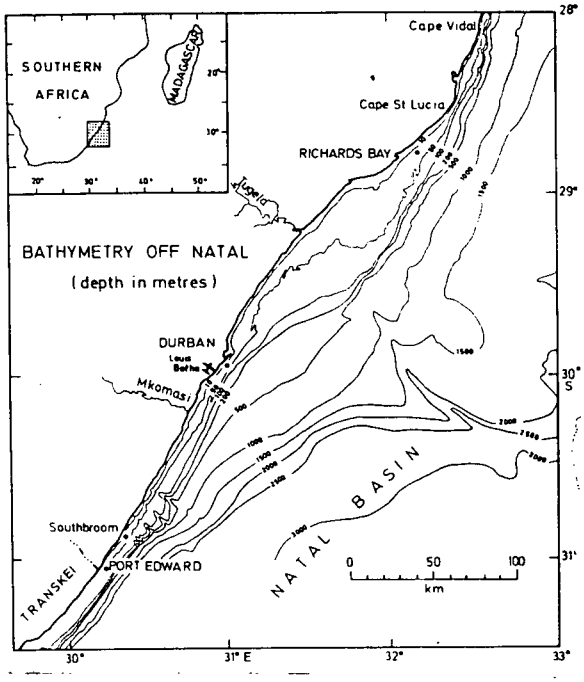

Fig.III.24. Location of measurement sites for Schumann's Natal experiment.(From Schumann, 1981).

winds exhibit seasonality, with the spectral energy of 17-day fluctuation decreasing from the April to September segment analysed to the October to February segment analysed. This seasonality of the wind energy at 17-days may account for the transient nature of the oscillation seen in Fig.III.23 (note that oscillation is strongest in the months from April to June). The 17-day oscillation has been found in other midlatitude wind analyses; see Speth and Madden (1973). Apparently, little is known about this oscillation in the tropics; Fig.III.4 of this

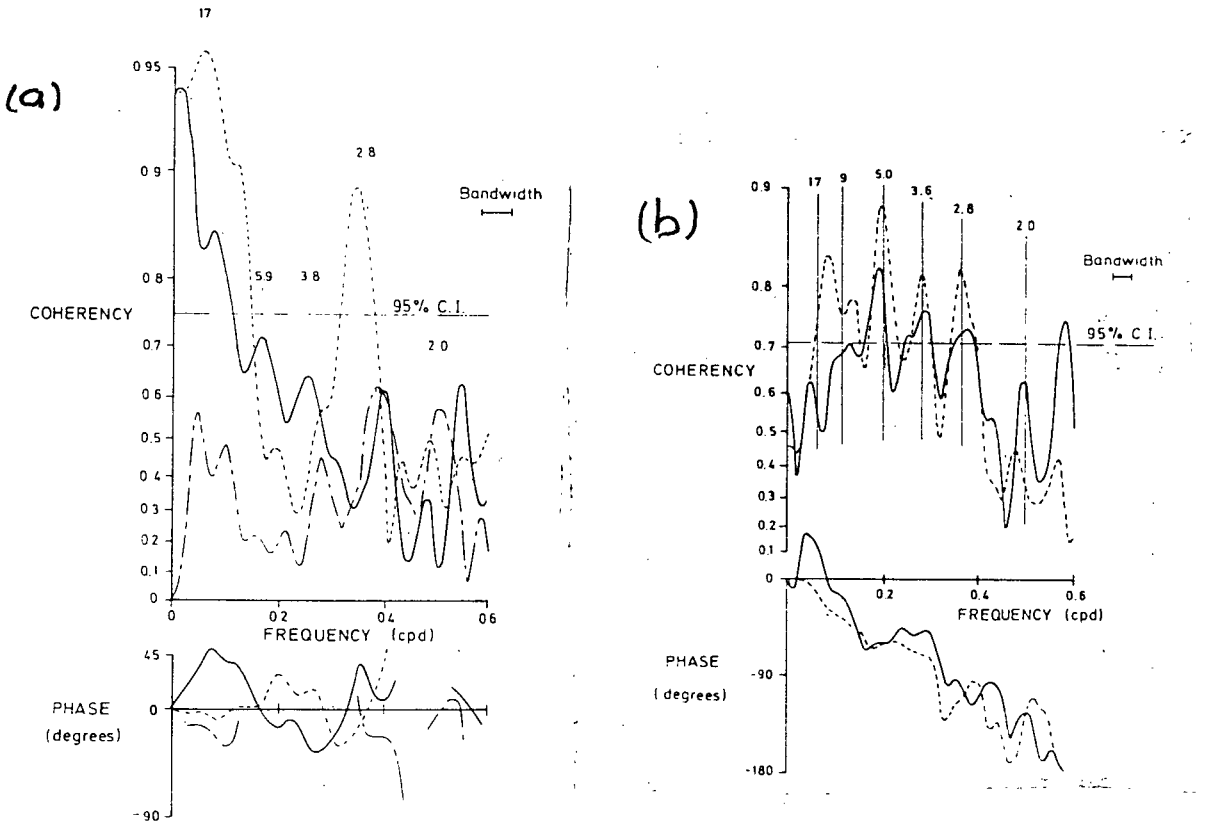

Fig.III.25. (a) Coherency and phase spectra between measurements made at moorings off Port Edward and Southbroom (see Fig.III.24). Solid line indicates longshore current components, dashed line indicates offshore current, components, and dotted line indicates temperature.
(b) Coherency and phase spectra between the longshore wind measured at Louis Botha airport and the longshore current (solid line) and the offshore current (dotted line) measured at Richard's Bay. (From Schumann, 1981).

thesis suggests that the oscillation is not present in the tropical atmosphere[4] (over the Western Indian Ocean) and thus that the oceanic signal must have propagated northward off the coast of Natal.

Of the offshore velocity spectra, only that of the top

---

[4] Madden (1978) has shown that the latitudinal structure of the atmospheric 16-day oscillation shows little energy at low latitudes (see Fig.III.26).

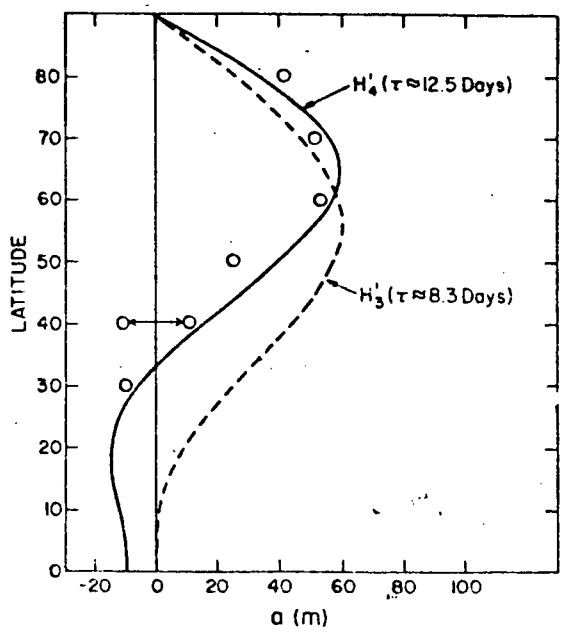

Fig.III.26. Amplitude of Hough functions (H'_3 ,H'_4) versus latitude and the measured amplitude of a 16-day wave at 100 mb. (From Madden , 1978).

sensor's record shows any energy near 50 days (the lowest frequency peak in Fig.III.27 at 30 days). If one examines the low-passed record from this sensor (Fig.III.28), one sees a striking similarity of the record to that of the longshore fluctuations (Fig.III.21a). Specifically, after about 50 days the records show high (visual) correlation with little phase difference. These facts seem to indicate a highly rectilinear oscillation, directed somewhat eastward of the chosen axis (the longshore oscillations have about twice the amplitude of the offshore oscillations).

Comparison of Fluctuations at K2 and K1.

If one compares Fig.III.19d,e,f with Fig.III.21a,b,c one sees a strong resemblance in low frequency temperature fluctuations in the time interval prior to the high speed burst

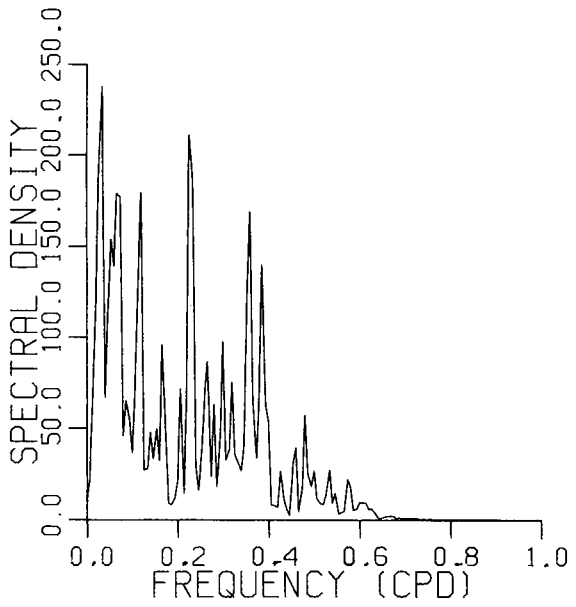

Fig.III.27. Autospectrum of the offshore velocity fluctuations at the top sensor of station K2. The spectral density is in units of $(cm/s)^2/cpd$.

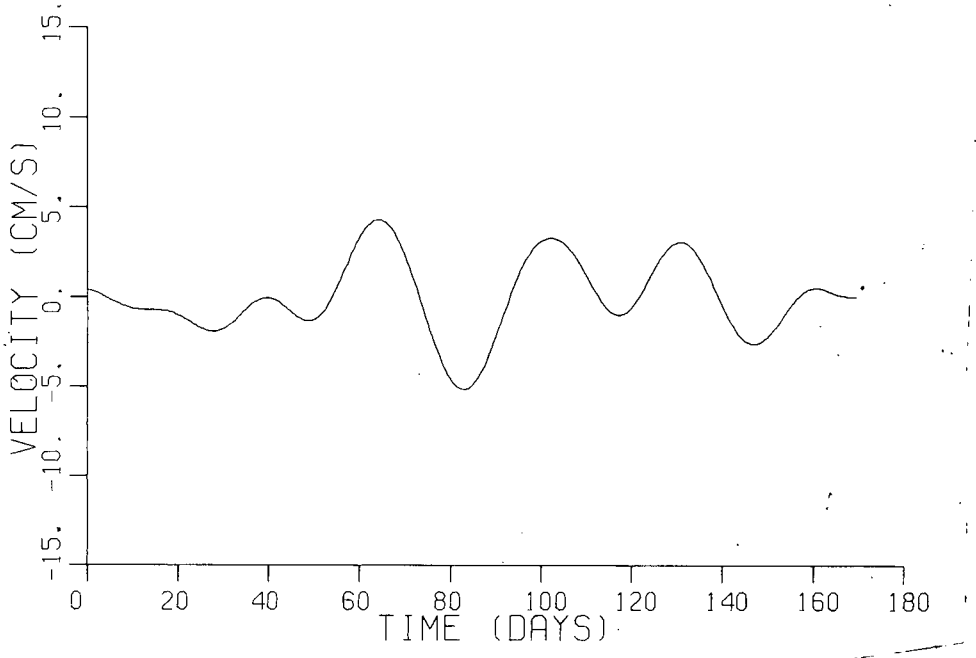

Fig.III.28. Low passed offshore velocity record from the top sensor of station K2.

(around day 50) at K1. To obtain a crude estimate of the longshore wavelength one can compare the phase of the fluctuations at the top sensor of K1 with the phase of the fluctuations at the mid-sensor of K2 since they are at similar

depths (180m vs. 176m). The large peak at K1 (prior to the burst) occurs about five days earlier than the corresponding peak at K2. If this represents a delay due to wave propagation (from K1 to K2), a phase speed of (154km/5days) $\approx$ 30km/day (K1 is about 154 km from K2) is implied. This phase speed estimate corresponds to a wavelength of (50 daysx30km/day)=1500km, which has a large uncertainty, being based on one cycle of data.

III.4 Summary

In Chapters II and III I have presented the body of information regarding the 40- to 50-day oscillation. The review of the literature (Chapter II) showed the atmospheric oscillation to be global in nature. The tropical component, propagating eastward with planetary wavenumber 1, and modulating the Walker cell, is connected to a midlatitude component by poleward propagating fluctuations. While there is relatively little information in the literature on the oceanic 40- to 50-day oscillation, it has been suggested that the oscillation propagates as an equatorial Kelvin wave (confined to within 3° of the equator) in the Pacific Ocean and probably also in the Indian Ocean.

The contribution of this thesis, as described in this chapter, has been to show the existence of the 40- to 50-day fluctuations in an interesting and important region, namely the source of the Somali Current. It is important that the existence of the oscillation be shown there, since that region is on the western boundary of the Indian Ocean, which is thought to be the source of the (eastward propagating) fluctuations. It may be that the land-sea contrast in this area is necessary for generating the fluctuations, and indeed the strength of the fluctuations, as established in this chapter, may lend credence to this notion. The nearby East African Highlands are known to have an important influence on the atmospheric circulation over the Western Indian Ocean, and appropriately, I noted in Chapter

II and showed in this chapter that the 40- to 50-day fluctuations propagate parallel to the coast (and this mountain range). The most important contribution of this thesis regarding the atmospheric 40- to 50-day oscillation, is the demonstration, for the first time, of its existence in wind stress curl data. The wind stress curl is very important since it is the forcing term for oceanic low-frequency motions. I will make extensive use of the wind stress curl analysis in Chapter IV.

The analysis of the oceanic data has established, for the first time, the existence of the 40- to 50-day fluctuation as a coastal equatorial phenomenon. Further, some evidence has been presented which indicates that this oscillation travels along the coast toward the equator. I have shown that large fluctuations exist in the oceanic temperature field (of the order of 2°C). This is an important observation in that air-sea interaction is thought to play an important role in the generation of the 40- to 50-day oscillations, via heat exchange (see Chapter IV).

IV. The Oceanic Response to Atmospheric Forcing

IV.1. Introduction

The preceding chapters have presented considerable evidence which shows that:

(i) An oscillation of 40- to 50-days period exists in the atmosphere over a wide meridional belt of the tropics, being weak or undetectable only over the Atlantic.

(ii.) An oscillation of 40- to 50-days period exists in both the tropical Indian and Pacific Oceans.

These points suggest that there is a relation between the atmospheric and oceanic 40- to 50-day oscillations. It is possible that: (i.) the atmosphere drives the ocean, (ii.) the ocean drives the atmosphere, or (iii.) the oscillation is due to an ocean-atmosphere feedback. I will examine the first possibility in some detail in this chapter by presenting some specific wind-driven models of equatorial and coastal circulation and applying these models to the observations discussed earlier. In Appendix III mechanisms (ii.) and (iii.) are briefly discussed.

The time-dependent modelling of an atmospherically forced ocean has a long history. For example, Veronis and Stommel (1956) looked at the mid-latitude oceanic response to time-harmonic atmospheric forcing. Large scales were also examined in Lighthill's (1969) treatment of the response of the Indian Ocean to seasonal variations of the wind stess. At intermediate

scales, atmospherically generated continental shelf waves have been predicted and detected. To properly model the response of the ocean to the 40- to 50- day atmospheric oscillations one should employ the full nonlinear Navier-Stokes equations for a rotating stratified, fluid. However, such a treatment is beyond the scope of this thesis. To make the general problem tractable the most important features of the dynamics will be modelled separately. Thus, two models will be used to calculate the response of the ocean on the largest scale, and in these models variations of the coriolis parameter will be included. Specifically, the basin and equatorial Kelvin wave responses to the global-scale atmospheric circulation cells will be calculated. Next, the effects of a strong horizontal mean current shear will determined via a reduced gravity model of the upper-layer , where current shears are strongest. The vertical structure of the response will then be determined with a quasi-geostrophic three-layer model (now ignoring horizontal variations). In all cases the problems will be treated as linear.

Preliminary Considerations

Before I proceed to introduce models of the atmospherically driven ocean, it is useful to determine the relevant length, time, and amplitude scales associated with the fluctuations. The most important problem is to explain the magnitude of the observed oceanic fluctuations. That is, one must first establish

that wind forcing can account for the strength of the oceanic oscillations before attemting to explain details of the observations. Accordingly, I will now examine the fundamental scales for velocity and temperature:

There are two natural scales for the wind-driven current velocity ,V (see, e.g., Pond and Pickard, 1978):

(i.) an Ekman scale $$V_E = \frac{\tau^{(x)}}{\rho H f} \qquad \text{(IV.1a)}$$

(ii.) a Sverdrup scale $$V_s = \frac{curl_z \underset{\sim}{\tau}}{\rho H \beta} \qquad \text{(IV.1b)}$$

The maximum values of $\tau^{(x)}$=.3 dyne/cm^2, $curl_z \underset{\sim}{\tau}$ =6x10^{-8} N/m^3 are obtained from Fig.(III.7a,b) and with $|f| \approx 10^{-5}$ s^{-1} (at about 2.5°S), $\beta \approx 2\times10^{-11}$m^{-1}s^{-1}, H$\approx$100m, one finds from (IV.1) the maximum response of response averaged over the wind mixed layer (upper 100 meters) is

$$V_E \approx 3 \text{ cm/s}, \qquad V_s \approx 3 \text{ cm/s} \qquad \text{(IV.2)}$$

In section (III.3a) it was shown that much larger velocities than this (up to 10 cm/s) were found at depths considerably greater than 100m. This fact suggests that direct wind forcing (i.e., an Ekman or Sverdrup response can account for only a small part of the observed 40- to 50-day current velocities. If the oceanic signal is wind-driven, then a mechanism must be invoked to explain the enhancement of the response over direct forcing scales; e.g., a wave-resonance mechanism.

Simple scaling arguments allow one to account for the temperature fluctuations with direct wind forcing; i.e., without resort to wave models. The initial temperature fluctuation amplitudes at station K2 are shown in the second column of Table 2. From the second and third columns, the fluctations are seen to vary roughly as the mean temperature gradients do. This suggests that the fluctations are induced by a relatively depth-independent (over 125-251 m) vertical velocity. This is based on the assumption that the temperature fluctuations (T') are related to the mean temperature gradient ($\frac{\partial \bar{T}}{\partial z}$) and the isotherm displacement (η) by $T' = \frac{\partial \bar{T}}{\partial z}\eta$. The information in Table 2 allows one to calculate an estimate for η:

$$\eta \approx 10\,m \qquad \text{(IV.3)}$$

A low-frequency wave off the equator will approximately satisfy the geostrophic equations for a reduced gravity model (i.e., as in Pedlosky, 1979, equation(3.12.4), the time variations are much slower than the inertial frequency so that an approximate geostrophic balance holds throughout the fluid)

$$-fv = -g'\eta_x \qquad \text{(IV.4a)}$$

$$fu = -g'\eta_y \qquad \text{(IV.4b)}$$

(the equations are vertically averaged over the upper mixed layer; g' is the reduced gravity).

Table 2. Initial temperature fluctuations at K2.

Sensor	Fluctuation Amplitude	Mean temperature gradient (see Figs.IV.13, IV.16)
1 z=125 m	0.9°C	0.1°C/m
2 z=176 m	0.75°C	0.07°C/m
3 z=261 m	0.35°C	0.03°C/m

Thus a scale for the interfacial displacement at the base of the mixed layer due to a quasi-geostrophic wave would be

$$\eta \sim \frac{f V L_x}{g'} \sim \frac{f U L_y}{g'} \qquad \text{(IV.5)}$$

where U,V are scales for the x,y components of the velocity and L_x and L_y are length scales for the x,y directions. Düing and Schott (1976) give 100 km as the scale width of the Somali Current, thus I take L_x =100 km. In Chapter II I deduced a longshore wavelength for the 40- to 50- day oscillations of 3200 km (see Fig.II.9). Thus, I take $3200/2\pi$ km as L_y . From section III.3, one finds that approximate depth averaged values for U, V are

$$V \approx 5 \text{ cm/s} \qquad U \approx 1 \text{ cm/s} \qquad \text{(IV.6)}$$

Thus one finds, using $g' \approx 2.5 \times 10^{-2} ms^{-2}$, $|f| = 7 \times 10^{-6} s^{-1}$

$$\eta_{WAVE} \approx 1.5m \qquad \text{(IV.7)}$$

Since this is much less than the 10m displacement required (see IV.3), one must now look at an Ekman pumping model. From the Ekman and continuity equations integrated over the wind forced layer, viz.,

$$-fv = \frac{\tau^{(x)}}{\rho H} \qquad \text{(IV.8a)}$$

$$-fv = \frac{\tau^{(y)}}{\rho H} \qquad \text{(IV.8b)}$$

$$u_x + v_y = \frac{1}{H}\eta_t \qquad \text{(IV.8c)}$$

(η_t evaluated at the layer bottom)

one can easily show

$$\eta_t = \frac{curl_z \tilde{\tau}}{\rho f} \qquad \text{(assuming f=constant)} \qquad \text{(IV.9)}$$

The Ekman balance specified by (IV.8a,b) is valid, as Pedlosy (1979, p.176) notes, when the layer under consideration is homogeneous (allowing separarion of Ekman and geostrophic velocities) as is approximately the case for the wind-mixed layer. Using Fig. (III.7b) one finds maximum wind stress curl amplitudes of about 6×10^{-8} Nt/m^3. Thus equation (IV.9) gives (with f=-7×10^{-6} s^{-1} and $\rho = 10^3$kg/m^3)

$$|\eta| = \frac{|\eta_t|}{\omega} \approx 5m \quad \text{for a 50-day oscillation} \qquad \text{(IV.10)}$$

Thus the Ekman pumping model accounts for the order of magnitude of the temperature fluctuations. It is now helpful to compare the time histories of the temperature field (Fig. III.20a,b,c) with that of the wind stress curl (Fig.III.7b). First note that the temperature time series at the top two sensors are very much alike, except that the peak near 140 days is suppressed at the

upper sensor. The response at the upper sensor may be complicated by dynamical effects other than the Ekman pumping discussed above (I will return to this briefly in section IV.6). Thus, the second sensor represents the "purest" response to the wind stress curl. Accordingly, the two time series are plotted together in Fig. IV.1. The striking similarity of the two series lends credence to the simple Ekman pumping model and establishes the role of the atmosphere in forcing the ocean at 40- to 50-days.

In the remainder of this chapter I will look at three simple models of the oceanic response to a 40- to 50-day oscillation of the wind field. As noted in the introduction to this chapter, one expects the atmosphere to drive a basin-wide response as well as creating localized responses where restoring forces are concentrated (in this case forces due to mean current shears and bottom topography). First, the response of the ocean to the global-scale circulation cells will be examined. Next, two models will be employed to analyze the response of the coastal ocean strictly in the region of interest.

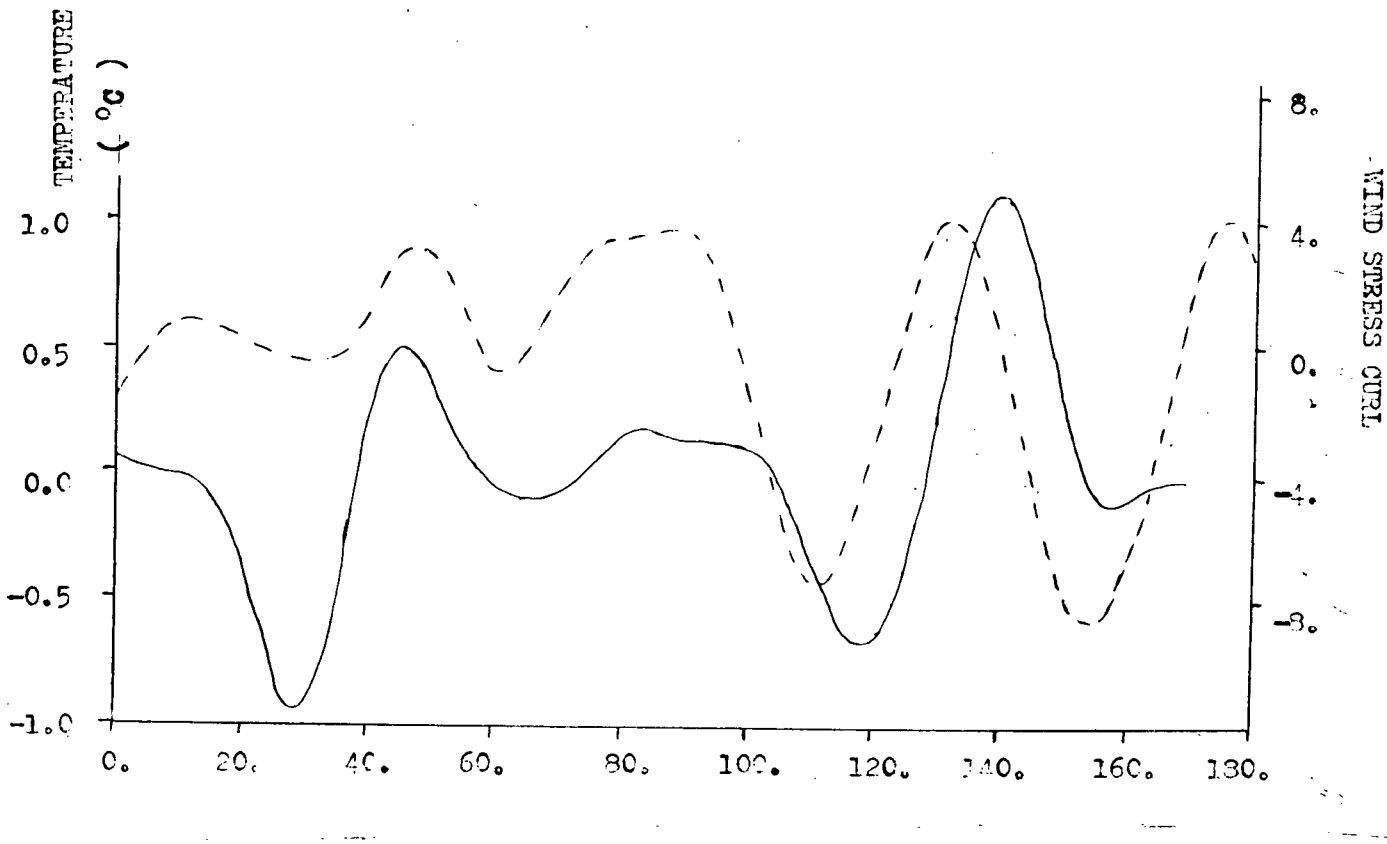

Fig.IV.1. Temperature fluctuations (solid line) at the mid-sensor of station K2 compared to the local wind stress curl (dashed line; in units of 10^{-8} N/m^3).

IV.3 Response of the Equatorial Ocean to the Global-Scale Circulation Cells: Generation of Equatorial Kelvin Waves.

In section II.3 , it was shown that the 40- to 50-day oscillation of the atmosphere has a tropical component which propagates throughout the Indian and Pacific Oceans as a (planetary wavenumber 1) equatorial Kelvin wave . In section II.5 it was shown that the oceanic 40- to 50-day oscillation propagates throughout the Pacific (and possibily the Indian Ocean) as a first baroclinic mode equatorial Kelvin wave with equivalent depth h_1 =.71 m. It is interesting, then, to see whether the atmospheric (global-scale) circulation cells can deliver sufficient forcing to account for the oceanic observations. The analysis will utilize the estimates of the wind stress curl from Chapter III to establish the stength of the forcing.

From the momentum equations for an Kelvin wave on an equatorial plane (invoking an equatorial plane results in an error of only 14% even at 30° north or south latitude, according to Gill, 1982, p.434)

$$u_t = -\frac{p_x}{\rho} + \frac{1}{\rho}\frac{\partial \tau^{(x)}}{\partial z} \qquad \text{(IV.11a)}$$

$$\beta y u = -\frac{p_y}{\rho} + \frac{1}{\rho}\frac{\partial \tau^{(y)}}{\partial z} \qquad \text{(IV.11b)}$$

one forms the vorticity equation

$$u_{ty} - \beta y\, u_x = \frac{1}{\rho}\frac{\partial}{\partial z}\left(\mathrm{curl}_z \underset{\sim}{\tau}\right) \qquad \text{(IV.12)}$$

which involves the known forcing function $\mathrm{curl}_z\underset{\sim}{\tau}$. One must project this forcing function onto the vertical and horizontal eigenmodes. Following Luther (1980), the equivalent depth is based on a constant Brunt-Väisälä frequency ocean (of $N \approx 0.0023 s^{-1}$). Luther finds the 40-to 50-day Kelvin wave to be first baroclinic mode in nature. This first baroclinic mode (of a constant N ocean) has depth dependence given by the function $\cos(\pi z/H)\exp(-N^2 z/2g)$. For $N^2 \approx 5\times10^{-6}$ s^{-2} the factor $\exp(-N^2 z/2g)$ is approximately equal to 1 over the entire depth of about 2500m. Thus the projected forcing $F_{Effective}$ is given by

$$F_{effective} = \frac{\frac{1}{\rho}\int_{-H}^{0}\frac{\partial}{\partial z}\left(\mathrm{curl}_z\underset{\sim}{\tau}\right)\cos\left(\frac{\pi z}{H}\right)dz}{\int_{-H}^{0}\cos^2\left(\frac{\pi z}{H}\right)dz} \qquad \text{(IV.13)}$$

$$\left[\ \int_{-H}^{0}\cos^2\left(\frac{\pi z}{H}\right)dz = \frac{H}{2}\ \right]$$

Since $\mathrm{curl}_z\underset{\sim}{\tau}$ exists only over the shallow mixed layer of depth d_M , where $d_M << H$, one has

$$\int_{-H}^{0}\frac{\partial}{\partial z}\,\mathrm{curl}_z\underset{\sim}{\tau}\cos\left(\frac{\pi z}{H}\right)dz \cong \int_{-d_M}^{0}\frac{\partial}{\partial z}\,\mathrm{curl}_z\underset{\sim}{\tau}\,dz = \mathrm{curl}_z\underset{\sim}{\tau}\Big)_{SURFACE} \qquad \text{(IV.14)}$$

This latter function $\mathrm{curl}_z\underset{\sim}{\tau}\Big)_{SFC.}$ was given in equation(II.5) as

$$\left(\mathrm{curl}_z\underset{\sim}{\tau}\right)_0 \frac{y}{y_0}\exp\left[-2\left(\frac{y}{y_0}\right)^2\right]e^{i\omega t}$$

where periodic forcing ($e^{i\omega t}$) has been asssumed. Thus,

$$F_{effective} = \frac{2(curl_z \tilde{\tau})_0}{\rho H} \frac{y}{y_0} \exp\left[-2\left(\frac{y}{y_0}\right)^2\right] e^{i\omega t}$$

Now , for a Kelvin wave of the first baroclinic mode (of equivalent depth h_1)

$$u = u_0 e^{i(kx-\omega t)} e^{-\frac{\beta}{2(gh_1)^{\frac{1}{2}}} y^2} \qquad \text{(IV.15)}$$

so that equation(IV.12) becomes

$$e^{i(kx-\omega t)} e^{-\frac{\beta}{2(gh_1)^{\frac{1}{2}}} y^2} u_0$$

$$= \frac{-2i(curl_z \tilde{\tau})_0 e^{-2\left(\frac{y}{y_0}\right)^2} e^{i\omega t}}{\beta \rho H y_0 \left(\frac{\omega}{(gh_1)^{\frac{1}{2}}} - k\right)} \qquad \text{(IV.16)}$$

I now project the function $\exp[-2(y/y_0)^2]$ onto the latitudinal structure function for the first baroclinic mode by calculating the projection coefficient a_1 so that the effective forcing is

$$\frac{-2ia_1(curl_z \tilde{\tau})_0 e^{-\frac{\beta}{2(gh_1)^{\frac{1}{2}}} y^2} e^{i\omega t}}{\beta \rho H y_0 \left(\frac{\omega}{(gh_1)^{\frac{1}{2}}} - k\right)}$$

The projection coefficient a_1 is given by

$$a_1 = \frac{\int_{-\infty}^{\infty} e^{-\frac{\beta}{2(gh_1)^{\frac{1}{2}}} y^2} e^{-2\left(\frac{y}{y_0}\right)^2} dy}{\int_{-\infty}^{\infty} e^{-\frac{\beta}{2(gh_1)^{\frac{1}{2}}} y^2} e^{-\frac{\beta}{2(gh_1)^{\frac{1}{2}}} y^2} dy}$$

$$= \frac{1}{\left(\frac{1}{2} + \frac{(gh_1)^{\frac{1}{2}}}{\beta} \frac{\beta}{y_0^2}\right)^{\frac{1}{2}}} \approx 1.4 \quad (\text{for } y_0 \approx 1000\,km) .$$

If one now Fourier transforms (IV.16) zonally, and with

$$U(k) = \int_{-\infty}^{\infty} u_0 e^{ikx}\, dx \quad , \tag{IV.17}$$

and

$$F(k) = \int_{-\infty}^{\infty} (curl_z \underset{\sim}{\tau})_0 \, e^{-ikx}\, dx \quad , \tag{IV.18}$$

one has

$$U(k) = \frac{-2ia_1}{\beta \rho H y_0} \frac{F(k)}{\left(\frac{\omega}{(gh_1)^{\frac{1}{2}}} - k\right)} \quad . \tag{IV.19}$$

The Fourier inversion of (IV.19) yields

$$u_0 = \frac{-2ia_1}{\beta \rho H y_0 2\pi} \int_{-\infty}^{\infty} \frac{F(k)\, e^{ikx}}{\left(\frac{\omega}{(gh_1)^{\frac{1}{2}}} - k\right)} dk \quad . \tag{IV.20}$$

It was noted earlier in this section that Luther finds the 40- to 50- day oscillation to propagate eastward at planetary wavenumber s=1 or 2, with s=1 dominating (Madden and Julian (1971) find s=1), where s=(40,000km/2π)k (40,000 km is roughly the circumference of the earth). Thus, one might assume F(s) has a gaussian structure (a standard model for spectral line shapes) with halfwidth at s=2 (see Fig. IV.2). Thus, I assume

$$F(s) = F_0 \, e^{-\ln 2 (s-1)^2} \tag{IV.21}$$

To estimate the magnitude of u_0 friction is introduced since the

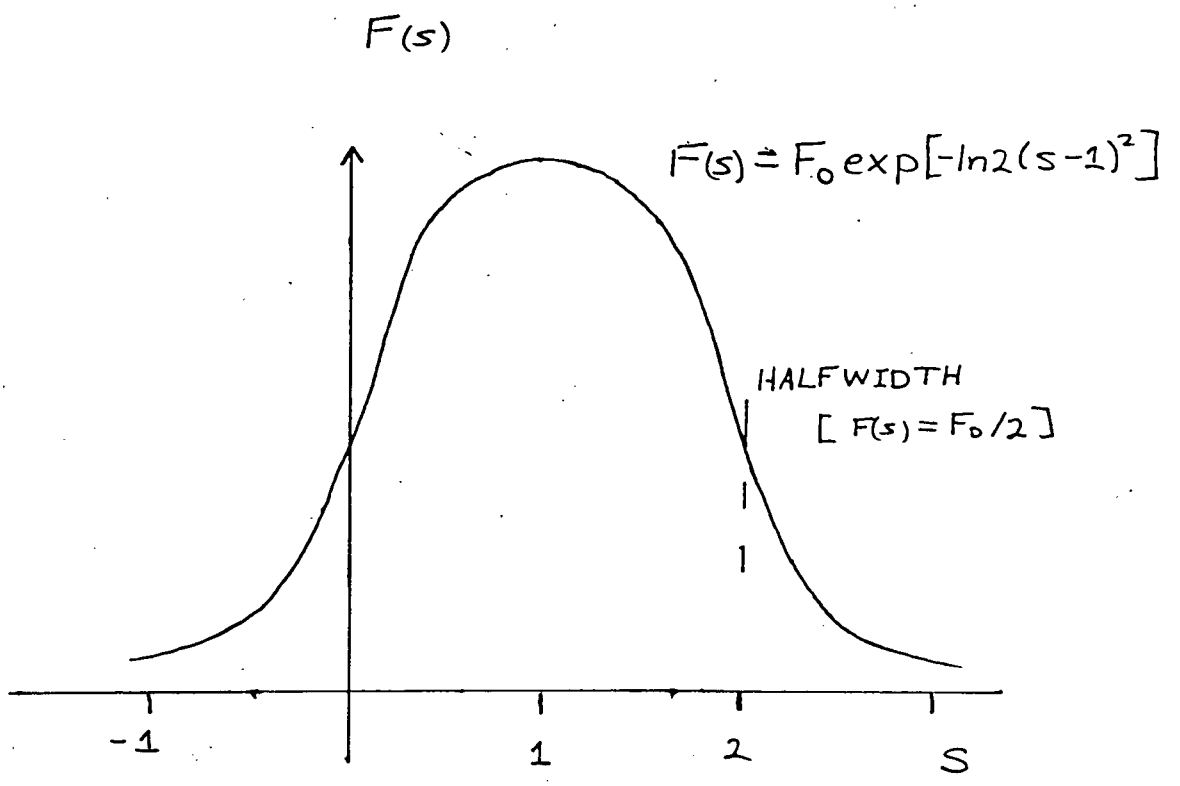

Fig.IV.2. The gaussian distribution of amplitude specified by equation(IV.21).

denominator in the integral of equation (IV.20) is zero when $k = \omega/(gh_1)^{\frac{1}{2}}$. This is done in an approximate manner so as not to unduly complicate the model. With friction , becomes complex , i.e.,

$$\omega \rightarrow \omega_r + i\omega_i$$

where ω_i represents the frictional terms. Vertical friction is represented by a vertical eddy diffusion coefficient, A_z, and horizontal friction by a horizontal eddy diffusion coefficient, A_h. Dimensionally, one requires an inverse time for the friction term ω_i. For the horizontal friction write

$$\omega_i)_h = \frac{\beta}{(gh_1)^{\frac{1}{2}}} A_h \qquad \text{(IV.22)}$$

and for the vertical friction write

$$\omega_i)_z = \frac{A_z}{\delta H} \qquad (\delta = \text{vertical length scale}) . \qquad \text{(IV.23)}$$

If one desires vertical friction to be represented by a bottom drag one chooses (see section (IV.6)) $\delta = \delta_{EKMAN} = \sqrt{\frac{2A_z}{f}}$. In LeBlond and Mysak (1978), estimates are given for bounds on A_h given by

$$10^2 \frac{m^2}{s} < A_h < 10^6 \ m^2/s$$

and bounds on A_z given by

$$3 \times 10^{-5} \ m^2/s < A_z < 2 \times 10^{-2} \ m^2/s$$

Thus the ranges for ω_i are:

$$10^{-9} s^{-1} < \omega_i)_h < 10^{-5} s^{-1}$$

$$6 \times 10^{-9} s^{-1} < \omega_i)_z < 10^{-7} s^{-1} .$$

One may now (somewhat arbitrarly)[5] choose an intermediate value of $\omega_i = 5\times10^{-8}\,m^2/s$. Equation(IV.20) is then

$$u_o = \frac{-2i\,a_1}{\beta\rho H y_o 2\pi}\int_{-\infty}^{\infty}\frac{F(k)\,e^{ikx}}{\left[\left(\frac{\omega}{(gh_1)^{\frac{1}{2}}}-k\right)+i\frac{\omega_i}{(gh_1)^{\frac{1}{2}}}\right]}\,dk$$

An estimate of the magnitude $|u_o|$ is given by

$$|u_o| \approx \frac{2a_1}{\beta\rho H y_o 2\pi}\int_{-\infty}^{\infty}\frac{F(k)\;dk}{\sqrt{\left(\frac{\omega}{(gh_1)^{\frac{1}{2}}}-k\right)^2+\left(\frac{\omega}{(gh_1)^{\frac{1}{2}}}\right)^2}} \qquad \text{(IV.24)}$$

The integral has a value of about 17 N/m^2, so that with $a_1 = 1.4$, $\beta \approx 2\times10^{-11}\ m^{-1}s^{-1}$, one finds

$$|u_o| \approx 16\,cm/s$$

This amplitude is sufficient to explain Luther's observed value of 8 cm/s. If the friction coefficient is made ten times larger the response drops to about 5 cm/s, still close to the observed

---

[5]Eddy coefficients tend to increase with the scale of phenomenon. Thus, I expect the horizontal coefficient to be large because the horizontal scale is large (~1000 km) but not too large since the strong gradient of planetary vorticity near the equator will tend to inhibit horizontal mixing. The vertical coefficient should tend toward the large end of the range since I am concerned with bottom fricition where stratification is weak.

strength. If the friction coefficient is decreased by a factor of ten the response increases to about 27cm/s, which is comparable to the strength observed by McPhaden in the Indian Ocean (about 25 cm/s). Thus, a link is established between the equatorial oceanic 40- to 50- day fluctuations and the global-scale atmospheric circulation cells first described by Madden and Julian (1972a).

IV.4 The Basin Response

Two sets of observations have established significant non-coastal and off-equatorial (outside the equatorial waveguide) fluctuations at 40- to 50-days: Hayes' (1979) observations and Düing and Schott's (1978) Somali Current observations. I now wish to try and explain these observations in terms of a basin-wide forced model. That is, I will look at the barotropic response of the whole Indian Ocean to the global-scale atmospheric circulation cells in the hope that a western-intensified response will be sufficiently strong to account for these oceanic oscillations. I use Düing's (1970) model of the Indian Ocean basin with periodic forcing (he examined the annual response ; I will specify a 50-day period). The model is illustrated in Fig.IV.3. This model is limited in that only the depth averaged (barotropic) responses are calculated. However, it is interesting to find the strength of the oceanic responses on the largest scales; that is, throughout the extent of a large oceanic basin and throughout the depth of the ocean (Hayes' observations were made near the bottom of the Pacific).

Following Düing I proceed from the vertically averaged equations of motion:

$$\frac{\partial \bar{U}}{\partial t} - f\bar{V} = -\frac{1}{\rho}\frac{\partial P}{\partial x} - k\bar{U} + \frac{\tau^{(x)}}{\rho H} \qquad \text{(IV.25a)}$$

$$\frac{\partial \bar{V}}{\partial t} + f\bar{U} = -\frac{1}{\rho}\frac{\partial P}{\partial y} - k\bar{V} + \frac{\tau^{(y)}}{\rho H} \qquad \text{(IV.25b)}$$

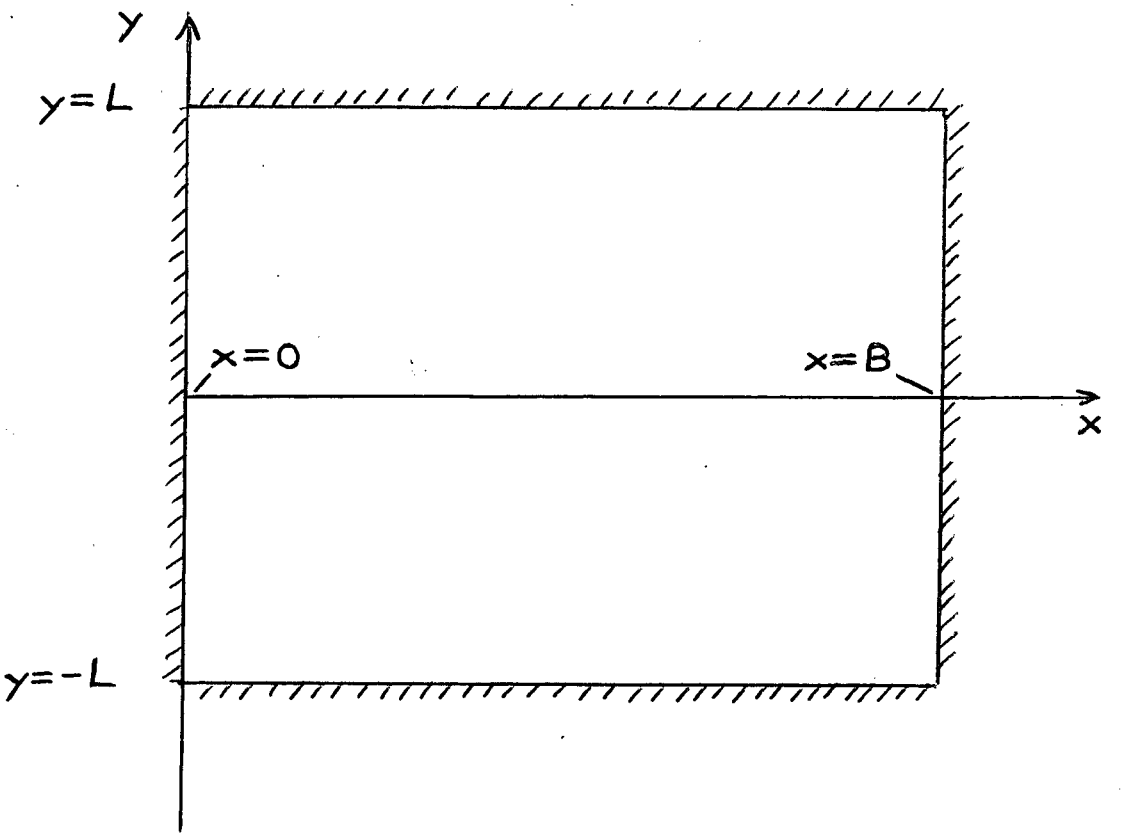

Fig.IV.3. The basin model. Parameters are fixed at L=1000 km, B=6000 km, H (depth)= 4000m, for purposes of calculation.

where $U = \frac{1}{H}\int_{-H}^{0} u\, dz$ is the vertically averaged (barotropic) x-component of the velocity, V, P are the corresponding averaged quantities, k is the bottom friction coefficient, and $\tau^{(x)}$, $\tau^{(y)}$ are the x and y components of the wind stress, respectively. Pedlosky (1979, p.238) notes that homogeneous models generally adequately reproduce the horizontal motions of large-scale oceanic circulation. Using the assumption of nondivergent flow (perhaps the most serious restriction for an equatorial model), a stream function ψ^* is introduced

$$V = \frac{\partial \psi^*}{\partial x} \qquad U = -\frac{\partial \psi^*}{\partial y} \tag{IV.26}$$

and cross differentiation of (IV.25) leads to

$$\frac{\partial}{\partial t}\nabla^2\psi^* + \beta\frac{\partial \psi^*}{\partial x} + k\nabla^2\psi^* = curl_z \tilde{\tau}/\rho H . \tag{IV.27}$$

I assume the forcing to be periodic with frequency $\omega = 2\pi/50\,DAYS$, and accordingly I write

$$\psi^*(x,y,t) = \psi(x,y)\, e^{i\omega t} . \tag{IV.28}$$

From equation (II.5) I note that

$$curl_z \tilde{\tau} = curl_z \tau\Big)_0 \frac{y}{y_0} \exp\left[-2\left(\frac{y}{y_0}\right)^2\right] e^{i\omega t}$$

(the x-dependence of the forcing is small since the wavelength of the global-scale oscillation is about 40,000 km). Thus the

governing dynamics are described by

$$(k+i\omega)\,\nabla^2\psi + \beta\frac{\partial\psi}{\partial x} = \frac{(curl_z\,\tilde{\tau})_o}{\rho H}\,\frac{\gamma}{\gamma_o}\,e^{-2\left(\frac{\gamma}{\gamma_o}\right)^2} \qquad \text{(IV.29)}$$

with corresponding boundary conditions (dictated by the no flow condition through the basin walls)

$$\psi(0,y) = \psi(B,x) = \psi(x,-L) = \psi(x,L) = 0 \qquad \text{(IV.30)}$$

I now decompose the forcing into a Fourier series:

$$(curl_z\,\tilde{\tau})_o\,\frac{\gamma}{\gamma_o}\,e^{-2\left(\frac{\gamma}{\gamma_o}\right)^2} = (curl_z\,\tilde{\tau})_o\sum_{n=1}^{\infty} a_n \sin\left[\frac{n\pi(y+L)}{2L}\right] \qquad \text{(IV.31)}$$

where

$$a_n = \int_{-L}^{L}\frac{\gamma}{\gamma_o}\,e^{-2\left(\frac{\gamma}{\gamma_o}\right)^2}\sin\left[\frac{n\pi(y+L)}{2L}\right]dy \qquad \text{(IV.32)}$$

The solution is now the sum of the responses to each Fourier component of the forcing (since this is a linear problem). Thus I find (using equation 29 , page 39 of Düing, 1970)

$$\psi = \frac{L^2(curl_z\,\tilde{\tau})_o}{\pi^2\rho H(k+i\omega)} \cdot \sum_{n=1}^{\infty}\frac{a_n}{n^2}\left[\frac{e^{\lambda_1 x}(e^{\lambda_2 B}-1)+e^{\lambda_2 x}(1-e^{\lambda_1 B})}{e^{\lambda_2 B}-e^{\lambda_1 B}} - 1\right] \qquad \text{(IV.33)}$$

where $\lambda_{1,2} = -\frac{a}{2} \pm \sqrt{\frac{a^2}{4} + c}$, $a = \frac{\beta}{k+i\omega}$, $c = \frac{n^2\pi^2}{L^2}$.

Numerical computation shows that a_n decreases approximately as $1/n$, so that the factor a_n/n^2 causes the sum to converge rapidly (5 terms are used to obtain the results that follow).

The sums (IV.31) are calculated and the results displayed in Fig.IV.4 . I have used a friction coefficient of $k=10^{-7}$ s^{-1} in these computations , which is in the mid-range of reasonable values suggested by Düing (parameter sensitivity studies indicate that the maximum response amplitudes are not too sensitive to the value of k , changing by a factor of 2 with a ten-fold variation of k). The results shown are both the stream function and the velocity magnitude $(U^2+V^2)^{1/2}$ for three different times: at t=0, $t=(\pi/4)(1/\omega)$, and $t=(\pi/2)(1/\omega)$. The units for the streamfunction plots (IV.4a,c,e) are m^2/s and 10^{-1} cm/s for the velocity magnitudes (IV.4b,d,f). The cellular patterns characterizing the stream function (IV.4a,c,e) shift from completely anti-symmetric at t=0 to fully symmetric at $t=(\pi/2)(1/\omega)$. Many cells are also evident in the velocity magnitude plots (IV.4b,d,f) , with maximum velocities of 2 cm/s evident in the westernmost cells . This maximum velocity is too small to account for the Somali Current observations at stations K1 and K2. These results may , however , be useful in explaining the observations of Hayes (1979) if the model can be applied to the Pacific. Examination of Fig.IV.5 shows that the region of Hayes' observations is roughly bounded by a basin formed by the Line Islands and East Pacific Rise on one side and the Americas on the other (the basin is about 6000 km long). If the model was

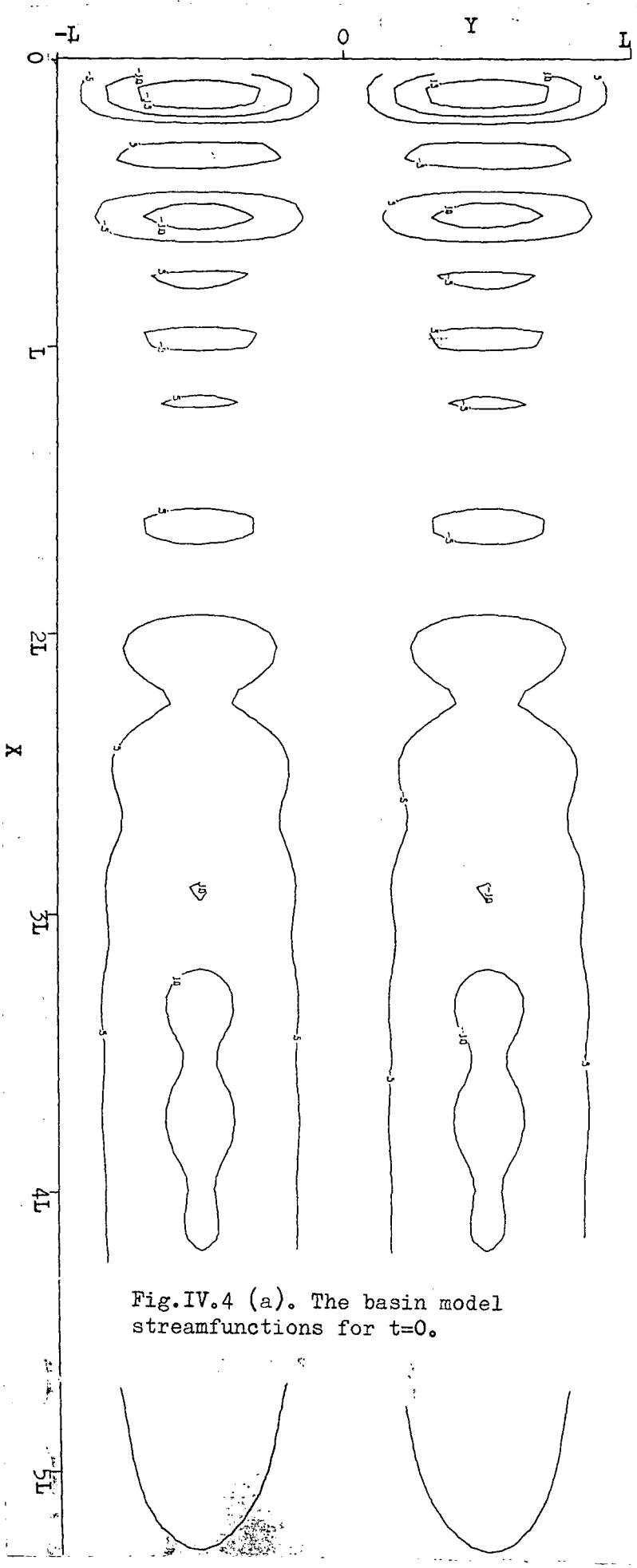

Fig.IV.4 (a). The basin model streamfunctions for t=0.

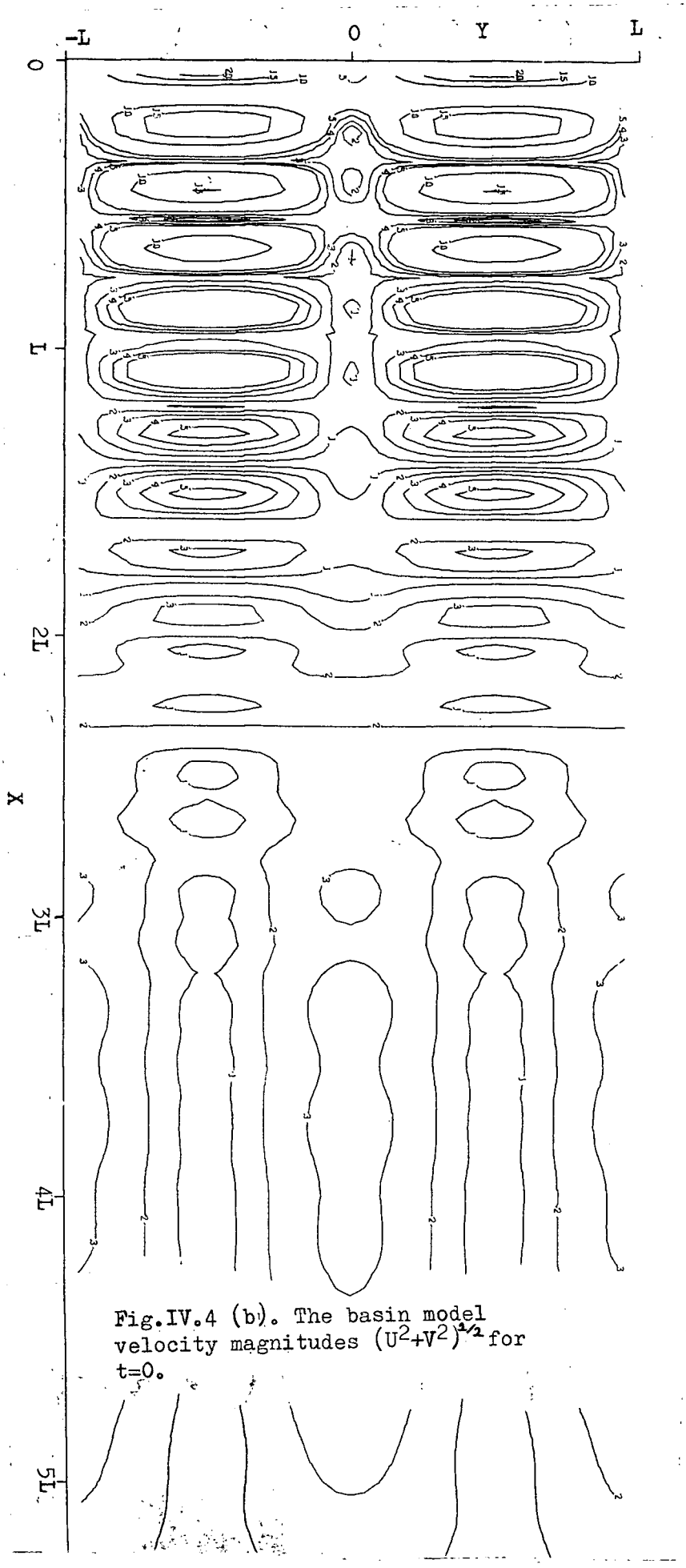

Fig.IV.4 (b). The basin model velocity magnitudes $(U^2+V^2)^{1/2}$ for t=0.

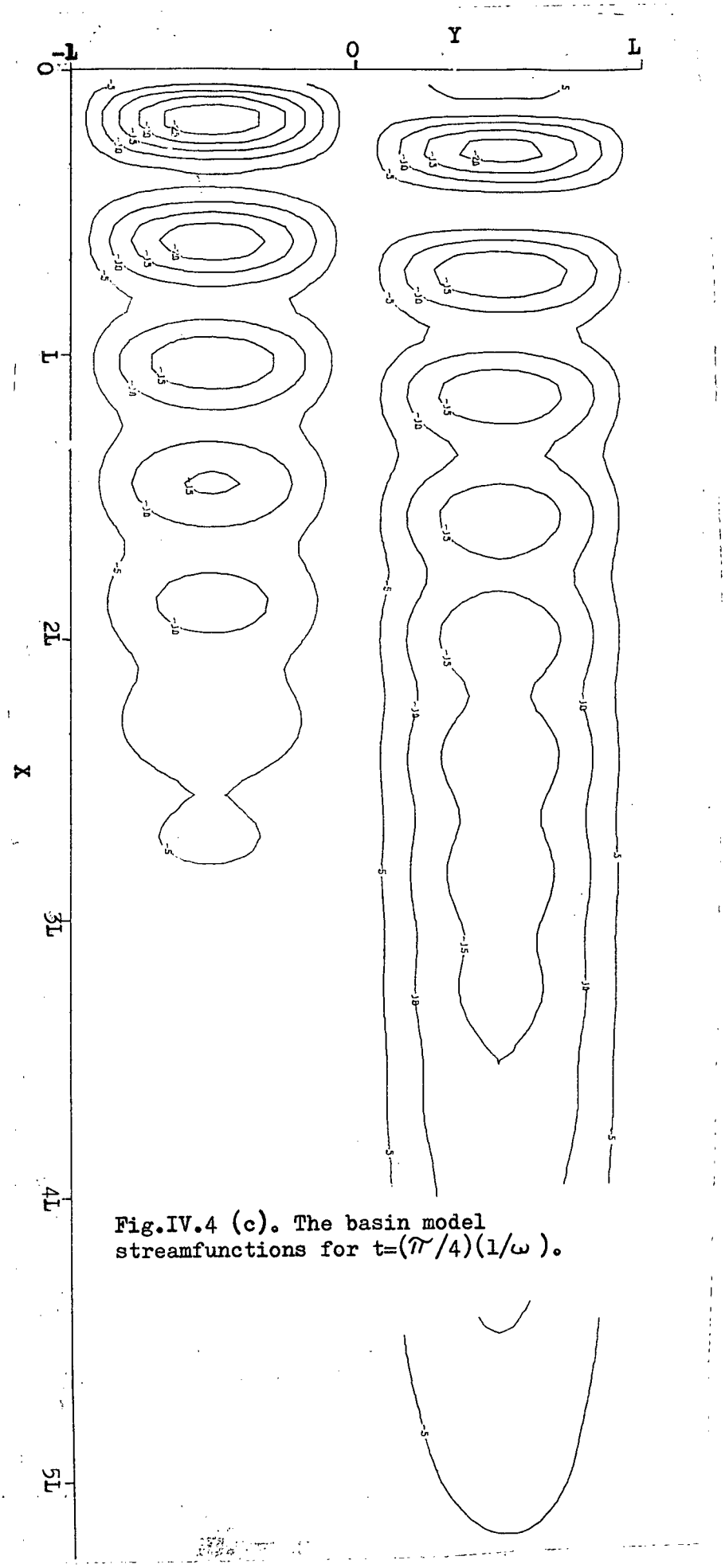

Fig.IV.4 (c). The basin model streamfunctions for $t=(\pi/4)(1/\omega)$.

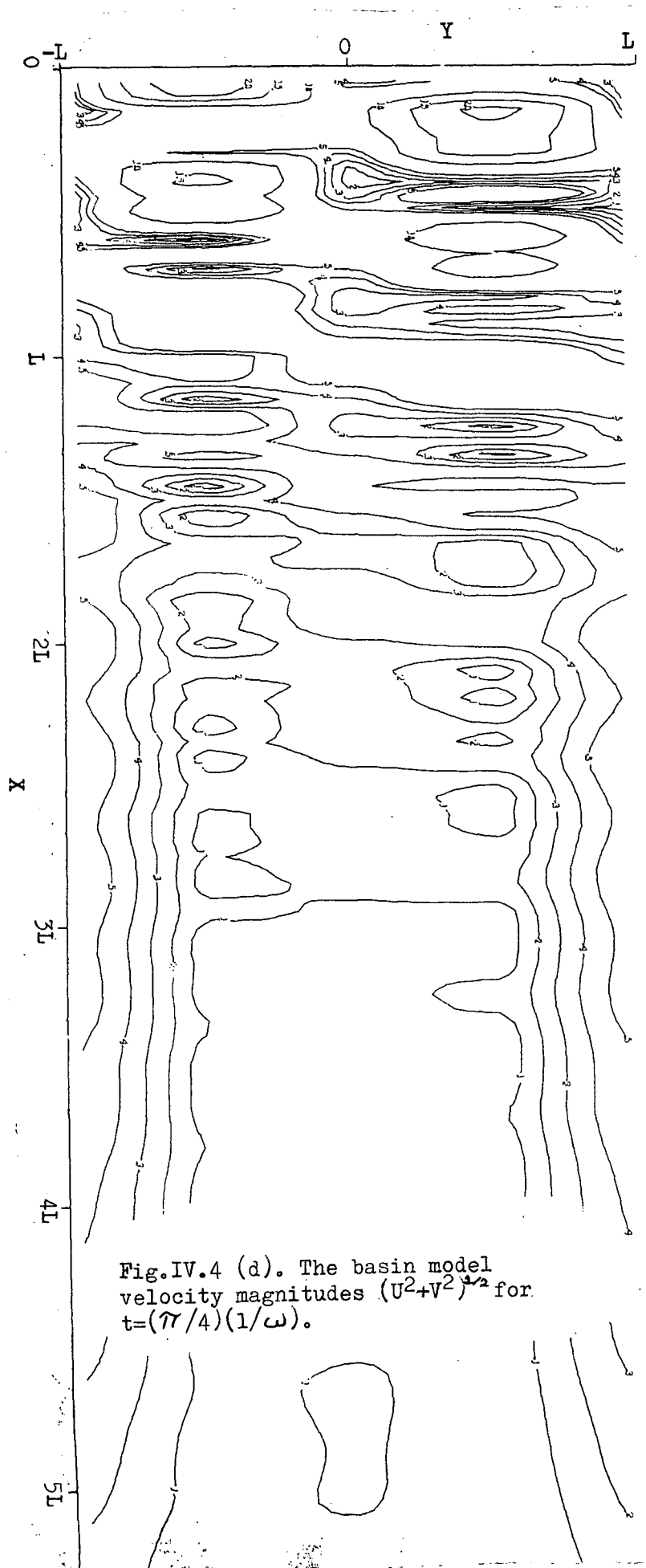

Fig.IV.4 (d). The basin model velocity magnitudes $(U^2+V^2)^{1/2}$ for $t=(\pi/4)(1/\omega)$.

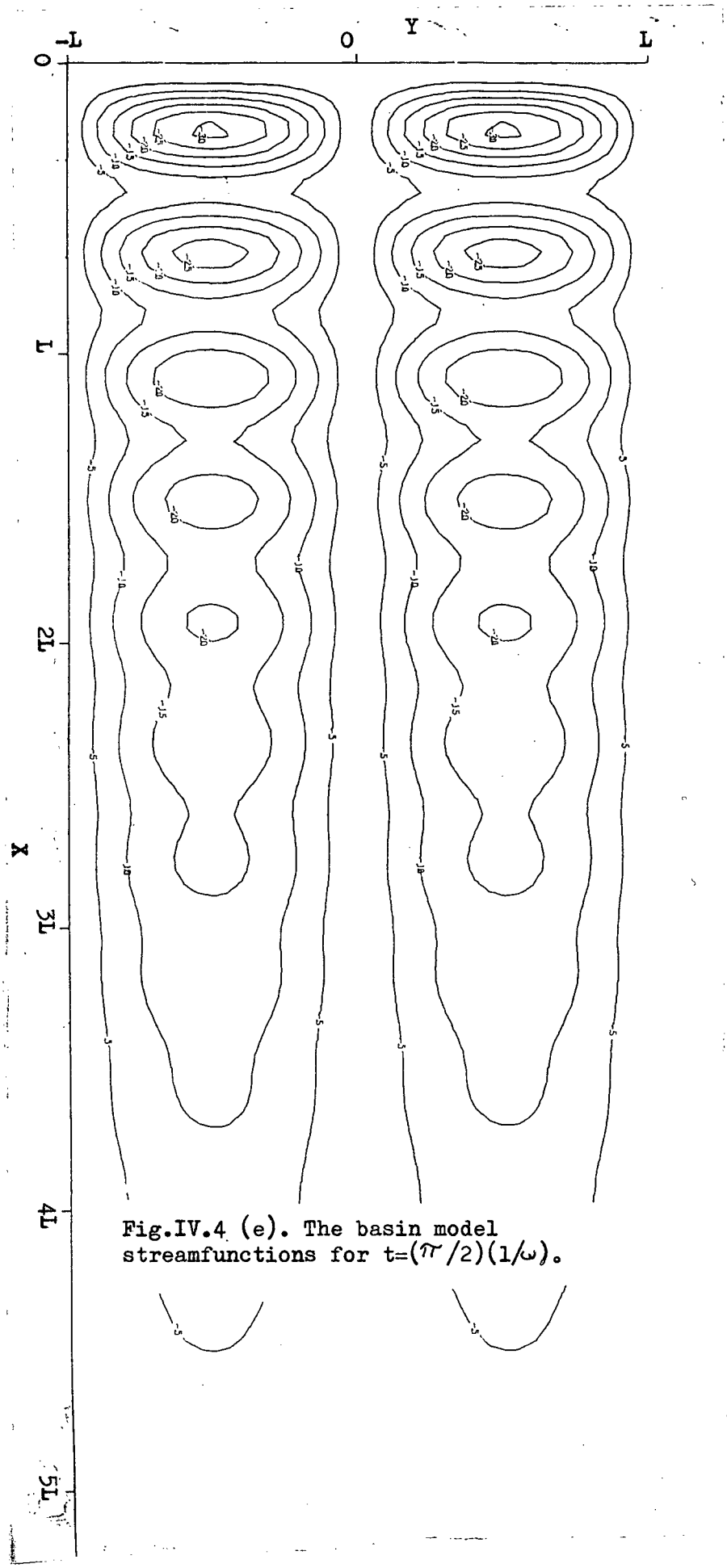

Fig.IV.4 (e). The basin model streamfunctions for $t=(\pi/2)(1/\omega)$.

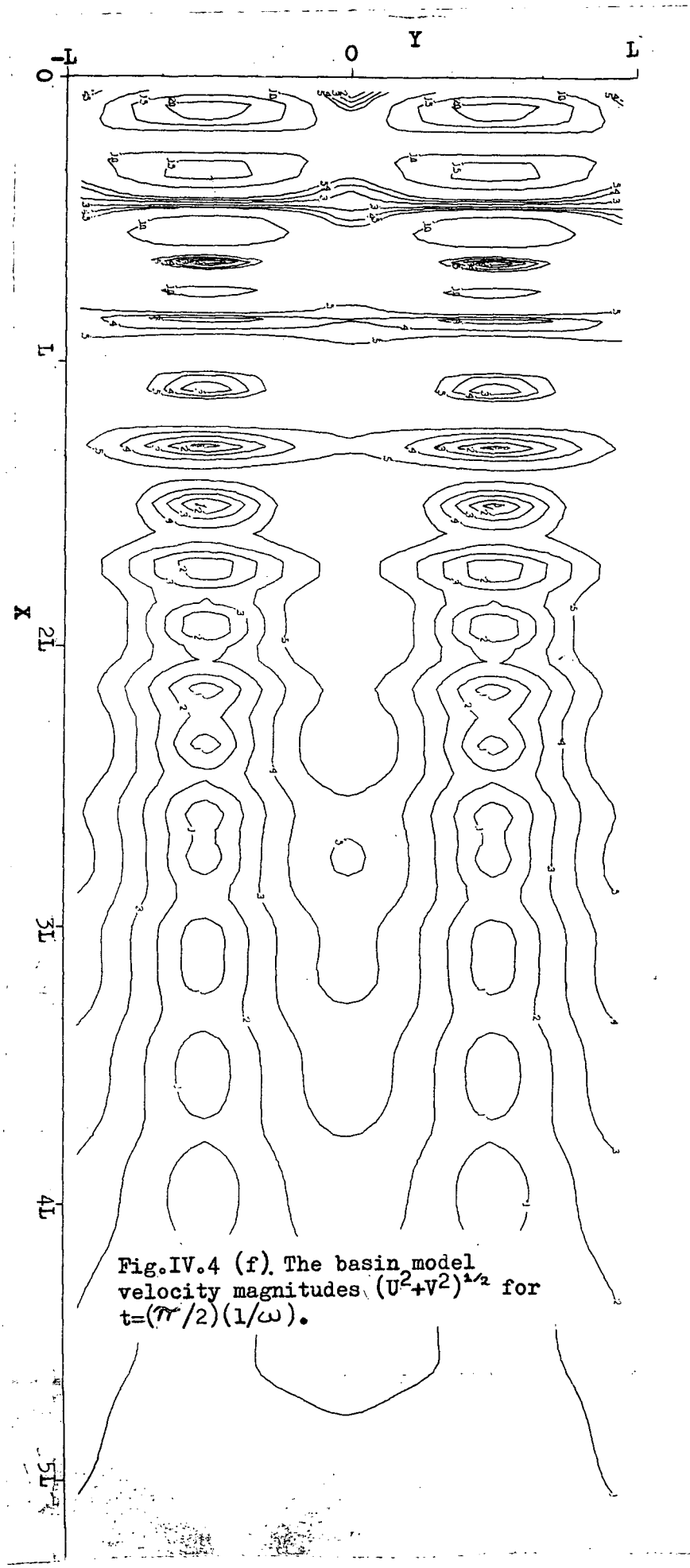

Fig.IV.4 (f). The basin model velocity magnitudes $(U^2+V^2)^{1/2}$ for $t=(\pi/2)(1/\omega)$.

applied here the results might explain the observation of 40- to 50-day energy at great depths. Hayes finds (see Fig.10, Table 1 of Hayes, 1979) meridional current oscillations near the bottom of the Pacific at sites B and C (see Fig.IV.5) with an approximate 2-month period and a strength of about 2 cm/s. There is much less 2-month energy at site A. The meridional orientation of the oscillations is unusual but fits with the basin model results where the strongest velocities are meridional. The basin model also predicts that 2 to 3 cm/s current oscillations can exist in the very deep ocean. The low amplitudes found at site A might indicate that this point is in the frictional boundary layer which would associated with the westward intensified currents.

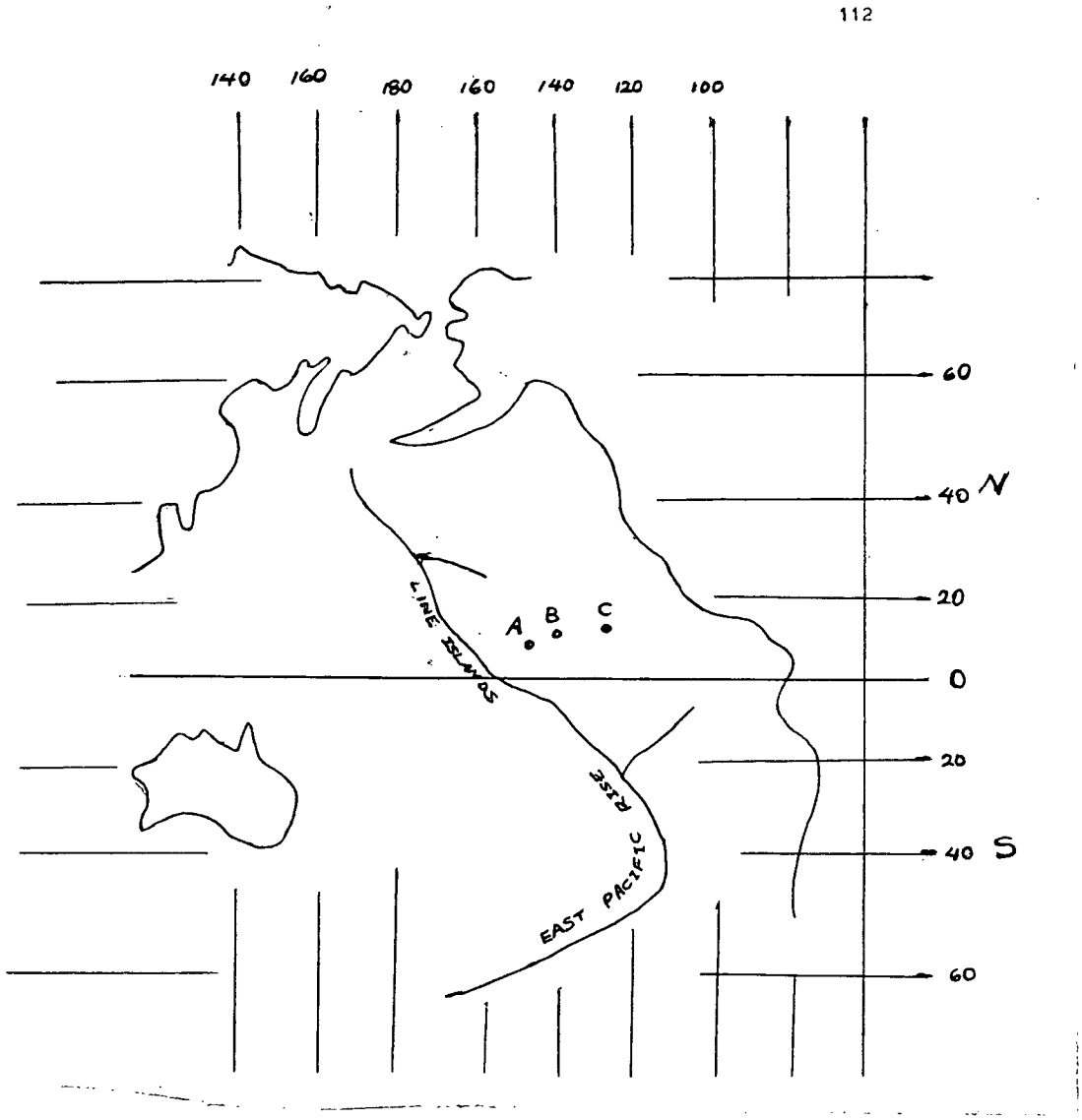

Fig.IV.5. Ocean ridges near sites A,B,C of Hayes' program. (Adapted from King, 1962).

IV.5 Upper Layer Dynamics

In this section I will examine the dynamics of a surface layer (i.e., a reduced-gravity model) forced by a 50-day wind oscillation in the coastal region. Specifically, in this section I will ignore coupling of the wind-driven layer to the deeper ocean (it will be shown that the rotational Froude number characterizing interlayer coupling is small). I will show, using Lee's (1975) forced solution of the Niiler-Mysak (1971) model, that the waveguide constituted by the Somali Current with lateral current shear responds to a 50-day atmospheric oscillation with more than sufficient strength to account for the observed current oscillations.

I start with the momentum and conservation of mass equations integrated over the surface layer which rests on fluid of slightly greater density below. Under these conditions a reduced gravity model applies (see Gill, 1982, pp.121,122) and the relevant equations are:

$$\frac{D}{Dt} u - f v = -g' h_x + \frac{\tau^{(x)}}{\rho H} \qquad \text{(IV.34a)}$$

$$\frac{D}{Dt} v + f u = -g' h_y + \frac{\tau^{(y)}}{\rho H} \qquad \text{(IV.34b)}$$

$$u_x + v_y = \frac{1}{H} \frac{\partial h}{\partial t} \qquad \text{(IV.34c)}$$

where x,y are the coordinates aligned with the current (and are thus not north-south), so that $f = \beta_{(x)} x + \beta_{(y)} y$

($\beta_{(x)} \equiv \partial f/\partial x$, $\beta_{(y)} \equiv \partial f/\partial y$)

H is the mean layer thickness (about 100m)

h is the total layer thickness (=H+layer perturbation)

$g' = \frac{\Delta\rho}{\rho} g$, with $\Delta\rho$ being the density difference between the top and bottom layers.

I will now show that the dynamics are essentially non-divergent; that is, the right hand side of (IV.34c) is negligible. The motions may be regarded as horizontally nondivergent if (Lee,1975) the time scale of the motion is large compared to $L/\sqrt{g'H}$ or equivalently, $\omega L/\sqrt{g'H} \ll 1$ (this parameter is effectively a rotational Froude number). If one chooses L as the current width, which Düing and Schott (1978) give as 100 km, and with ω corresponding to a 50-day oscillation ($\omega \approx 10^{-6} s^{-1}$) one finds $\omega L/\sqrt{g'H} \approx 0.1 \ll 1$. Thus, the motions may be regarded as horizontally nondivergent and from this it follows that interlayer coupling is weak. Next, linearization is performed according to

$$u \rightarrow u, \qquad v \rightarrow V(x)+v$$

where V(x) is the mean flow , possessing lateral shear, and then form the vorticity equation

$$\left(\frac{\partial}{\partial t} + \bar{V}\frac{\partial}{\partial y}\right)\zeta + u\bar{V}_{xx} + \beta_{(x)}u + \beta_{(y)}v = \mathrm{curl}_z \underset{\sim}{\tau}/\rho H \qquad \text{(IV.35)}$$

$$[\ \zeta \equiv v_x - u_y\ ]$$

From the data presented in Chapter III I now wish to estimate the size of various restoring force terms, that is all the terms balancing the term, $\left(\frac{\partial}{\partial t}+\bar{V}\frac{\partial}{\partial y}\right)\zeta$, in equation(IV.35). The relevant scales are

$$u = O(0.01\ m/s)$$

$$v = O(0.1\ m/s) \qquad \text{(IV.36)}$$

$$\beta_{(x)}\ ,\ \beta_{(y)} \approx 2\times 10^{-11}\ m^{-1}\ s^{-1}$$

(for a 45° inclination of the coastal waveguide $\beta_{(x)}$ and $\beta_{(y)}$ are equal)

To estimate the size of V_x and V_{xx} , I assume the mean flow to a have a half-sine profile of width 100 km, i.e., V(x)=1(m/s)sin(π x/100km). Thus,

$$\bar{V}_x = \frac{\pi}{100\ km}\ 1\ m/s\ \cos\left(\frac{\pi x}{100\ km}\right)$$

and

$$\bar{V}_{xx} = -\left(\frac{\pi}{100\ km}\right)^2\ 1\ m/s\ \sin\left(\frac{\pi x}{100\ km}\right) .$$

I thus choose as a scale for V_{xx}

$$\bar{V}_{xx} = O(10^{-9}\ m^{-1}s^{-1})$$

The estimates of the strength of the restoring force terms can now be completed:

$$u\bar{V}_{xx} = O(0.01\ m/s\cdot 10^{-9}\ m^{-1}s^{-1}) = O(10^{-11}\ s^{-2})$$

$$\beta_{(x)}u = O(2\times 10^{-11}\ m^{-1}s^{-1}\cdot 0.01\ m/s) = O(2\times 10^{-13}\ s^{-2}) \qquad \text{(IV.37)}$$

$$\beta_{(y)}v = O(2\times 10^{-11}\ m^{-1}s^{-1}\cdot 10^{-1}\ m/s) = O(2\times 10^{-12}\ s^{-12})$$

One might note that the above argument is particularly sensitive to the value of the current width chosen since this quantity is squared in the estimate of the term V_{xx} . In fact the width of the Somali Current is variable. Leetmaa (1973) finds a current width of 200 km in late April of 1971 based on direct current measurements across the Somali Current at 2°S. However, at this time the current in the upper layer has a strenth of about 2m/s (the width tends to increase with the current strength) so that even in this case the term uV_{xx} is still about two and a half times stronger than the next largest term $\beta_{(y)} v$. Thus, the dominant restoring force term is uV_{xx} so the effective balance becomes

$$\left(\frac{\partial}{\partial t} + \bar{V}\frac{\partial}{\partial y}\right)\xi + u\,\bar{V}_{xx} = curl_z \tau / \rho H \qquad \text{(IV.38)}$$

This equation obviously ignores variations of f despite the fact that one is near the equator. The scaling that eliminated β (variation of f) is in no way a "gimmick". The restoring force provided by the horizontal shear allows the waves to traverse a waveguide extending from 10°S to 10°N (at the peak strength of the Somali Current). One should emphasize that this waveguide crosses the equator with minimal leakage (see section (IV.7)). In contrast, waves depending on f for their restoring forces will leak into the equatorial waveguide and little energy will cross the equator (Anderson, 1981).

I now wish to introduce a streamfunction (ψ) defined by

$$Hu = -\frac{\partial \psi}{\partial y} \quad , \quad Hv = \frac{\partial \psi}{\partial x} \quad , \qquad \text{(IV.39)}$$

(H is assumed constant).

This procedure is justified since the motions have been shown to be effectively horizontally nondivergent.

Equation(IV.38) now becomes

$$\left(\frac{\partial}{\partial t} + \bar{V}\frac{\partial}{\partial y}\right)\nabla^2\psi - \bar{V}_{xx}\frac{\partial \psi}{\partial y} = \frac{1}{\rho}\,curl_z\,\underset{\sim}{\tau} \quad . \qquad \text{(IV.40)}$$

I will approach this problem via a model due to Niiler and Mysak (1971), whose forced solution was given by Lee (1975)[6]. The model is illustrated in Fig.IV.6. The term V_{xx} in equation(IV.40) now vanishes except at the discontinuites in V'(x) (at x=L,2L). Thus equation(IV.40) yields

$$\left(\frac{\partial}{\partial t} + \bar{V}\frac{\partial}{\partial y}\right)\nabla^2\psi = \frac{1}{\rho}\,curl_z\,\underset{\sim}{\tau} \qquad \text{(IV.41)}$$

in the regions 0<x<L, L<x<2L, x>2L.

In studying forced models it is often necessary to include the effects of friction, since, without friction, response amplitudes become infinite when the natural frequency of the driven system corresponds to the driving frequency (resonance condition) . Here, I will include a simple interlayer drag that

---

[6] Lee included the role of instability in the growth of forced waves. In the situation considered here, the waves are stable.

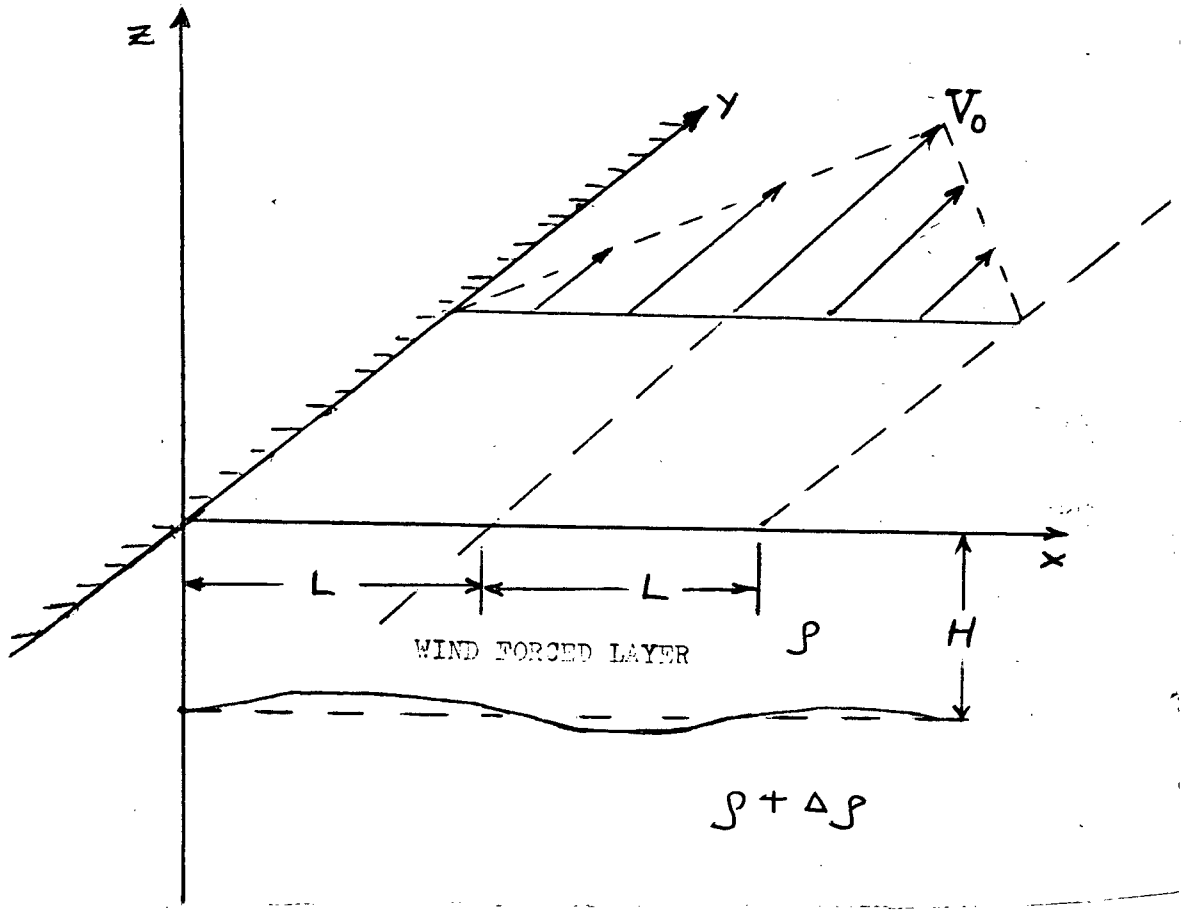

Fig.IV.6. The upper layer dynamics model.

requires no major modification of the governing dynamics (equation(IV.41)). With this drag the primitive momentum equations are

$$\left(\frac{\partial}{\partial t} + \bar{V}\frac{\partial}{\partial y}\right)u + fv + Ru = -p_x + \frac{\tau^{(x)}}{\rho H} \qquad \text{(IV.42a)}$$

$$\left(\frac{\partial}{\partial t} + \bar{V}\frac{\partial}{\partial y}\right)v - fu + Rv = -p_y + \frac{\tau^{(y)}}{\rho H} \qquad \text{(IV.42b)}$$

where R is the drag coefficient which is related to a nondimensional drag coefficient (C_I^*) by the equation (see p.145 in section IV.6)

$$R = \frac{C_I^* \bar{V}_s}{H}$$

where V_s is a velocity scale.

With the inclusion of friction equation(IV.42) becomes

$$\left(\frac{\partial}{\partial t} + R + \bar{V}\frac{\partial}{\partial y}\right)\nabla^2\psi = \frac{1}{\rho}\,\mathrm{curl}_z\,\underset{\sim}{\tau} \quad . \qquad \text{(IV.43)}$$

For the purposes of the calculation here I take (see p.145 below) $C_I^* = 3\times10^{-4}$. Equation (IV.43) is valid in each of the regions marked 1,2,3. The required boundary condition at the coastal edge of region 1 is

$$\psi_1(0,y,t) = 0 \qquad \text{(IV.44)}$$

since the coast must be a streamline. Matching conditions at x=L and x=2L are required . There the mass transport perpendicular to the coast and the surface displacements (pressure) must be

continuous (the matching condition for pressure can be found by integrating equation(IV.40) across a discontinuity in mean current velocity). These conditions may be expressed, respectively, as

$$\left\{ \psi(x) \right\}_-^+ = 0 \quad \text{at} \quad x = L, 2L$$
$$\left[\left\{ \psi(x) \right\}_-^+ \equiv \psi(x_+) - \psi(x_-) \right] \tag{IV.45}$$

and

$$\left\{ \left(\frac{\partial}{\partial t} + R + \bar{V} \frac{\partial}{\partial y} \right) \frac{\partial \psi}{\partial x} + \left(f + \frac{d\bar{V}}{dx} \right) \psi \right\}_-^+ = 0$$
$$\text{at} \quad x = L, 2L \,. \tag{IV.46}$$

In addition one requires that ψ be bounded as $x \to \infty$. Before proceeding, the equations are nondimensionalized as follows:

$$x = L x^* \,, \quad y = L y^* \,, \quad t = \frac{1}{f} t^*$$
$$\bar{V} = \bar{V}_0 \bar{V}^* \,, \quad \left(\tau^{(x)}, \tau^{(y)} \right) = \tau^\circ \left(\tau^{(x)*}, \tau^{(y)*} \right) \tag{IV.47}$$
$$\psi = \frac{\tau^\circ L}{\rho f} \psi^*$$

Then equation(IV.43) (after dropping the asterisks) becomes

$$\left(\frac{\partial}{\partial t} + R + \lambda \bar{V} \frac{\partial}{\partial y} \right) \nabla^2 \psi = \text{curl}_z \underset{\sim}{\tau} \tag{IV.48}$$

where $\lambda = \bar{V}_o/fL$ is the Rossby number and the nondimensional friction and forcing terms are given by

$$R)_{Nondimensional} = R/f$$

$$curl_z \tilde{\tau})_{Nondimensional} = \frac{L}{\tau_o} curl_z \tilde{\tau} \quad . \tag{IV.49}$$

The boundary and matching conditions are

$$\psi(0,y,t) = 0$$

$$\left\{ \psi(1,y,t) \right\}_-^+ = \left\{ \psi(2,y,t) \right\}_-^+ = 0 \tag{IV.50}$$

$$\left\{ \left(\frac{\partial}{\partial t} + R + \lambda \bar{V} \frac{\partial}{\partial y} \right) \frac{\partial \psi}{\partial x} - \left(1 + \lambda \frac{d\bar{V}}{dx} \right) \psi \right\}_-^+ = 0 \quad .$$

For the model in Fig. IV.6 one has

$$\bar{V}(x) = \begin{cases} x & 0 < x < 1 \\ 2-x & 1 \leq x \leq 2 \\ 0 & x > 2 \end{cases} \quad . \tag{IV.51}$$

I will now look for plane wave solutions of the problem. For a forcing function that represents a plane wave travelling parallel to the coast (see Chapter II), it follows that

$$curl_z \tilde{\tau} = c_o e^{i(ky - \omega t)} \tag{IV.52}$$

(assuming the wind forcing is constant in the x-direction). Thus, I look for corresponding solutions of the form

$$\psi(x,y,t) = \psi_0(x)\, e^{i(ky-\omega t)} \qquad \text{(IV.53)}$$

With these specifications equations (IV.48) and (IV.50) give

$$(\omega - iR - \lambda\bar{V}k)\left(\frac{\partial^2\psi}{\partial x^2} - k^2\psi\right) = -i\,C_0 \qquad \text{(IV.54a)}$$

$$\left\{(\omega - iR - \lambda\bar{V}k)\frac{\partial\psi}{\partial x} + k\left(1 + \lambda\frac{\partial\bar{V}}{\partial x}\right)\psi\right\}_-^+ = 0 \qquad \text{(IV.54b)}$$

at x=1,2

with ψ now a function of x,k, and ω, i.e., $\psi = \psi(x,k,\omega)$. In Lee (1975), these equations are solved for the model specified by equation(IV.51). Lee proceeds as follows:

Denote the solutions of equation(IV.54) in region i by ψ_i. It is possible to find particular solutions of equation(IV.54) that satisfy

$$\psi_{1p}(0,k,\omega) = \psi_{1p}(1,k,\omega) = \psi_{2p}(1,k,\omega) = \psi_{2p}(2,k,\omega) = \psi_{3p}(2,k,\omega) = 0 \qquad \text{(IV.55)}$$

and which are bounded as $x \to \infty$. They are given by

$$\psi_{1p}(x,k,\omega) = \frac{i\,C_0}{k\sinh k}\left[\sinh k \int_x^1 \frac{\sinh[k(1-\xi)]\,d\xi}{[\omega - iR - \lambda k\bar{V}(\xi)]} + \sinh[k(1-x)]\int_0^x \frac{\sinh(k\xi)}{[\omega - iR - k\lambda\bar{V}(\xi)]}\,d\xi\right], \qquad \text{(IV.56a)}$$

$$\psi_{2p}(x,k,\omega) = \frac{iC_0}{k\sinh k}\left[\sinh[k(x-1)]\int_x^2 \frac{\sinh(k\xi)}{[\omega - iR - \lambda k\bar{V}(\xi)]}\,d\xi + \sinh[k(x-2)]\int_1^x \frac{\sinh[k(\xi-1)]}{[\omega - iR - \lambda k\bar{V}(\xi)]}\,d\xi\right] \quad \text{(IV.56b)}$$

$$\psi_{3p}(x,k,\omega) = -iC_0\exp[-|k|(x-2)] \cdot \left[\cosh[k(x-2)] - \sinh[k(x-2)]\right] + iC_0\exp[-|k|(x-2)]/\omega k^2 \quad \text{(IV.56c)}$$

Now the solutions of equation(IV.54) that are continuous at x=1 and x=2 are

$$\psi_1(x,k,\omega) = A(k,\omega)\sinh kx + \psi_{1p}(x,k,\omega) \quad \text{(IV.57a)}$$

$$\psi_2(x,k,\omega) = A(k,\omega)\sinh kx + B(k,\omega)\sinh[k(x-1)] + \psi_{2p}(x,k,\omega) \quad \text{(IV.57b)}$$

$$\psi_3(x,k,\omega) = \exp[-|k|(x-2)] \cdot [A(k,\omega)\sinh 2k + B(k,\omega)\sinh k] + \psi_{3p}(x,k,\omega) \quad \text{(IV.57c)}$$

The functions A(k,ω) and B(k,ω) can be found by applying the matching conditions at x=1 and x=2. The equations thus derived may be written

$$\alpha_{11}A + \alpha_{12}B = b_1$$
$$\alpha_{21}A + \alpha_{22}B = b_2 \quad \text{(IV.58)}$$

where

$$\alpha_{11} = 2\lambda \sinh k$$
$$\alpha_{12} = -(\omega - iR - \lambda k)$$
$$\alpha_{21} = \omega e^{|k|} - \lambda \sinh k \qquad \text{(IV.59)}$$
$$b_1 = \frac{(\omega - iR - \lambda k)}{k}\left[\psi_{2P_x}(1,k,\omega) - \psi_{1P_x}(1,k,\omega)\right]$$
$$b_2 = \frac{\omega}{k}\left[\psi_{3P_x}(2,k,\omega) - \psi_{2P_x}(1,k,\omega)\right]$$

Equations(IV.58) have solutions

$$A = (b_1\alpha_{22} - b_2\alpha_{12})/\Delta$$
$$\text{(IV.60)}$$
$$B = (b_1\alpha_{11} - b_1\alpha_{21})/\Delta$$

where

$$\Delta(k,s) = \alpha_{11}\alpha_{22} - \alpha_{21}\alpha_{12} \quad . \qquad \text{(IV.61)}$$

The solutions are illustrated in Fig. IV.7a,b,c,d,e,f,g,h. Shown here are the nondimensional streamfunction (ψ) and the nondimensional longshore velocity ($= \psi_x$) calculated on the basis of L=10^5m , $\text{curl}_z\underset{\sim}{\tau}_{DIMENSIONAL}$ =5×10^{-8} Nt/m^3 (the peak value in Fig.III.7b) for the cases k=0.2,0.4,0.6,0.8. To obtain the dimensional longshore velocity one multiplies the nondimensional velocity by the scale factor $\frac{L}{\rho H f}\text{curl}_z\underset{\sim}{\tau} \approx 0.5$cm/s. The response curves show fairly complicated behavior arising from the superposition of the particular and homogeneous solutions. The resonant wavenumbers for 50-day forcing (Δ =0 in IV.60) are k=0.2,0.6, and at these wavenumbers the longshore velocity response is largest, although strong responses are observed in all cases. Indeed, the response is generally of the order of

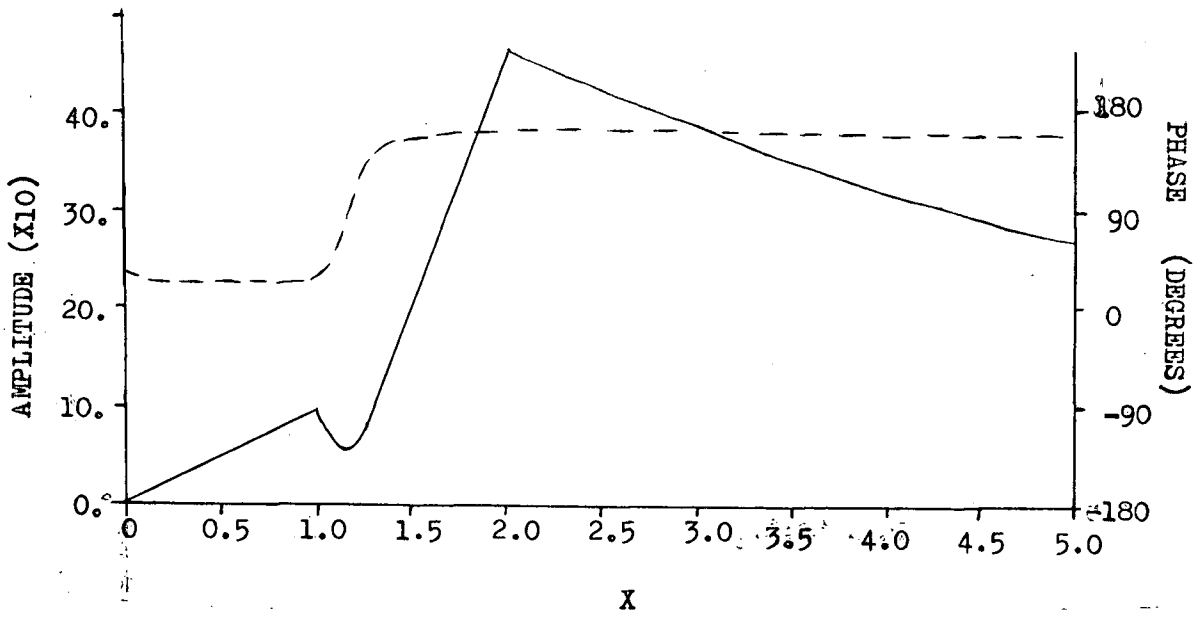

Fig.IV.7 (a). Nondimensional streamfunction , amplitude (solid line) and phase (dashed line) for the forced shear modes for the case k=0.2. The current profile is given in equation (IV.51); the peaks of the amplitude at x=1,2 correspond to the discontinuities in V .

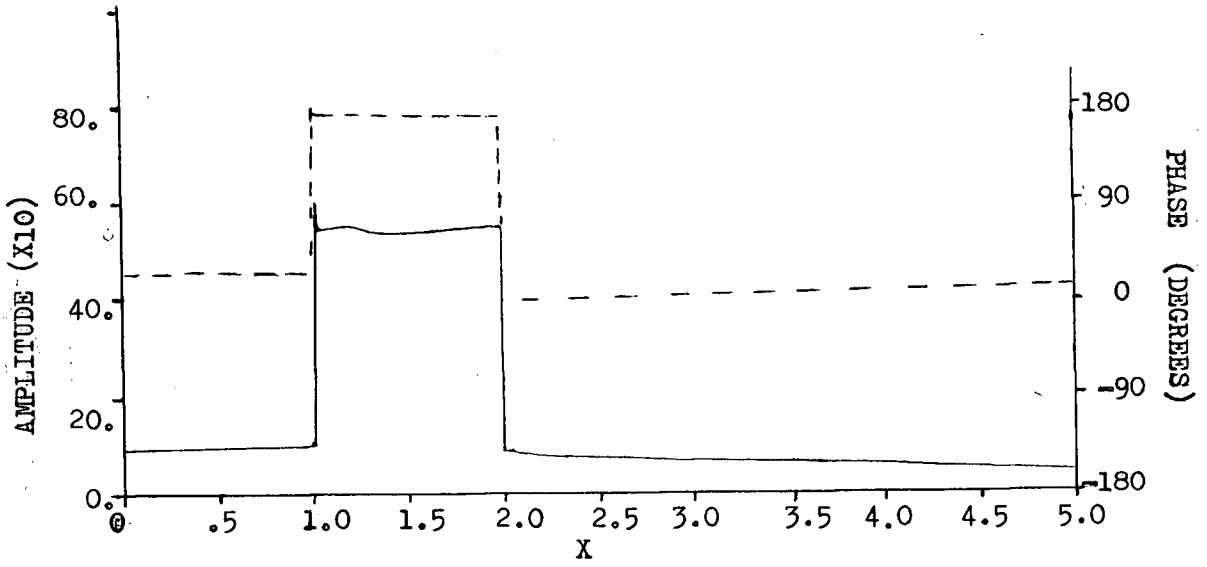

Fig.IV.7 (b). Nondimensional longshore velocity, amplitude (solid line)and phase (dashed line) for the forced shear modes for the case k=0.2.

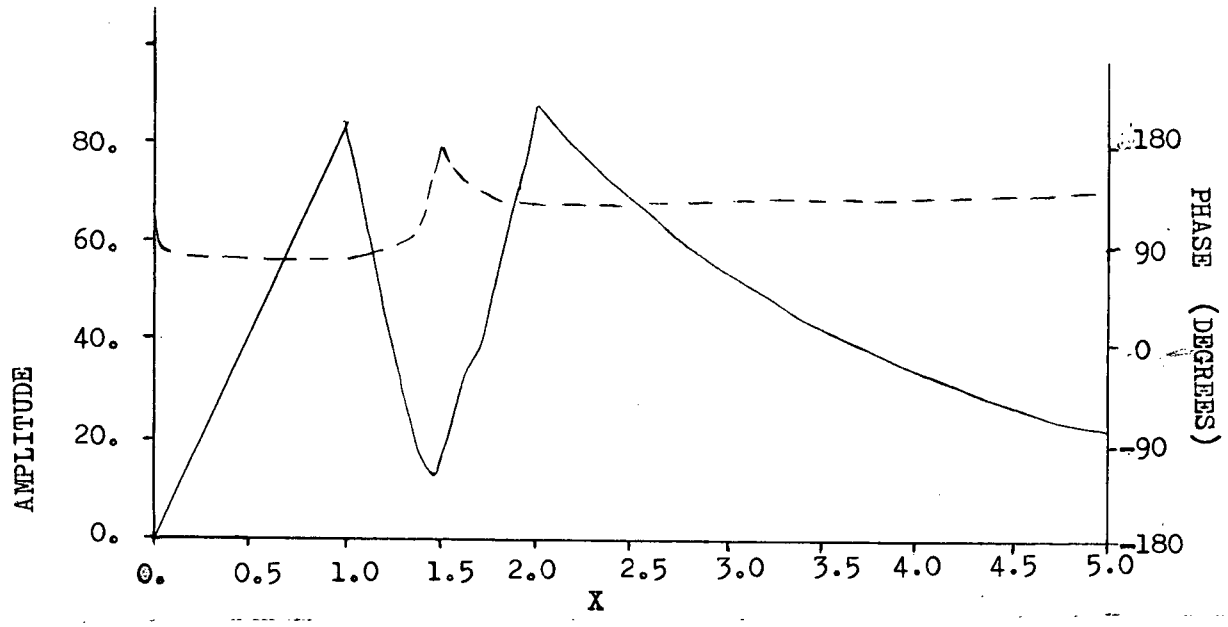

Fig.IV.7 (c). As in (a) , except for the case k=0.4.

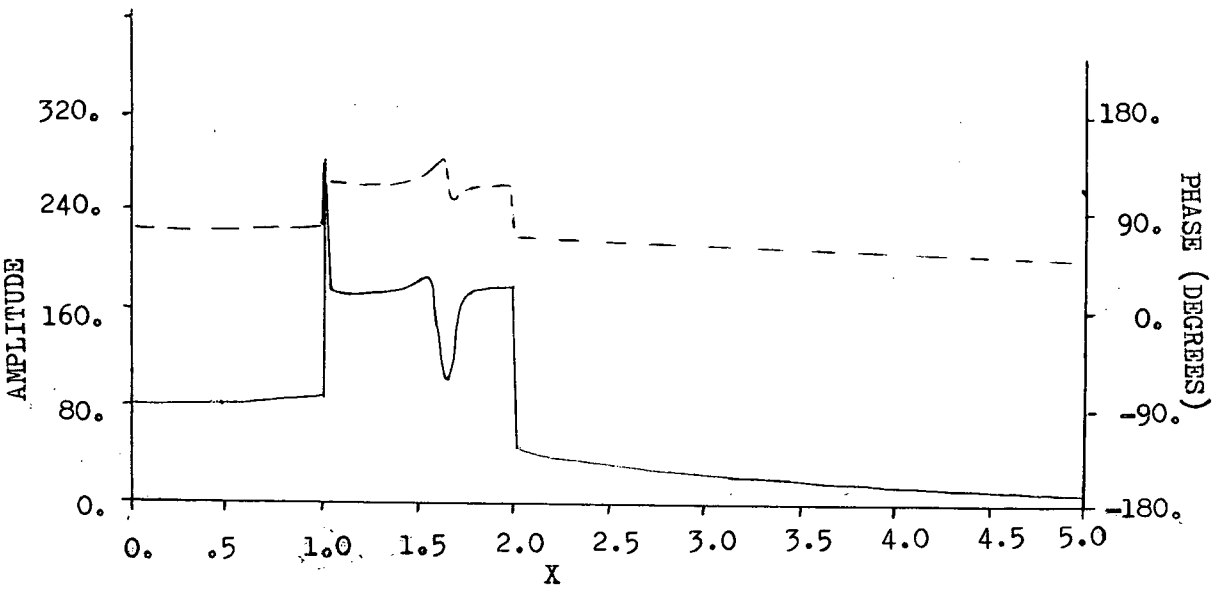

Fig.IV.7 (d). As in (b), except for the case k=0.4.

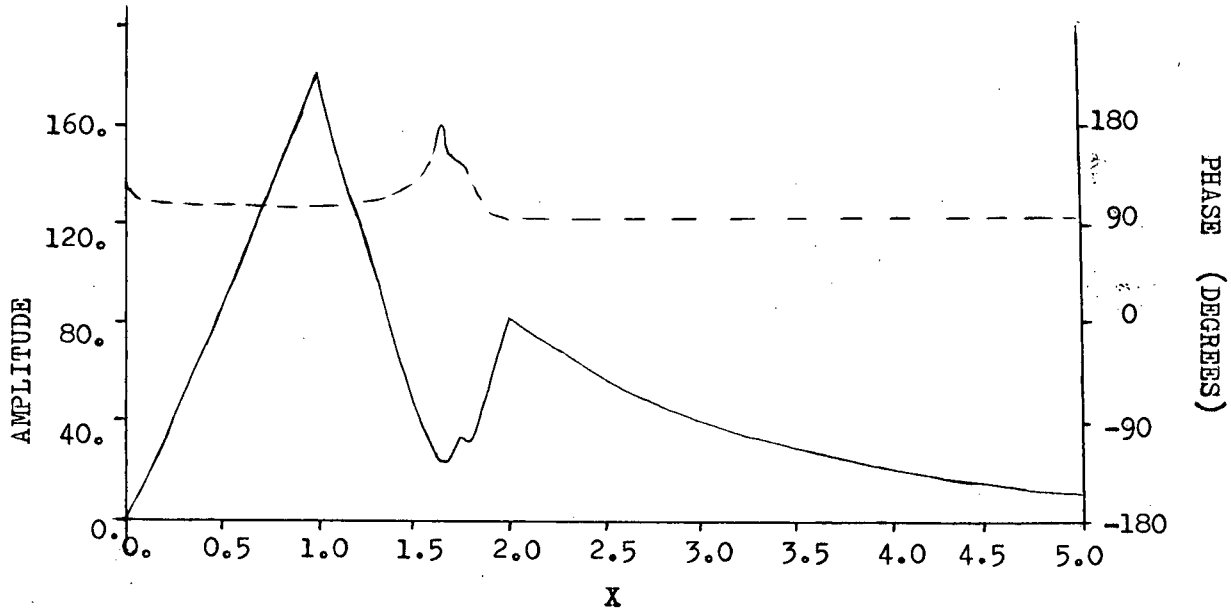

Fig. IV.7 (e). As in (a), except for the case k=0.6.

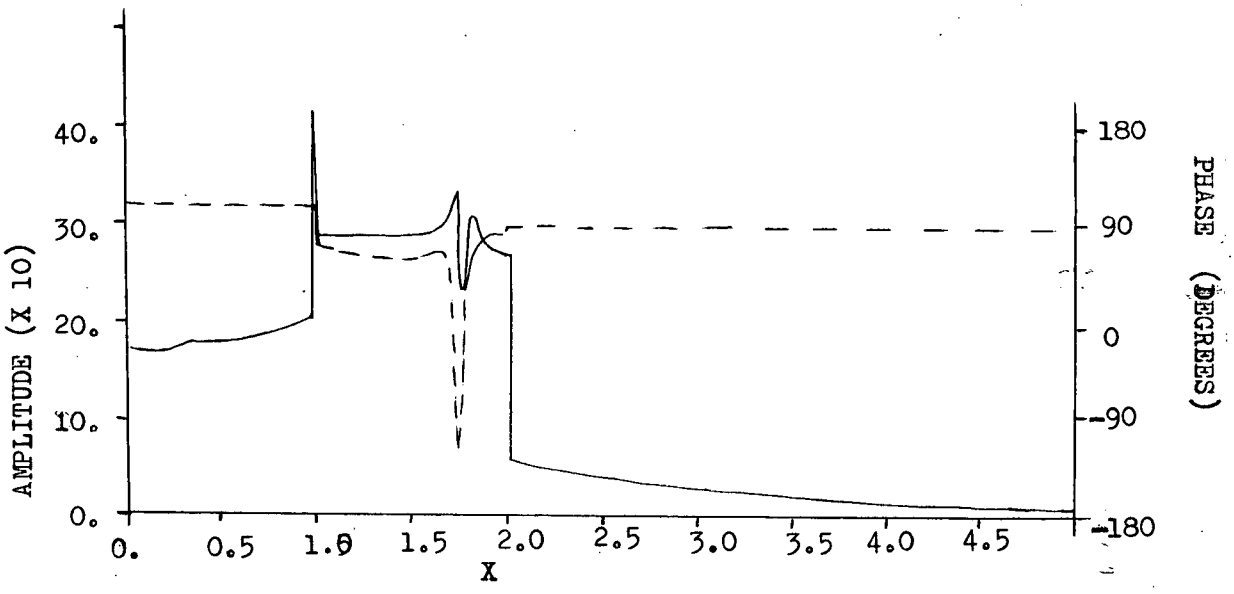

Fig.IV.7 (f). As in (b), except for the case k=0.6.

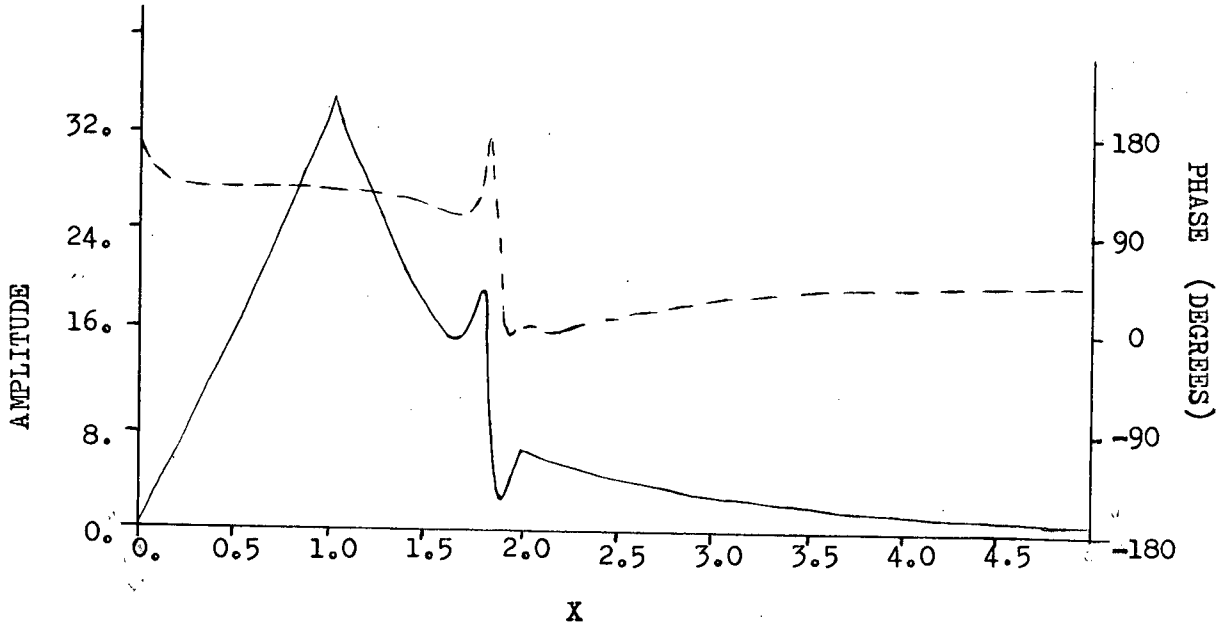

Fig.IV.7 (g). As in (a), except for the case k=0.8.

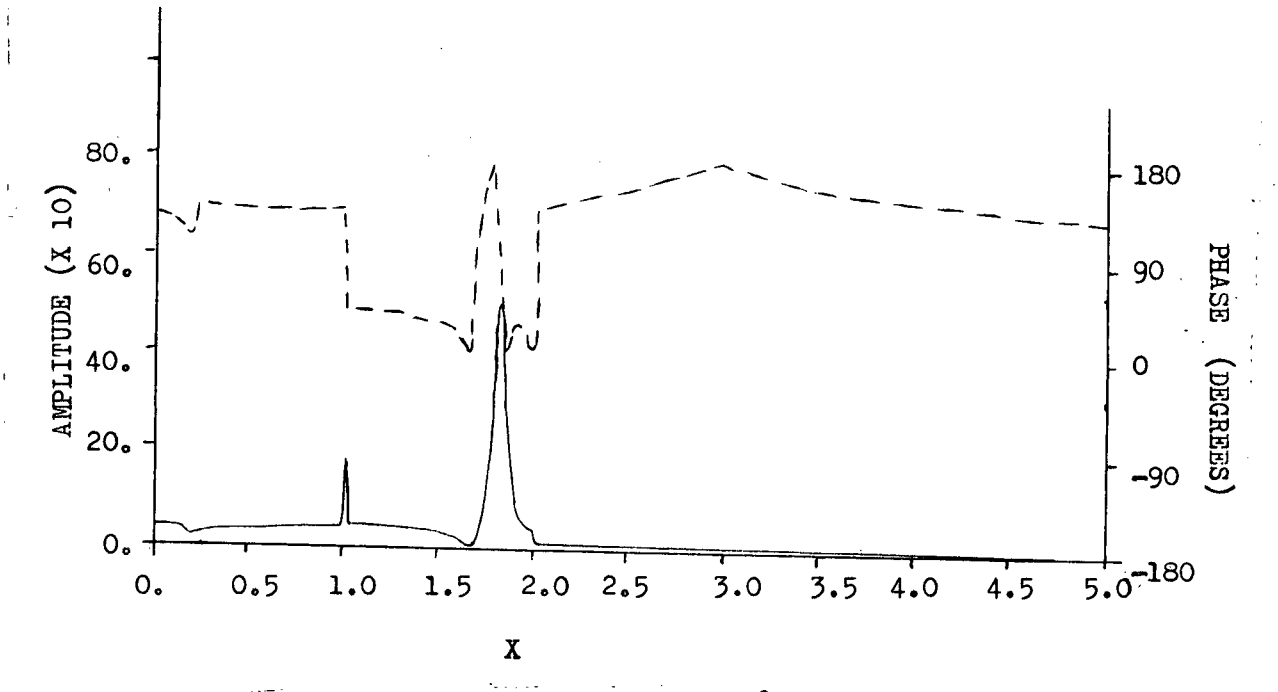

Fig.IV.7 (h). As in (b), except for the case k=0.8.

100cm/s or more at the peaks. This is undoubtedly an overestimate of the response , due to the inclusion of an excessively large potential vorticity gradient in the model. That is, the wind induced transports across the potential vorticity gradient give rise to effective forces (like the topographic forcing caused by Ekman transports) and I have assumed a delta function spike in the potential vorticity gradient (at x=L,2L where the derivative of the mean velocity changes sharply). One sees that this effect gives rise to very sharp jumps in the longshore velocity response, so that horizontal friction would be very effective in limiting the response in this model. A rough estimate of the effect can be made by noting that with horizontal friction the governing dynamics is described by

$$u_t - fv + A_h u_{yy} = \frac{-p_x}{\rho} + \frac{\tau^{(x)}}{\rho} \qquad \text{(IV.62a)}$$

$$v_t + fu + A_h v_{xx} = \frac{-p_y}{\rho} + \frac{\tau^{(y)}}{\rho} \qquad \text{(IV.62b)}$$

where A_h is the horizontal eddy coefficient. The vorticity equation would then become

$$i\omega \nabla^2 \psi + A_h \nabla^4 \psi = \text{curl}_z \underset{\sim}{\tau} \quad . \qquad \text{(IV.63)}$$

I now approximate the sharp change in the wavefunction across the mean flow region with a half sine profile ,$\sin(\pi x/2L)$. The friction term can now be written as $\left[k^2 + \left(\frac{\pi}{2L}\right)^2\right] A_h \nabla^2 \psi$, so

that (IV.63) becomes

$$\left\{ i\omega + \left[k^2 + \left(\frac{\pi}{2L}\right)^2\right] A_h \right\} \nabla^2 \psi = \mathrm{curl}_z \underset{\sim}{\tau}$$

Thus the required inverse time scale representing the friction is $(\pi/2L)^2 A_h$, with the range of A_h specified by (see section IV.3)

$$10^2 \ m^2/s < A_h < 10^6 \ m^2/s$$

It is appropriate to look at the large end of this range since I have minimized the estimate of large shear. The inverse time scale for friction becomes

$$\left(\frac{\pi^2}{2 \cdot 10^5}\right)^2 10^6 \cong 10^{-4} \ s^{-1} \ .$$

This is much larger than the scale provided by interlayer drag, which has a value of about $3 \times 10^{-7} s^{-1}$. Thus the inclusion of horizontal friction would significantly decrease the (excessive) model responses giving current amplitudes more like those observed by Düing and Schott (1978) in the coastal region.

(IV.6) Multilayer Dynamics

In this section I will concentrate on the vertical structure of the response of the Somali waveguide to local atmospheric forcing . Accordingly, I will develop a multi-layer model in order that the vertical variations of the response be modelled.

I will now derive the multi-layer equations necessary to describe the quasi-geostrophic response of the ocean to atmospheric forcing. The equations for an incompressible, non-diffusive, Boussinesq fluid in hydrostatic equilibrium will be derived in considerable generality: I will allow an arbitrary number of layers and will include vertical friction, although I will ignore horizontal friction and the β-effect (the reasons for ignoring the β-effect will be discussed after the model formulation). The physical situation is illustrated in Fig.IV.8. The vertically integrated equations governing the motion of each layer are, following McNider and O'Brien (1973): Conservation of horizontal momentum:

$$\frac{D}{Dt} u_j - f v_j = - \frac{p_{jx}}{\rho_j} + (\tau_j^{Tx} - \tau_j^{Bx}) / \rho_j h_j \qquad \text{(IV.64a)}$$

$$\frac{D}{Dt} v_j + f u_j = - \frac{p_{jy}}{\rho_j} + (\tau_j^{Ty} - \tau_j^{By}) / \rho_j h_j \qquad \text{(IV.64b)}$$

Conservation of vertical momentum (hydrostatic assumption):

$$p_n = g \sum_{j=1}^{n-1} \rho_j h_j + g \rho_n (\eta_n - z + H_n) \quad . \qquad \text{(IV.64c)}$$

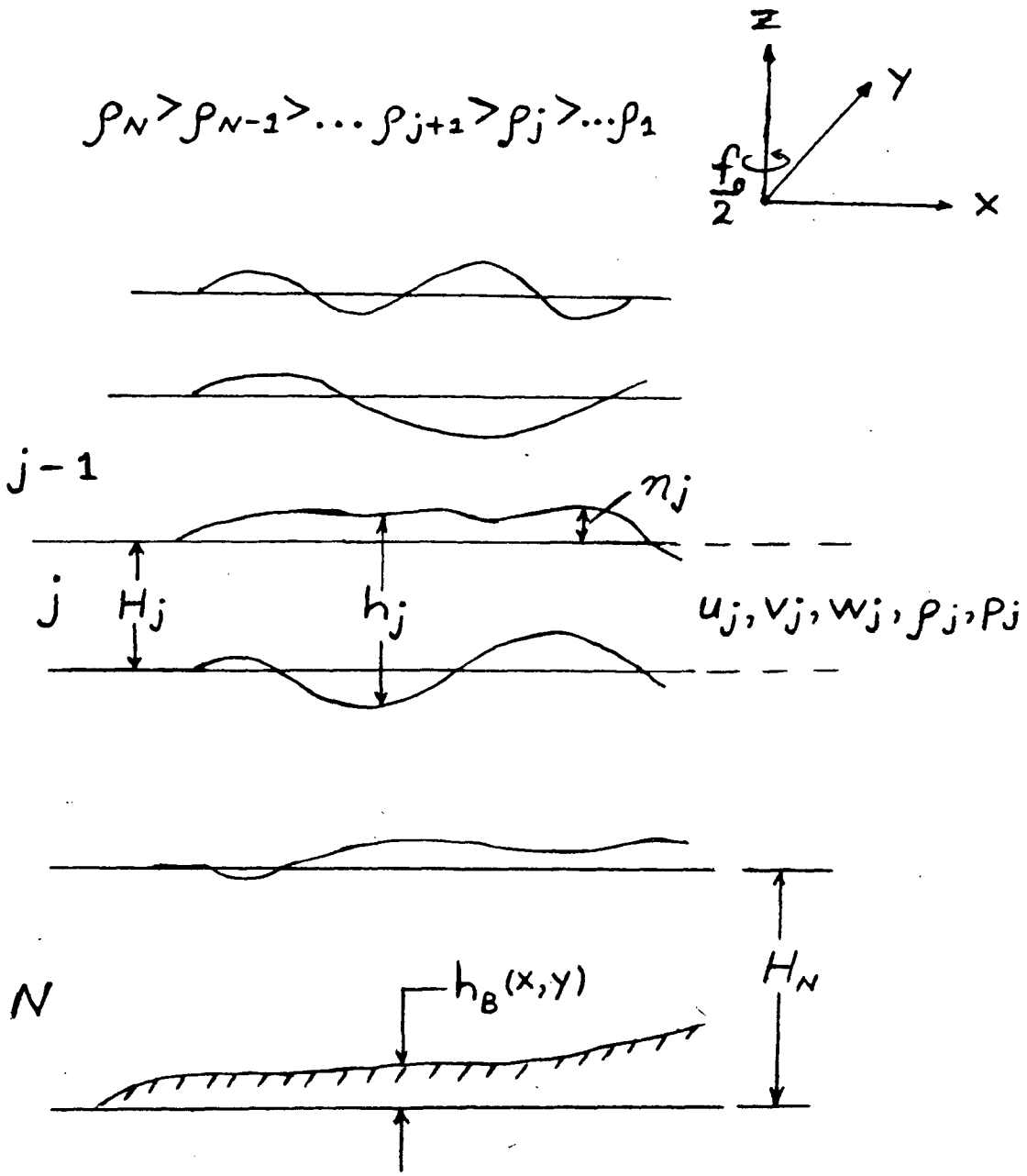

Fig.IV.8. The N-layer model.

Continuity of an incompressible nondiffusive fluid:

$$\frac{\partial u_j}{\partial x} + \frac{\partial v_j}{\partial y} = -\frac{1}{h_j}\frac{D}{Dt} h_j = \frac{1}{h_j}\frac{D}{Dt}(\eta_{j+1} - \eta_j) \qquad \text{(IV.64d)}$$

where, u_j , v_j are the x,y components of velocity (vertically averaged in the layer j,

p_j is the pressure in the layer j,

H_j is the thickness of the layer j in the absence of motion,

η_j is the displacement of the interface j,

h_j is the thickness of the layer j ($=H_j + \eta_j - \eta_{j+1}$),

τ_j^{Tx}, τ_j^{Ty} are the x,y components of the stress applied to the top of the layer j,

τ_j^{Bx}, τ_j^{By} are the x,y components of the stress applied to the bottom of the layer j,

ρ_j is the density of the layer j,

$$\frac{D}{Dt} \equiv \frac{\partial}{\partial t} + u_j\frac{\partial}{\partial x} + v_j\frac{\partial}{\partial y} \quad .$$

For convenience , I will subtract the static part of the pressure from the total pressure , i.e. the contribution $\sum_{j=1}^{n-1} g\rho_j H_j + g\rho_n(H_n - z)$ is subtracted from p_n . I will now specify the Boussinesq approximation ; that is , density differences between layers are assumed to be small so that the ρ_n's can be replaced by a reference density ρ_o except when density differences occur. The hydrostatic assumption (IV.64c) can then be written as

$$\eta_n = \frac{p_n - p_{n-1}}{g\left(\frac{\rho_n - \rho_{n-1}}{\rho_o}\right)} = \frac{p_n - p_{n-1}}{g_n'}$$

where

$$g_n' = g\left(\frac{\rho_n - \rho_{n-1}}{\rho_o}\right) .$$

If one also assumes $\eta_n / H_n << 1$, then one can eliminate the η_n's except where they occur in derivatives. That is, I will replace h_j by H_j in (IV.64a,b,c). Thus by eliminating the η_n's in the continuity equation

$$\frac{\partial u_j}{\partial x} + \frac{\partial v_j}{\partial y} = \frac{1}{H_j}\frac{D}{Dt}(\eta_{j+1} - \eta_j)$$

$$= \begin{cases} \frac{1}{H_j}\frac{D}{Dt}\left(\frac{p_{j+1} - p_j}{g_{j+1}'} - \frac{p_j - p_{j-1}}{g_j'}\right) & j = 1,2 \ldots N-1 \\ \frac{1}{H_N}\left[\vec{u}_N \cdot \nabla_H h_B - \frac{D}{Dt}\left(\frac{p_N - p_{N-1}}{g_N'}\right)\right] & j = N \end{cases}$$

[∇_H = horizontal gradient operator]

one can close the equations of motion. That is, there are 3N equations for the two velocities and the pressure in each of the N layers.

I will now introduce the assumption of quasi-geostrophy by following the scaling of Pedlosky (1979) . Velocity , length and stress scales (U,L, τ_0) are introduced as follows:

$$(x', y') = (x/L, y/L)$$

$$(u', v') = (u/U, v/U)$$

$$t' = t\,U/L$$

$$p_n' = p_n/\rho_0 f_0 U L$$

$$\tau_n'^{Tx}, \tau_n'^{Ty}, \text{etc.} = \frac{\tau_n^{Tx}}{\tau_0}, \frac{\tau_n^{Ty}}{\tau_0}, \text{etc.}$$

where the primed variables are non-dimensional. The horizontal momentum equations become (after dropping primes)

$$R_0 \frac{D}{Dt} u_j - v_j = -p_{jx} + \frac{\tau_0}{\rho_0 H_j U f_0} \left(\tau_j^{Tx} - \tau_j^{Bx}\right) \qquad \text{(IV.65a)}$$

$$R_0 \frac{D}{Dt} v_j + u_j = -p_{jy} + \frac{\tau_0}{\rho_0 H_j U f_0} \left(\tau_j^{Ty} - \tau_j^{By}\right) \qquad \text{(IV.65b)}$$

$$\left(R_0 \equiv \frac{U}{|f_0| L}\right) .$$

If I assume that the magnitude of the time variation and stress terms , characterized by R_o and $\tau_o/\rho_o H_j \bar{U} f_o$ respectively, are small, then I have geostrophic balance to a first approximation:

$$-v_j = -p_{jx} \quad ,$$

$$u_j = -p_{jy} \quad .$$

These equations are non-divergent horizontally ($u_{jx} + v_{jy} = 0$), and this has consequences when considering the non-dimensional continuity equation:

$$\frac{\partial u_j}{\partial x} + \frac{\partial v_j}{\partial y}$$

$$= \begin{cases} \frac{D}{Dt}\left[\frac{f_o \bar{U} L}{g'_{j+1} H_j}(p_{j+1} - p_j) - \frac{f_o \bar{U} L}{g'_j H_j}(p_j - p_{j-1})\right] & j = 1, 2, \ldots N-1 \\ \\ \frac{L}{H_N} \vec{u}_N \cdot \nabla h_B - \frac{D}{Dt} \frac{f_o \bar{U} L}{g'_N H_N}(p_N - p_{N-1}) & j = N \end{cases} \quad \text{(IV.65c)}$$

.

It is required that the terms on the right hand side are small, that is , of order R_o . Thus

$$\frac{f_o \bar{U} L}{g'_{j+1} H_j} \quad , \quad \frac{f_o \bar{U} L}{g'_{j+1} H_j} = O(R_o) \quad ,$$

$$\frac{L}{H_N} |\nabla h_B| = O(R_o) \, ,$$

which implies that

$$\frac{f_o^2 L^2}{g_{j+1}' H_j} = O(1) \quad ,$$

$$\frac{f_o L^2}{U H_N} |\nabla h_B| = O(1) \quad .$$

With the notations

$$\frac{f_o^2 L^2}{g_j' H_k} \equiv F_{jk} \quad ,$$

$$\frac{f_o L^2}{U H_N} |\nabla h_B| \equiv T \quad ,$$

I am demanding that the rotational Froude numbers (F_{jk}) and the topographic parameter (T) are of order unity. I will now formalize these considerations by introducing the following asymptotic expansions in the Rossby number R_o:

$$u_j = u_j^{(0)} + R_o u_j^{(1)} + \cdots \quad ,$$

$$v_j = v_j^{(0)} + R_o v_j^{(1)} + \cdots \quad ,$$

$$p_j = p_j^{(0)} + R_o p_j^{(1)} + \cdots \quad .$$

Thus , to lowest order I obtain

$$u_j^{(0)} = -\,\mathrm{sgn}(f_0)\, p_{jy}^{(0)} \quad ,$$

$$v_j^{(0)} = \mathrm{sgn}(f_0)\, p_{jx}^{(0)} \quad ,$$

(I have included the factor $\mathrm{sgn}(f_0)$ to allow for the possibility of working in the Southern Hemisphere), and to first order

$$\frac{D}{Dt} u_j^{(0)} - v_j^{(1)} = -p_{jx}^{(1)} + \frac{\tau_0}{R_0 \rho_0 H_j |f_0|} \left(\tau_j^{Tx} - \tau_j^{Bx} \right) \quad , \qquad \text{(IV.66a)}$$

$$\frac{D}{Dt} v_j^{(0)} + u_j^{(1)} = -p_{jy}^{(1)} + \frac{\tau_0}{R_0 \rho_0 H_j \tau |f_0|} \left(\tau_j^{Ty} - \tau_j^{By} \right) \quad , \qquad \text{(IV.66b)}$$

$$u_{jx}^{(1)} + v_{jy}^{(1)} =$$

$$\begin{cases} \dfrac{D}{Dt}\left[F_{j+1,j} \left(p_{j+1}^{(0)} - p_j^{(0)} \right) - F_{jj} \left(p_j^{(0)} - p_{j-1}^{(0)} \right) \right] & j = 1, 2, \ldots N-1 \\ \dfrac{D}{Dt}\left[\dfrac{T}{|\nabla h_B|} h_B - F_{NN} \left(p_N^{(0)} - p_{N-1}^{(0)} \right) \right] & j = N \end{cases} \qquad \text{(IV.66c)}$$

Note that the first order velocities and pressures in equation(IV.66a,b) can be eliminated by forming a vorticity equation $\left[\frac{\partial}{\partial x} \text{(IV.66b)} - \frac{\partial}{\partial y} \text{(IV.66a)} \right]$. Also noting that the lowest order pressures ($p_j^{(0)}$) are streamfunctions, I write

$$q_j = p_j^{(0)}$$

and thus find the vorticity equation to be given by

$$\left(\frac{\partial}{\partial t}+\mathrm{sgn}(f_0)\,\psi_{jx}\frac{\partial}{\partial y}-\mathrm{sgn}(f_0)\,\psi_{jy}\frac{\partial}{\partial x}\right)\Big\{\mathrm{sgn}(f_0)\,\Delta\psi_j + \mathrm{sgn}(f_0)\left[F_{j+1,j}(\psi_{j+1}-\psi_j)-F_{jj}(\psi_j-\psi_{j-1})\right]\Big\} = \frac{\tau_0}{R_0|f_0|\tau\rho_0 H_j}\,\mathrm{curl}_z\left(\tau_j^T-\tau_j^B\right) \qquad j=1,2,\ldots N-1 \tag{IV.67a}$$

$$\left(\frac{\partial}{\partial t}+\mathrm{sgn}(f_0)\,\psi_{jx}\frac{\partial}{\partial y}-\mathrm{sgn}(f_0)\,\psi_{jy}\right)\Big\{\mathrm{sgn}(f_0)\,\Delta\psi_j + \frac{+T}{|\nabla h_B|}\,h_B - \mathrm{sgn}(f_0)\,F_{NN}(\psi_N-\psi_{N-1})\Big\} = \frac{\tau_0}{R_0|f_0|\tau\rho_0 H_j}\,\mathrm{curl}_z\left(\tau_N^T-\tau_N^B\right) \qquad j=N \tag{IV.67b}$$

where $\Delta=\frac{\partial}{\partial x^2}+\frac{\partial}{\partial y^2}$. It is interesting to note that the left hand sides of IV.67a,b are not invariant under a change of sign of f_0.

I now wish to linearize equations(IV.67) . That is, I will assume small perturbations about a basic state and retain only terms of first order in the perturbations in the equations of motion. The basic state will be assumed to be one of steady motion in the positive y direction; the velocities may vary from layer to layer. These motions are assumed to be in geostrophic balance so that (remembering that ψ_j is a geostrophic pressure)

$$\psi_j=\bar{\psi}+\psi_j'=\mathrm{sgn}(f_0)\,\bar{V}_{jx}+\psi_j'$$

where $\bar{\psi}_j$ is the mean pressure and ψ_j' is the perturbation pressure (V_j is the mean velocity in the layer j). Thus,

equation(IV.67) becomes (after dropping primes)

$$\left(\frac{\partial}{\partial t}+\bar{V}_j\frac{\partial}{\partial y}\right)\left[\Delta\psi_j+F_{j+1,j}(\psi_{j+1}-\psi_j)-F_{jj}(\psi_j-\psi_{j-1})\right]$$
$$-\left[F_{j+1,j}(\bar{V}_{j+1}-\bar{V}_j)-F_{jj}(\bar{V}_j-\bar{V}_{j-1})\right]\psi_{jy} \qquad \text{(IV.68a)}$$
$$=\frac{\tau_0}{R_0 f_0 \bar{U}\rho_0 H_j}\,curl_z(\tau_j^T-\tau_j^B) \qquad j=1,2,\ldots N-1$$

$$\left(\frac{\partial}{\partial t}+\bar{V}_N\frac{\partial}{\partial y}\right)\left[\Delta\psi_N-F_{NN}(\psi_N-\psi_{N-1})\right] \qquad \text{(IV.68b)}$$
$$+\left[F_{NN}(\bar{V}_N-\bar{V}_{N-1})-sgn(f_0)\,sgn\left(\frac{\partial h_B}{\partial x}\right)\tau\right]\psi_{Ny}$$
$$=\frac{\tau_0}{R_0 f_0 \bar{U}\rho_0 H_j}\,curl_z(\tau_N^T-\tau_N^B) \qquad j=N$$

where I have now assumed $h_B=h_B(x)$. The left hand side of IV.68a is invariant under a change of sign of f_0 while the right hand sides of (IV.68a,b) change sign when f_0 does. The left hand side of IV.68b is invariant under a change of sign of f_0 only if $\partial h_B/\partial x$ also changes sign.

The stresses appearing in equation(IV.68) are of three types: (i.) The stress τ_1^T is the wind stress acting on the ocean. It may be calculated from the formula $\tau_1^T=\tau_{WIND}=\rho_{AIR}C_D\bar{U}_{WIND}^2$ (C_D is a drag coefficient). (ii.) The interfacial stresses $\tau_1^B,\tau_2^T,\ldots\tau_N^T$, which represent the turbulent momentum exchange between layers moving at different velocities. (iii.) The bottom stress τ_B^N which represents the drag induced by the fluid moving over a solid boundary. The usual formulation for bottom friction is in terms of Ekman layer dynamics (Pond and Pickard, 1978). One supposes that the

(dimensional) frictional stress given by

$$\tau_{FRIC} = \rho_0 A_z \frac{\partial \vec{u}}{\partial z}$$

(A_z is the coefficient of eddy viscosity) is largely confined to an Ekman layer. If one uses the e-folding distance $\delta_E = \sqrt{\frac{2A_z}{f}}$ of the Ekman layer, then one can approximate the bottom stress by

$$\vec{\tau}_N^B = \rho A_z \frac{\vec{u}_N}{\delta_E} = \frac{\rho A_z}{\sqrt{\frac{2A_z}{f}}} u_N \ .$$

A similar approach can be used to estimate the interfacial stresses, but the stresses are not confined to an Ekman layer, at least not in the continuous case I am trying to represent. Presumably, the scale depth for the stress should be no greater than the total layer thickness. Thus I write the interfacial stress in the form of an inequality

$$\begin{aligned} \frac{\rho A_z}{H_j} \ (\vec{u}_j - \vec{u}_{j+1}) \\ < \vec{\tau}_j^B = \vec{\tau}_{j+1}^T \\ < \rho \frac{A_z}{\delta_E} (\vec{u}_j - \vec{u}_{j+1}) \quad j = 1, 2, \ldots N-1 \end{aligned} \tag{IV.69}$$

where I have invoked continuity of stress at an interface to write $\vec{\tau}_j^B = \vec{\tau}_{j+1}^T$. An alternative formulation for the interfacial stresses is given by O'Brien and Hurlburt (1972). They invoke the familiar quadratic stress law:

$$\vec{\tau}_j^B = \vec{\tau}_{j+1}^T = \rho C_1^* \bar{u} (u_j - u_{j+1}) \tag{IV.70}$$

where C_I^* is a dimensionless interfacial drag coefficient and $\bar{u}$ is the modulus of the mean speeds represented by $\vec{u}_j$ and $\vec{u}_{j+1}$. To linearize this stress law, I will assume $\bar{u}$ to be constant. Quoted values for C_I^* range from 3×10^{-4} (O'Brien and Hurlburt, 1972) to 10^{-5} (McNider and O'Brien, 1973). I have found values of A_z (for equatorial thermoclines) ranging from 1 cm^2/s (Robinson, 1966 ; Jones, 1973) to 10 cm^2/s (Philander, 1973). Using these values in (IV.69), one can find the extremes possible for the stress using an eddy viscosity coefficient:

$$10^{-4}\,cm/s\,(\vec{u}_j - \vec{u}_{j-1}) < \frac{\vec{\tau}_j^B}{\rho} = \frac{\vec{\tau}_{j+1}^T}{\rho} < 7\times10^{-3}\,cm/s\,(\vec{u}_j - \vec{u}_{j+1}) \qquad j = 1, 2, \ldots N-1$$

where I have assumed $f \approx 10^{-5}\ s^{-1}$, $H \approx 100m$. This range is approximately matched if one chooses $\bar{u}$ in (IV.70) to be about 10cm/s which is a reasonable scale for the fluctuations I wish to model. I will thus explore the range

$$10^{-4}\,cm/s < C_I < 3\times10^{-3}\,cm/s$$

where $C_I = C_I^*\bar{u}$ and $\vec{\tau}_j^B = \vec{\tau}_{j+1}^T = \rho C_I(\vec{u}_j - \vec{u}_{j+1})$. For the bottom friction ($\vec{\tau}_N^B$) I will choose the largest value in the range:

$$C_B = 3\times10^{-3}\,cm/s \quad \text{where} \quad \vec{\tau}_N^B = \rho C_B \vec{u}_N .$$

With these considerations, I may now write (IV.68) as

$$\left(\frac{\partial}{\partial t}+\bar{V}_1\frac{\partial}{\partial y}\right)\left[\Delta 4_1+F_{21}(4_2-4_1)-F_{11}(4_1-4_0)\right]-\left[F_{21}(\bar{V}_2-\bar{V}_1)-F_{11}\bar{V}_1\right]4_{1y} \qquad \text{(IV.71a)}$$

$$+\frac{c_I}{R_0|f_0|H_1}\Delta(4_1-4_2)=\frac{\tau_0}{R_0 f_0 \bar{\rho}_0 H_1}\,curl_z\,\tau_{WIND} \qquad j=1$$

$$\left(\frac{\partial}{\partial t}+\bar{V}_j\frac{\partial}{\partial y}\right)\left[\Delta 4_j+F_{j+1,j}(4_{j+1}-4_j)-F_{jj}(4_j-4_{j-1})\right] \qquad \text{(IV.71b)}$$

$$-\left[F_{j+1,j}(\bar{V}_{j+1}-\bar{V}_j)-F_{jj}(\bar{V}_j-\bar{V}_{j-1})\right]4_{jy}-\frac{c_I}{R_0|f_0|H_j}\Delta(4_{j+1}-4_j)$$

$$+\frac{c_I}{R_0|f_0|H_j}\Delta(4_j-4_{j-1})=0 \qquad j=2,\ldots,N-1$$

$$\left(\frac{\partial}{\partial t}+\bar{V}_N\frac{\partial}{\partial y}\right)\left[\Delta 4_N-F_{NN}(4_N-4_{N-1})\right]+\left[F_{NN}(\bar{V}_N-\bar{V}_{N-1})\right. \qquad \text{(IV.71c)}$$

$$\left.-\mathrm{sgn}(f_0)\,\mathrm{sgn}\left(\frac{\partial h_B}{\partial x}\right)T\right]4_{Ny}+\frac{c_I}{R_0|f_0|H_N}\Delta(4_N-4_{N-1})+\frac{c_B}{R_0|f_0|H_N}\Delta 4_N=0$$

$$j=N\,.$$

I will now discuss the suppression of the β-effect in the preceeding considerations. In the modelling to follow I am interested in two things: (i.) the amplitudes of the responses in the various layers and (ii.) the longshore wavelength of the oceanic response . It will be seen that the upper-layer response is determined principally by the value of the friction parameter; the response in the lower layers depends on the coupling to the upper layer (via the rotational Froude numbers and friction parameters) . The following simple argument assesses the role of β in interlayer coupling: For geostrophic balance with variable f,

$$-\beta y v_1=-p_{1x}/\rho\,,$$

$$\beta y u_1=-p_{1y}/\rho\,.$$

The divergence no longer vanishes to lowest order since

$$\beta v_1+\beta y v_{1y}=-p_{1xy}/\rho,$$

$$-\beta y u_{1x}=-p_{1xy}/\rho$$

implying that

$$\beta y (u_{1x} + v_{1y}) = \beta v_1$$

thus

$$\beta y^2 (u_{1x} + v_{1y}) = \beta y v_1 = -p_{1x} \quad .$$

From the continuity equation

$$u_{1x} + v_{1y} = \frac{1}{g'H} (p_{2t} - p_{1t})$$

I find

$$p_{1x} = -\frac{\beta y^2}{g'H} (p_{2t} - p_{1t}) \quad .$$

I now have an interlayer coupling term (analogous to the rotational Froude number) given by $\frac{\beta y^2}{g'H}$. Thus the "β-coupling" will be important if the term $\frac{\beta y^2}{g'H}$ is comparable to the dimensional coupling paramter $\frac{fL}{g'H}$, that is

$$\frac{\beta y^2}{g'H} \approx \frac{fL}{g'H} \rightarrow \beta y^2 \simeq fL$$

In fact I am interested in latitudes of about 2°S, so that with L=100km (the Somali Current width), I have

$$\beta y^2 \approx 0.8 \text{ m/s} \qquad \text{whereas} \qquad fL \approx 1 \text{ m/s}$$

Thus the β-coupling effect is comparable to the dimensional coupling parameter. However, parameter sensitivity studies of the model to be presented indicate that model properties only vary weakly with the coupling parameter. The frictional terms turn out to be much more important in interlayer coupling.

I will now address point (ii.) above: The wavelength is determined by the dispersion relation which, including the β effect (but ignoring the rotational Froude number terms which I will show to be small) is given by

$$(-\omega + k\bar{U})(k^2 + m^2\pi^2) + k\beta = 0$$

For the situation of interest one finds $k^2 << \pi^2$ so that

$$k \approx \frac{\omega}{\bar{U} + \frac{\beta}{\pi^2}} \qquad \text{with} \qquad \beta = \frac{\beta_{DIMENSIONAL}}{f/L} \approx 2.$$

Thus $k \approx \frac{\omega}{\bar{U}+0.2}$, where U is of order unity. It seems that the β effect will not make a significant difference to the longshore wavenumber calculation. An important consequence of the variations in the coriolis parameter is the leakage of shear wave energy into the equatorial waveguide (as the decrease of f reduces the interfacial slopes and thus the restoring force for shear waves). This leakage is significant as the shear waves pass through the equatorial waveguide (which extends 2° to 3° on either side of the equator). Since the region of interest is at about 2.5°S the waves are still on the border of the equatorial waveguide and should not have leaked significant energy at this latitude.

To represent the situation of interest, that is, the Somali Current near station K2, I now choose a 3-layer model, in order that the three current meters at K2 be represented. To simplify the calculations I will assume the flow to be confined to a channel, as illustrated in Fig. IV.9. The use of channel

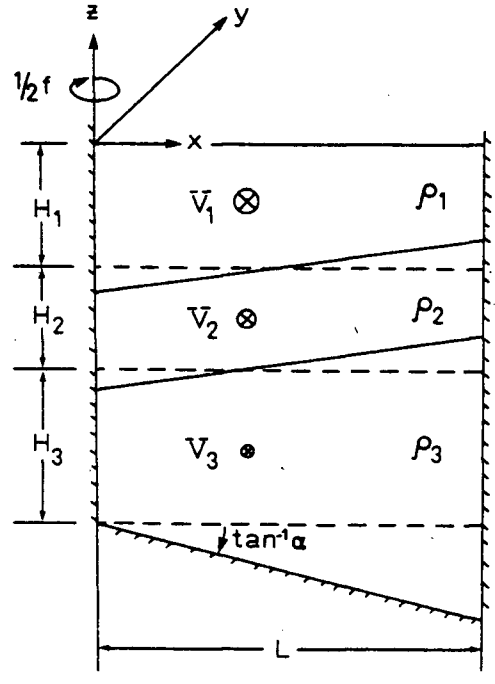

Fig.IV.9. Model of the channel flow considered in the response analysis. V_1, V_2, V_3, are assumed constant. The interfacial slopes are drawn appropriate to a Southern Hemisphere situation with the mean velocity decreasing monotonically with depth.

models in instability calculations has been justified by Mysak, Johnson , and Hsieh (1981). They showed that baroclinic shear modes (with which I shall be primarily concerned) decay away from the coast in an f-plane model. Physically, this is reasonable in that the restoring forces for the wave modes (current shears) exist only in the narrow shear zones near the coast; to a first approximation the waves are confined to the region where restoring forces exist, and wave energy found in the ocean's interior is due to leakage from the current zone. Thus, I consider the presence of an outer rigid wall to be reasonable, certainly at 3-4°S.

The equations of motion are:

$$\left(\frac{\partial}{\partial t}+\bar{V}_1\frac{\partial}{\partial y}\right)\left[\Delta\psi_1+F_{21}(\psi_2-\psi_1)\right]+F_{21}(\bar{V}_1-\bar{V}_2)\psi_{1y}$$

$$+R_{12}\Delta(\psi_1-\psi_2)=\frac{-\tau_0}{R_0 f_0 \bar{V}\rho_1 H_1}\,\mathrm{curl}_z\,\tilde{\tau}_{WIND}\,, \tag{IV.72a}$$

$$\left(\frac{\partial}{\partial t}+\bar{V}_2\frac{\partial}{\partial y}\right)\left[\Delta\psi_2+F_{32}(\psi_3-\psi_2)-F_{22}(\psi_2-\psi_1)\right]$$

$$+\left[F_{32}(\bar{V}_2-\bar{V}_3)-F_{22}(\bar{V}_1-\bar{V}_2)\right]\psi_{2y}-R_{23}\Delta(\psi_3-\psi_2) \tag{IV.72b}$$

$$+R_{21}\Delta(\psi_2-\psi_1)=0,$$

$$\left(\frac{\partial}{\partial t}+\bar{V}_3\frac{\partial}{\partial y}\right)\left[\Delta\psi_3-F_{33}(\psi_3-\psi_2)\right] \tag{IV.72c}$$

$$-\left[F_{33}(\bar{V}_2-\bar{V}_3)+T\right]\psi_{3y}+R_{32}\Delta(\psi_3-\psi_2)+R_b\Delta\psi_3=0\,,$$

where

$$\Delta = \partial_{xx} - \partial_{yy},$$

V_j is the mean velocity in layer j (j=1,2,3)

$$F_{ij} = \frac{f_o^2 L^2}{g_i' H_j}$$ (internal rotational Froude numbers for each layer)

$$g_2' = g(\rho_2 - \rho_1)/\rho_2, \quad g_3' = (\rho_3 - \rho_2)/\rho_3,$$

$$T = \frac{\alpha |f_o| L^2}{H_3 \bar{U}}$$ (topographic parameter)

$$R_{ij} = \frac{C_I}{R_o |f_o| H_i}$$ (interfacial friction parameters)

$$R_b = \frac{C_B}{R_o |f_o| H_3}$$ (bottom friction parameter) .

In the above , R_o (the Rossby number) $=(U/|f_o|L)$, α is the bottom slope , and C_I and C_B are interfacial and bottom friction coefficients respectively. For the channel model , the boundary conditions are

$$\psi_n = 0 \quad at \quad x=0,1 \quad (n=1,2,3). \qquad (IV.73)$$

I will now solve the equations for quite general forcing functions; I will require only that the solution be periodic in time. The solution will be expressed as a sum of along-channel propagating waves. To this end , it is convenient to Fourier transform equations (IV.72) in the along- channel coordinate (y):

$$(-\omega_o + k\bar{v}_1)[(\partial_{xx}-k^2)\tilde{\psi}_1(x,k) + F_{21}(\tilde{\psi}_2(x,k)-\tilde{\psi}_1(x,k))] \qquad \text{(IV.74a)}$$
$$+ k F_{21}(\bar{v}_1-\bar{v}_2)\tilde{\psi}_1(x,k)$$
$$- i R_{12}(\partial_{xx}-k^2)[\tilde{\psi}_1(x,k)-\tilde{\psi}_2(x,k)] = \tilde{F}(x,k) ,$$

$$(-\omega_o + k\bar{v}_2)[(\partial_{xx}-k^2)\tilde{\psi}_2(x,k) + F_{32}(\tilde{\psi}_3(x,k)-\tilde{\psi}_2(x,k)) - F_{22}(\tilde{\psi}_2(x,k)-\tilde{\psi}_1(x,k))]$$
$$+ k[F_{32}(\bar{v}_2-\bar{v}_3) - F_{22}(\bar{v}_1-\bar{v}_2)]\tilde{\psi}_2(x,k) \qquad \text{(IV.74b)}$$
$$+ i R_{23}(\partial_{xx}-k^2)[\tilde{\psi}_3(x,k)-\tilde{\psi}_2(x,k)] - i R_{21}(\partial_{xx}-k^2)[\tilde{\psi}_2(x,k)-\tilde{\psi}_1(x,k)]$$
$$= 0 ,$$

$$(-\omega_o + k\bar{v}_3)[(\partial_{xx}-k^2)\tilde{\psi}_3(x,k) - F_{33}(\tilde{\psi}_3(x,k)-\tilde{\psi}_2(x,k))$$
$$- k[F_{33}(\bar{v}_2-\bar{v}_3)+T]\tilde{\psi}_3(x,k) \qquad \text{(IV.74c)}$$
$$- i R_{32}(\partial_{xx}-k^2)[\tilde{\psi}_3(x,k)-\tilde{\psi}_2(x,k)] - i R_b(\partial_{xx}-k^2)\tilde{\psi}_3(x,k) = 0 ,$$

where I have assumed oscillatory forcing functions and responses, i.e.

$$\frac{i\tau_o}{R_o f_o \bar{\rho}_1 H_1}\, curl_z \tilde{\tau}_{WIND} \equiv F(x,y,t) = F(x,y)e^{-i\omega_o t} ,$$

$$\psi_j(x,y,t) = \psi_j(x,y)e^{-i\omega_o t} ,$$

and

$$\tilde{\psi}(x,k) = \int_{-\infty}^{\infty} \psi(x,y)e^{iky}\,dy ,$$

$$\tilde{F}(x,k) = \int_{-\infty}^{\infty} F(x,y)e^{-iky}\,dy .$$

The solutions to the homogeneous version of equations (IV.74)

are:

$$\tilde{\psi}_j(x,k) = \tilde{\psi}_{j,m}(k) \sin m\pi x$$

$$m = 1,2,\ldots \quad ; \quad j = 1,2,3.$$

Since the cross channel eigenfunctions $\sin(m\pi x)$ are orthogonal, the forcing function can be expanded in terms of them, viz.,

$$\tilde{F}(x,k) = \sum_{m=1}^{\infty} \tilde{f}_m(k) \sin m\pi x$$

where

$$\tilde{f}_m(k) = 2\int_0^1 \tilde{F}(x,k) \sin m\pi x \, dx \ .$$

Thus , the inhomogeneous equations may be written as follows:

$$(-\omega_o + k\bar{V}_1)[-k^2\tilde{\psi}_{1,m}(k) + F_{21}(\tilde{\psi}_{2,m}(k) - \psi_{1,m}(k))]$$
$$+ kF_{21}(\bar{V}_2 - \bar{V}_1)\tilde{\psi}_{1,m}(k) + iR_{12}k^2[\tilde{\psi}_{1,m}(k) - \tilde{\psi}_{2,m}(k)]$$
$$= \tilde{f}_m(k) \ , \qquad \text{(IV.75a)}$$

$$(-\omega_o + k\bar{V}_2)[-k^2\tilde{\psi}_{2,m}(k) + F_{32}(\tilde{\psi}_{3,m}(k) - \tilde{\psi}_{2,m}(k))$$
$$- F_{22}(\tilde{\psi}_{2,m}(k) - \tilde{\psi}_{1,m}(k))] + k(F_{32}(\bar{V}_2 - \bar{V}_3) - F_{22}(\bar{V}_1 - \bar{V}_2))\tilde{\psi}_{2,m}(k) \qquad \text{(IV.75b)}$$
$$- iR_{23}k^2[\tilde{\psi}_{3,m}(k) - \tilde{\psi}_{2,m}(k)] + iR_{21}k^2[\tilde{\psi}_{2,m}(k) - \tilde{\psi}_{1,m}(k)]$$
$$= 0 \ ,$$

$$(-\omega_o + k\bar{V}_3)[-k^2\tilde{\psi}_{3,m}(k) - F_{33}(\tilde{\psi}_{3,m}(k) - \tilde{\psi}_{2,m}(k))] \qquad \text{(IV.75c)}$$
$$- k[F_{33}(\bar{V}_2 - \bar{V}_3) + T]\tilde{\psi}_{3,m}(k) + iR_{32}k^2[\tilde{\psi}_{3,m}(k) - \tilde{\psi}_{2,m}(k)]$$
$$+ iR_b k^2 \tilde{\psi}_{3,m} = 0 \ ,$$

where $K^2=k^2+m^2\pi^2$.

If these equations are written in matrix form , i.e.,

$$A_{ij}\begin{pmatrix}\tilde{4}_{1,m}(k)\\ \tilde{4}_{2,m}(k)\\ \tilde{4}_{3,m}(k)\end{pmatrix}=\begin{pmatrix}\tilde{f}_m(k)\\ 0\\ 0\end{pmatrix}$$

where

$$A_{ij}=\begin{pmatrix}a_{11} & a_{12} & 0\\ a_{21} & a_{22} & a_{23}\\ 0 & a_{32} & a_{33}\end{pmatrix}$$

(the coefficients a_{ij} are given in Appendix II), then one finds the solutions

$$\tilde{4}_{1,m}(k)=\left(\frac{1}{a_{11}}+\frac{a_{33}a_{21}a_{12}}{a_{11}}\frac{1}{\det(A_{ij})}\right)\tilde{f}_m(k)\equiv T_{1,m}(k)\,\tilde{f}_m(k) \qquad \text{(IV.76a)}$$

$$\tilde{4}_{2,m}(k)=\frac{-a_{33}a_{21}}{\det(A_{ij})}\tilde{f}_m(k)\equiv T_{2,m}(k)\,\tilde{f}_m(k) \qquad \text{(IV.76b)}$$

$$\tilde{4}_{3,m}(k)=\frac{a_{32}a_{21}}{\det(A_{ij})}\tilde{f}_m(k)\equiv T_{3,m}(k)\,\tilde{f}_m(k) \qquad \text{(IV.76c)}$$

where $\det(A_{ij})$ is the determinant of the matrix A_{ij} and $T_{j,m}(k)$ are the transfer functions for the the layer j. one can now write the solution as

$$\psi_j(x,y,t) = e^{-i\omega_0 t} \sum_{m=1}^{\infty} \frac{1}{2\pi} \int_{-\infty}^{\infty} T_{j,m}(k)\, \tilde{f}_m(k)\, e^{iky}\, dk \sin m\pi x \qquad \text{(IV.77)}$$

Application to the Somali Current

To apply the model developed , the available data must be used to calculate the model parameters . For example, one must specify:

(i.) The bottom slope (to calculate the topographic parameter T).

(ii.) The density stratification (to calculate the appropiate layer depths and then the rotational Froude numbers).

(iii.) The mean current in each layer.

I am primarily concerned with applying the model near K2 ,since I have more detailed information from this station. As seen in Chapter III , the mean current field and bathymetry near K2 are quite complicated , making it rather challenging to fit a three-

layer model to this regime. Specifically, the concept of a bottom layer is somewhat contrived in that topography and bottom flow change greatly in going from the continental shelf to the contintal slope. However , in most of the considerations to follow, it will be seen that the upper-layer shear mode dominates the amplitude response of the system. This makes accurate representation of the bottom regime less important, and stresses the importance of fitting the channel to the near-surface flow. Accordingly, I will adopt the "scale" width of 100km for the Somali Current , given by Düing and Schott (1978) , as the channel width "L". The question is then where to position the center of the channel relative to station K2. Because of the importance of the current field for the model one should now examine Figure IV.10. It is seen that the surface currents south of Chisimaio attain their maximum value (with respect to transverse extent) near K2. It then seems reasonable to position the center of the channel near K2 . With these general considerations in mind, I can now proceed to fit the parameters of the channel model.

Parameter Fitting

The choice of layer depths will be based on the stratification. The only direct information I have on the stratification is that obtained from the mean temperature curves (dashed lines in Fig.IV.11a,b,c) constructed from the temperature data supplied by the K2 sensors. The three sensors

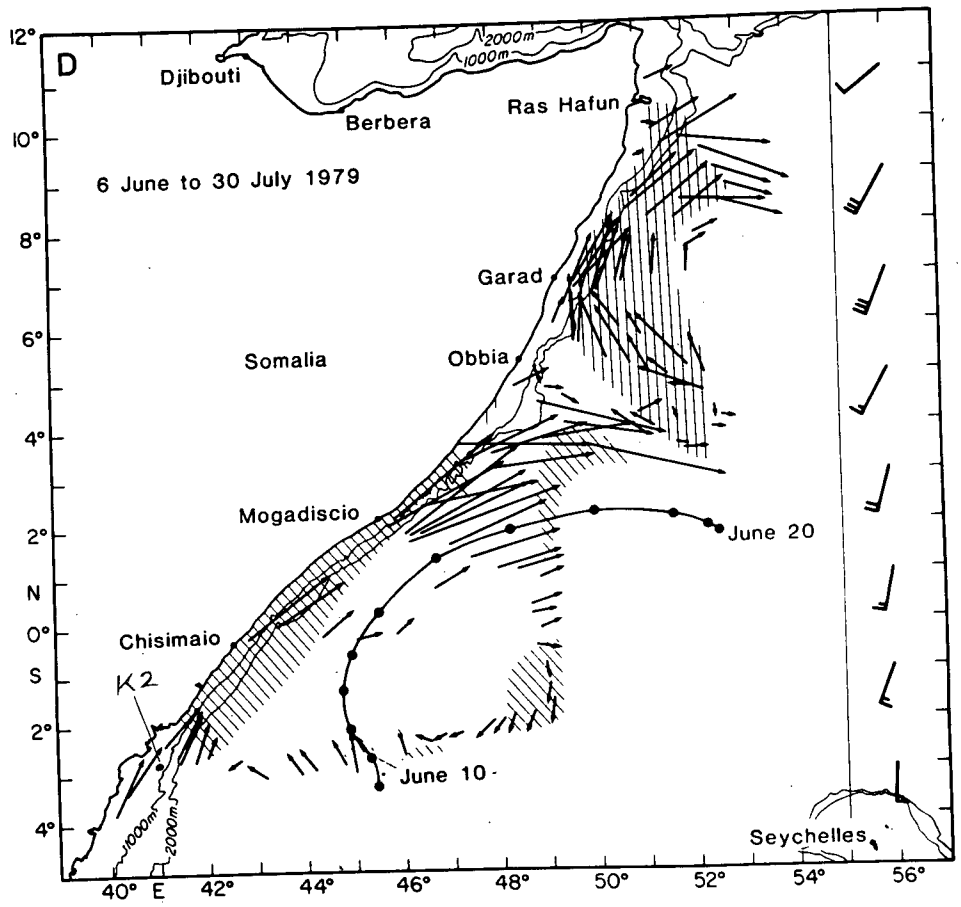

Fig.IV.10. Surface current data collected during INDEX (1979). Current arrows are centered on the observation point. (From Düing, Molinari, and Swallow ,1980).

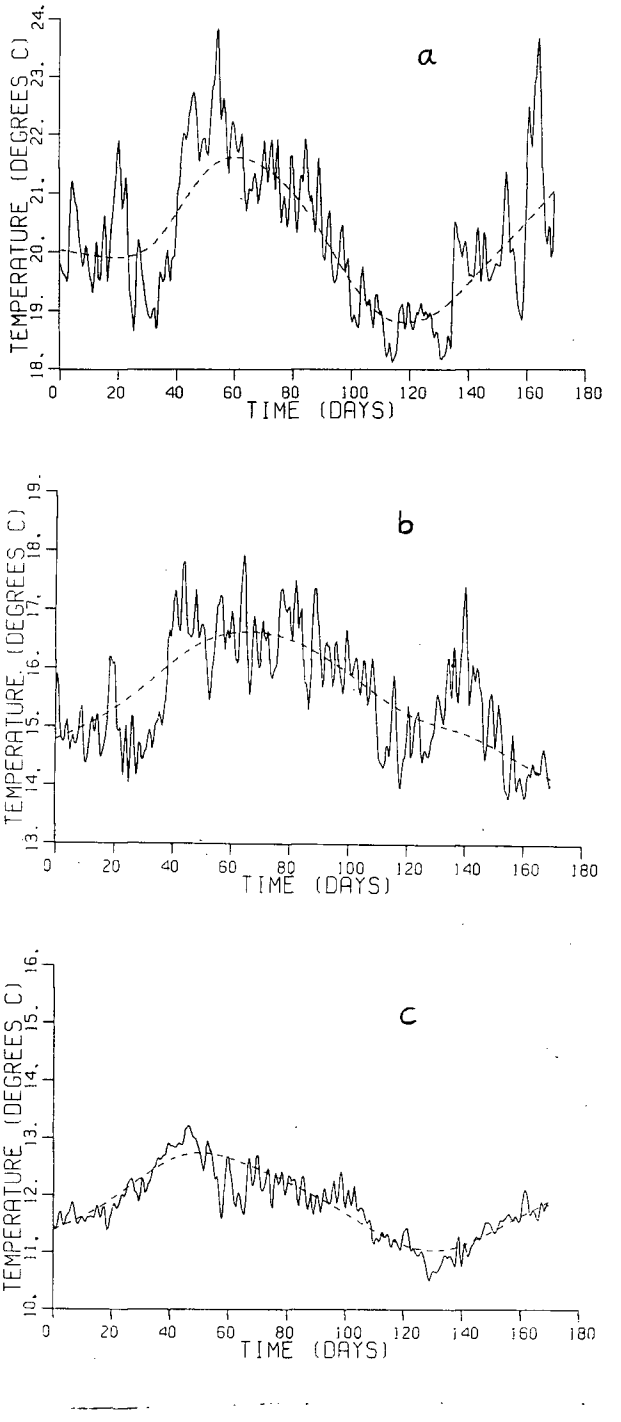

Fig.IV.11. (a) The temperature record from the top sensor of station K2. The dashed line represents a spline-fit to the mean temperature.
(b) As in (a), except for the middle sensor. Note that the ordinate has been shifted by 5°C.
(c) As in (a), except for the bottom sensor. Note that the ordinate has been shifted by 8°C.

provide little vertical resolution . A better temperature profile was obtained at station M1 (see Fig.III.10) which is about 50 km north of K2. This profile is shown in Fig.IV.12. From it the depth of the mixed layer is estimated to be about 75m , and this allows one to draw a rough mean temperature profile for K2 as illustrated in Fig.IV.13. These plotted values of temperature are intermediate between the maximum and minimum extremes seen in the K2 temperature records (this profile represents the situation in late April). Also shown in this figure is a temperature profile taken from Cox (1976) which is intended to represent the mean Indian Ocean conditions. The correspondence is reasonable except that Cox apparently has a somewhat shallower mixed layer. This correspondence encourages one to assume that Cox's density and temperature profiles (Fig. IV.14) are reasonably applicable to the situation of interest. If Cox's density data is plotted versus temperature (Fig. IV.15) , I find a reasonably linear relationship, suggesting that I can use the relation $\sigma_t = \sigma_o (1 - \alpha' T)$ (where $\sigma_o \cong 30.3$, $\alpha' \cong 9.2 \times 10^{-3} {}^\circ C^{-1}$) to infer densities from the temperature profiles.

In a layer model, the interfaces should represent rapid changes in the properties of the actual (continuous) fluid. This suggests putting the first interface at the middle of the observed pycnocline. The preceeding considerations suggest that the pycnocline and the thermocline coincide, so that Fig.IV.13 indicates placement of the first layer deep enough to include the top current meter of the first interface at about 130m, (I

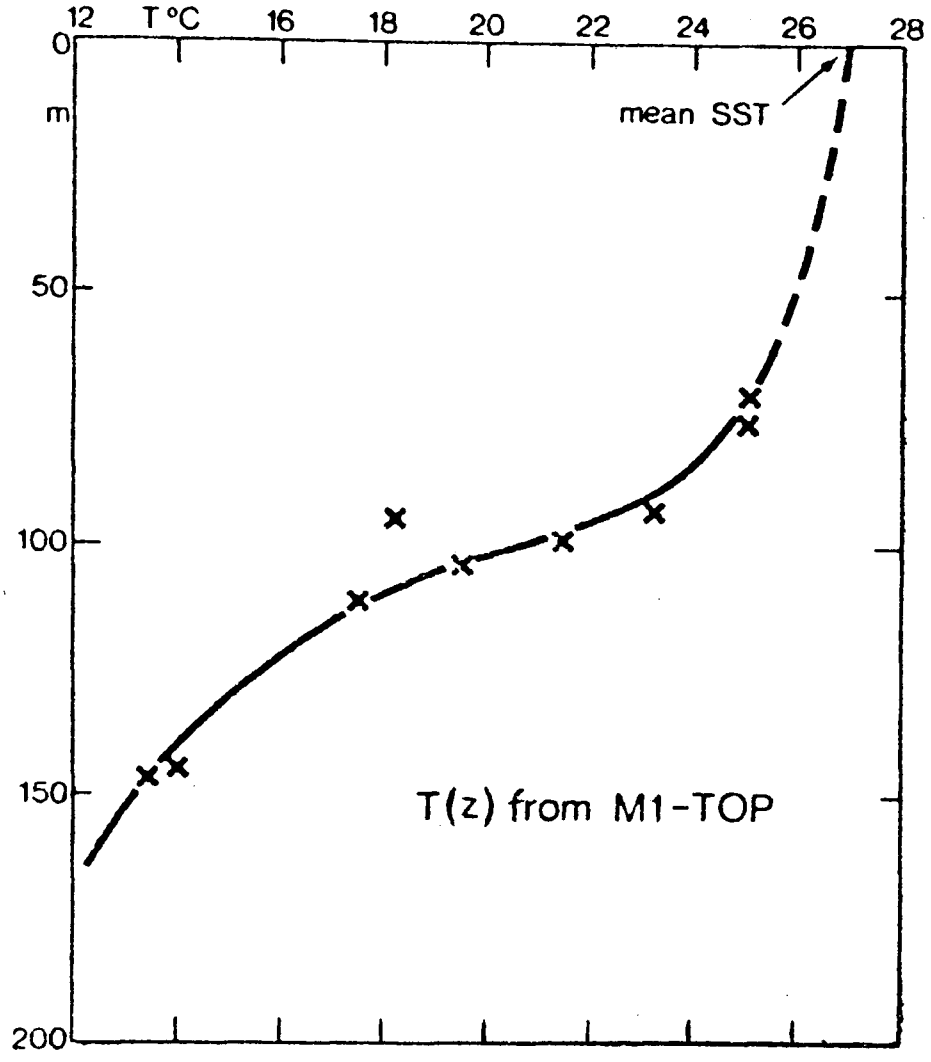

Fig.IV.12. Reconstruction of vertical temperature distribution by using simultaneous temperature and pressure records from the top sensor at mooring M1. (From Düing and Schott ,1978).

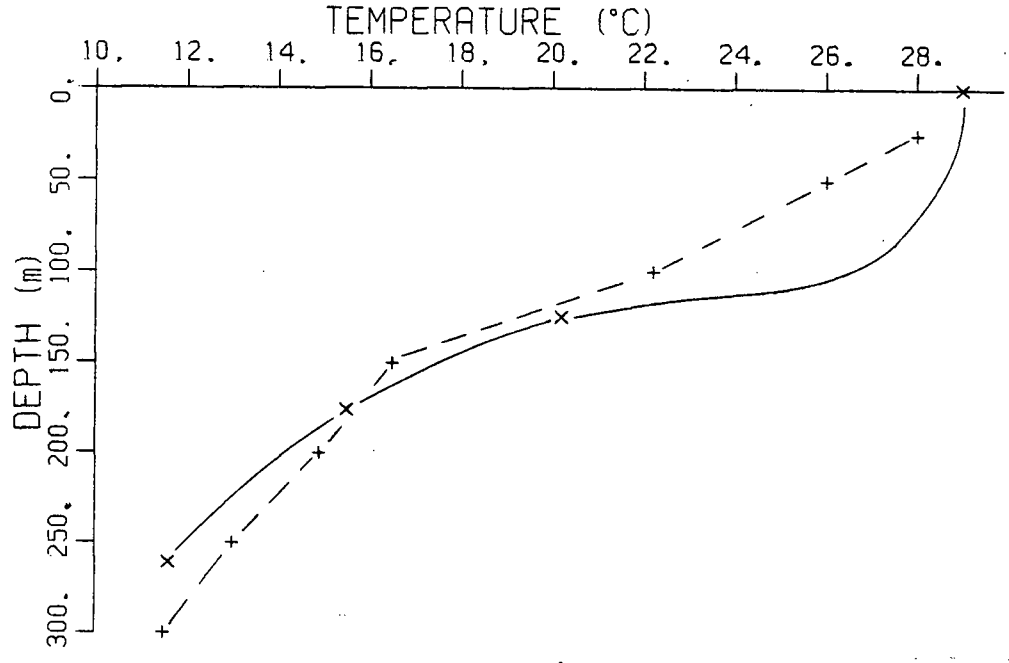

Fig.IV.13. Temperature profiles: the dashed curve is from Cox (1976) and represents mean Indian Ocean conditions; the solid curve is from K2 data and represents local conditions in late April. The surface point on the K2 curve is estimated from data in Brown, Bruce, and Evans (1980).

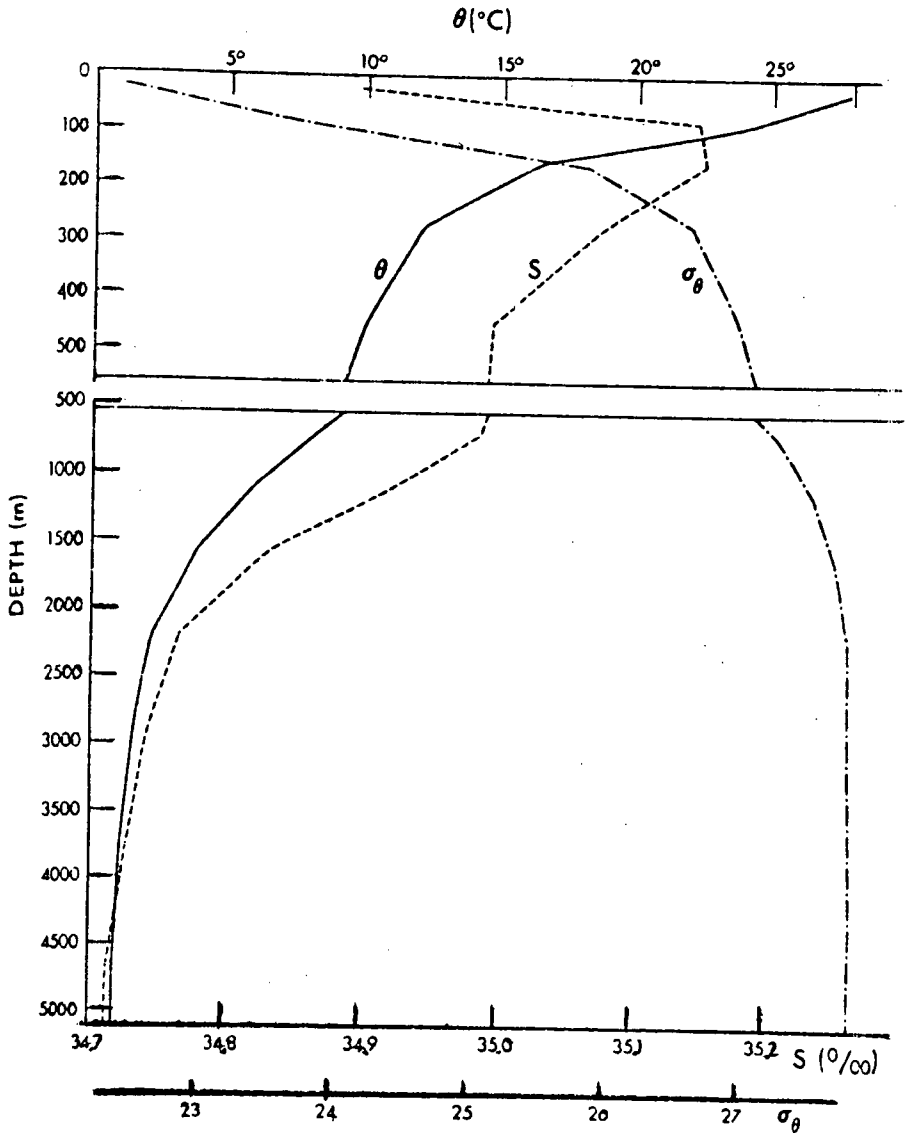

Fig.IV.14. Potential temperature (θ) and density (σ_θ) profiles from Cox (1976).

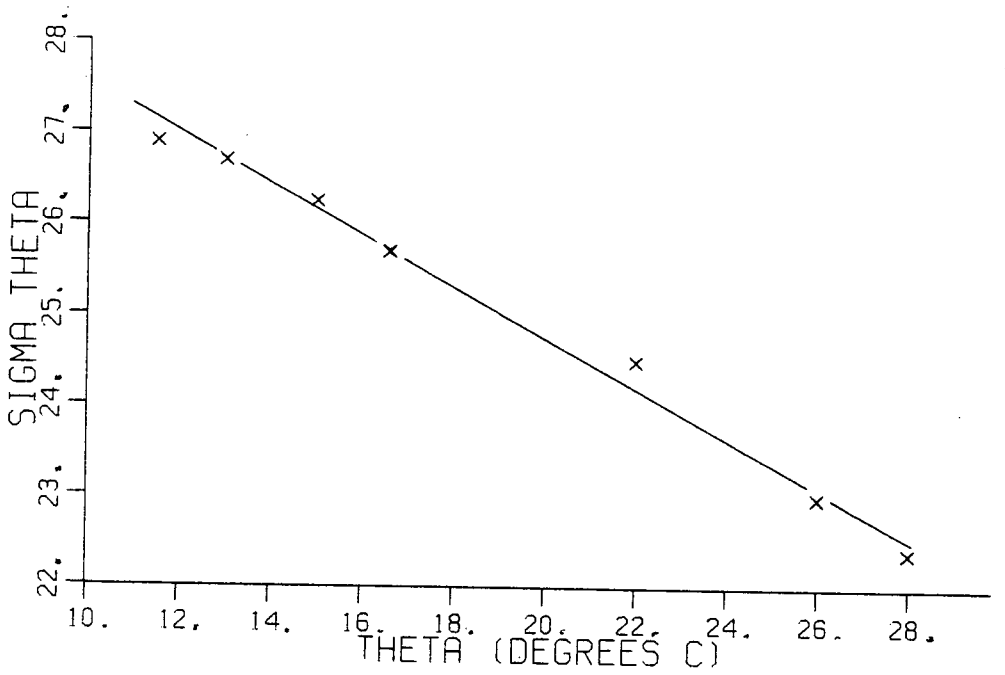

Fig.IV.15. Sigma$_\theta$ vs. Θ for the upper 300 meters of the stratification data in Cox (1976) (see Fig.IV.14).

also want the first layer deep enough to include the top current meter of K2 at 125m). The depth of the second layer is somewhat more arbitrary ; I will include the remainder of the thermocline in the second layer, giving it a depth range of 130 to 200 meters. I will make the total depth representative of K2, that is , a total depth of 300 meters (making the bottom layer 100 meters thick). With these specifications , it is now possible to obtain the representative densities of each layer by averaging the profiled temperatures (Fig.IV.13) over each layer. I find, using $\sigma_t = \sigma_0(1-\alpha' T)$ with $\sigma_0 = 30.3$ and $\alpha' = 0.0092°C^{-1}$:

(layer 1) $T_1 = 25.8°C$ $\sigma_t)_1 = 23.$

(layer 2) $T_2 = 17°C$ $\sigma_t)_2 = 25.5$

(layer 3) $T_3 = 12.4°C$ $\sigma_t)_3 = 27.$

The stratification is, of course, subject to seasonal change. Fig.IV.16a,b shows the temperature stratification at the high and low extremes in early March and late May , respectively. Representing the stratification by (dT/dz) (at z=176m, since I know the profile shape best here) I find this value only varies from 0.06°C/m to 0.07°C/m in going from the low to the high temperature case. Thus, seasonal variation of stratification is unlikely to be important in the model parameterization.

Having decided on layer depths, I can now average the mean longshore velocities (based on Fig.III.13a,b,c) over the vertical extent of each layer. In averaging over the top layer ,

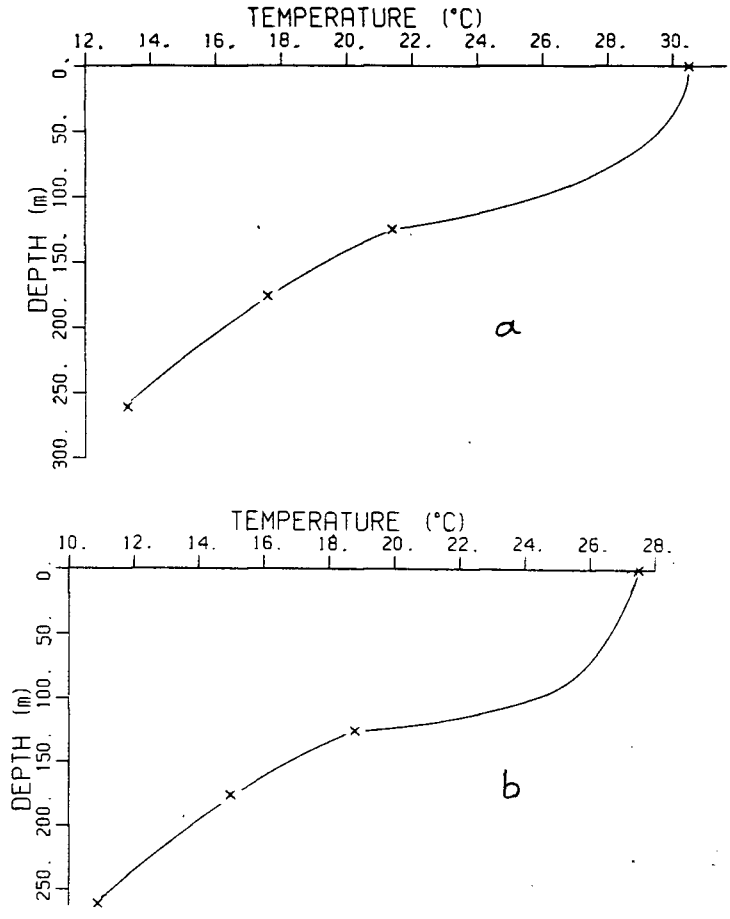

163

Fig.IV.16. (a) Temperature stratification at station K2 during period of lowest temperatures (late May). The point at the surface is estimated from data in Brown, Bruce and Evans (1980). (b) Temperature stratification at station K2 during the period of maximum temperatures (early March). The point at the surface is estimated from data in Brown , Bruce, and Evans (1980).

an assumption must be made as to the magnitude of the near-surface velocity. Here, I have little information as to the

seasonal variation of this quantity. Based on Fig.III.12 I assume a minimum speed of about 25 cm/s, during the Northeast Monsoon. Data from Düing, Molinari, and Swallow (1980) suggests a maximum speed of about 120 cm/s , during the Southwest Monsoon. Between these extremes, I assume a variation similar in shape to the mean curve in Fig.III.13a. This allows me to draw approximate profiles and perform the depth averages. The time variations of the average velocities are illustrated in Fig.IV.17 .

A constant bottom slope is , as indicated earlier (Fig.III.15) ,inappropriate. The actual bottom slope (α) varies from about -4×10^{-3} (shelf) to -50×10^{-3} (slope) over the channel width; thus I will assume an average slope of about -26×10^{-3}.

I now summarize the preceeding discussion regarding parameter values:

$$L = 10^5 m\ ,\ H_1 = 130m\ ,\ H_2 = 70m\ ,\ H_3 = 100m\ ,$$
$$f = -7.1\times10^{-6} s^{-1}\ ,\ \bar{U} = 0.5\ m/s\ ,\ \alpha = -2.6\times10^{-2},$$

$$\left.\begin{aligned}\sigma_t)_1 &= 23.\\ \sigma_t)_2 &= 25.5\\ \sigma_t)_3 &= 27.\end{aligned}\right\}\quad \left.\begin{aligned}g_2' &= 2.5\times10^{-2}\ m\,s^{-2}\\ g_3' &= 1.5\times10^{-2}\ m\,s^{-2}\end{aligned}\right\}$$

$$R_o = \frac{\bar{U}}{|f_o|L} = 0.7\ , \qquad \text{(IV.78)}$$

$$F_{21} = \frac{f_o^2L^2}{g_2'H_1} = 0.155$$

$$F_{22} = \frac{f_o^2L^2}{g_2'H_2} = 0.288$$

$$F_{32} = \frac{f_o^2L^2}{g_3'H_2} = 0.48$$

$$F_{33} = \frac{f_o^2L^2}{g_3'H_3} = 0.336\ ,\quad T = \frac{\alpha|f_o|L^2}{H_3\bar{U}} = 36.9\ .$$

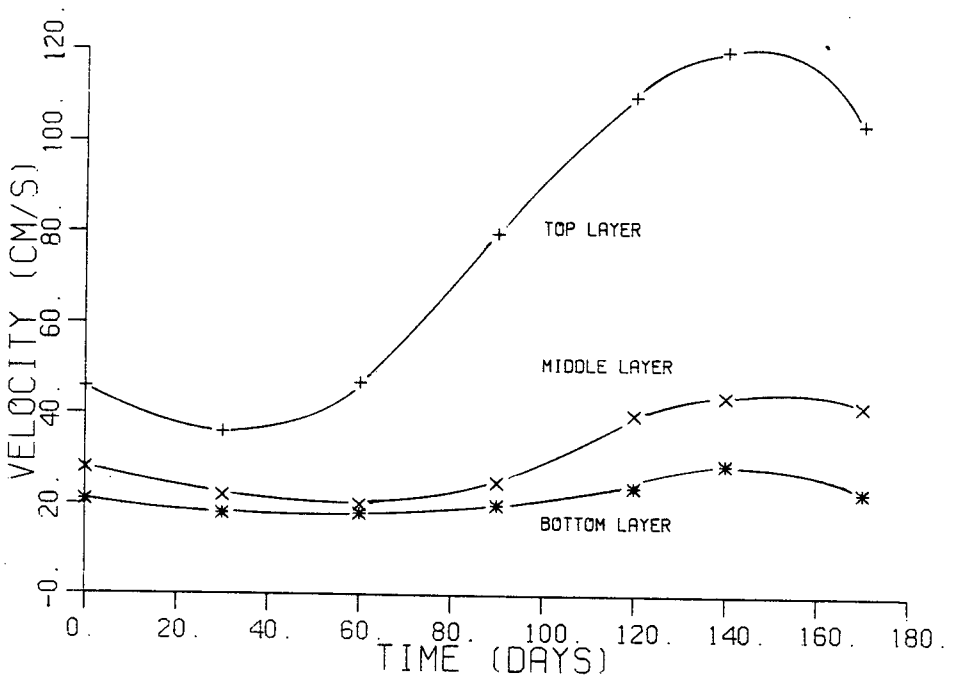

Fig.IV.17. Depth averaged longshore velocities as a function of time.

The chosen layer thicknesses give one current meter per layer (see Table 1). The Rossby number (R_o) appears to be too large ($\approx$0.7) to justify a quasi-geostrophic treatment. However, the expansion can be justified a posteriori. The Rossby number multiplies both the advective term kV and the time variation ω (i.e., the Rossby number multiplies the Lagrangian time variations ω-kV). In the calculations to follow it will be found that for Somali Current conditions the near resonant waves of interest approximately satisfy the advective condition ω=kV, so that the Lagrangian time variations are in fact small and a quasi-geostrophic treatment is justified.

Model Properties

With the parameters fixed as listed in (IV.78) the dispersive properties of the three-layer system may be investigated. The relevant dispersion relation (that is, the relation between ω and k which satisfies det(A_{ij})=0, see (IV.76), when $C_I = C_B = 0$), is shown in Fig.IV.18 for the case of maximum mean velocities V_1 =100cm/s, V_2 =25cm/s, V_3 =8cm/s. The upper curved line represents the topographic mode . The two almost straight lines are shear modes (waves depending on the interfacial slope for their restoring force , much as topographic waves depend on bottom slope for a restoring force). These lines are straight because the waves are moving almost entirely due to advection by the mean flow. That is , because restoring forces are small (the rotational Froude numbers F_{ij}

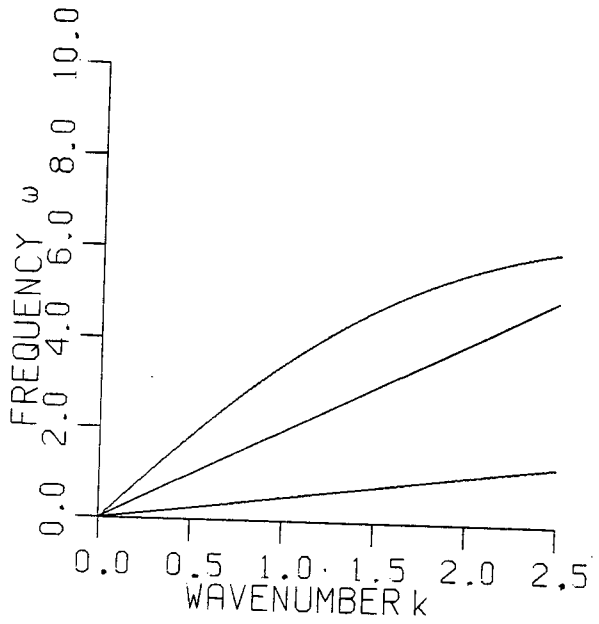

Fig.IV.18. The dispersion relation for the maximum shear case V_j =(100,25,8)cm/s, with the other parameters having values given in equation(IV.78). The three modes evident here are described in the text.

are small) the waves satisfy $\omega_o \cong kV_j$ for the two upper layer velocities V_j . It is also seen that no instabilities occur in the wavenumber region of interest. (I am interested in wavenumbers near those that satisfy the dispersion relation for ω_o (ω_o =.29 , corresponding to a period of 50 days). Since these curves represent the maximum shear case, one need not be concerned with the complicating effects of instability (which occurs when the top two curves coalesce).

I will now specify the spatial structure of the forcing which appears in (IV.77): I assume that the atmospheric 40- to 50- day oscillations propagate as waves parallel to the coast. Information presented in Chapter II showed that the 40- to 50-day oscillations do in fact propagate almost parallel to the coast (at low altitudes) and a wavelength of about 3200km was deduced (based on the observations of Murakami, Nakazawa and He, 1984). The amplitude of the oscillation is assumed constant over the narrow (100km) channel. That is,

$$F(x,y,t) = \text{const.}\, e^{i(k_o y - \omega_o t)}$$

so that

$$\tilde{f}_m(k) = \begin{cases} \text{const.} \dfrac{4}{\pi m}\, \delta(k-k_o) & m \text{ odd} \\ 0 & m \text{ even} \end{cases} . \qquad \text{(IV.79)}$$

With this forcing the velocity response in each mode (m) decreases approximately with the square of the mode number. Since the even modes are not excited, the response of the first mode is almost ten times that of the next excited mode (the third). Accordingly, I only consider the first mode here. I can now write

$$\psi_j(x,y,t) = \text{const.}\, e^{i(k_o y - \omega_o t)} T_{j,1}(k_o) \sin m\pi x . \qquad \text{(IV.80)}$$

Thus the phase and amplitude of the response are determined by the transfer functions $T_{j,1}(k_o)$.

The transfer functions (phase and amplitude) are illustrated in Fig. IV.19a,b,c for the same maximum shear case discussed above with regard to the dispersion relation. I have chosen a relatively small friction coefficient, $C_I = 10^{-5}$m/s, in order that all three modes be resolved for purposes of illustration. In the surface layer, only the upper-layer shear mode ($k \approx .145$) is apparent in the amplitude reponse . In the second layer , the upper-layer shear mode dominates but the second-layer shear mode ($k \approx 0.55$) is apparent. The third-layer response is also dominated by the upper-layer shear mode, but the topographic mode ($k \approx 0.09$) is well resolved, too. In this low friction case, the resonant peaks are situated close to the resonant wavenumbers found in Fig.IV.18 (corresponding to $\omega_o = 0.29$). The amplitude response decreases rapidly with increasing depth, in this low friction case. One sees that the upper-layer dynamics dominate the response in all layers. The

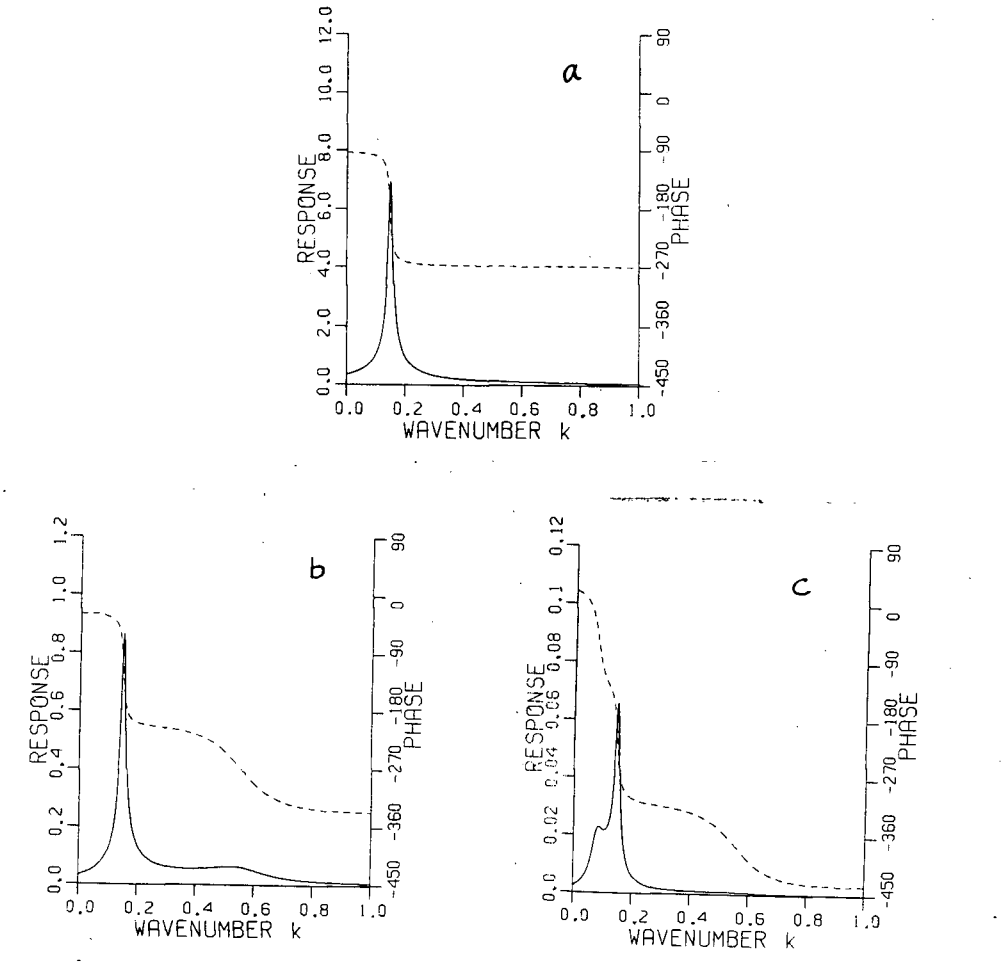

Fig.IV.19. (a) The nondimensional amplitude (solid line) and phase (dashed line) of the upper layer transfer function under conditions of maximum shear , with other parameters as listed in equation(IV.78) and $C_I=10^{-5}$ (m/s), and $C_B=3x10^{-5}$ (m/s). The phase shown is that of the longshore velocity fluctuations relative to the forcing.
(b) As in (a), except for the second layer. Note that the amplitude scale is one tenth that in (a).
(c) As in (a), except for the bottom layer. Note that the amplitude scale is one hundredth that in (a).

phase curve in the top layer exhibits the classic behavior in going through resonance; that is, one sees a 180° phase shift in going from one side of resonance to the other. The phase

characteristic of the middle layer is more complicated , with an additional phase shift due to the second-layer shear mode. It is interesting to note that the second layer actually leads the top layer at resonance in the upper-layer shear mode ($k \approx 0.145$). The bottom layer shows phase shifts associated with all three modes; the total phase change in going from k=0 to k large and positive is much greater than the 180° phase shift seen in the top layer. As expected, increasing friction has the effect of broadening the response peaks and making the phase changes less sharp as resonance is approached . The second-layer shear mode and the topographic mode tend to be suppressed as friction increases. The amplitude of the upper-layer shear mode (at resonance) in each layer has an interesting behavior, as illustrated in Fig.IV.20 (note that separate scales are used for the upper and two lower layer amplitudes). The response in the top layer decreases very rapidly as interfacial friction increases. The second layer shows an initial rapid decrease , then levels off. In the bottom layer a slow decrease is followed by a clear increase in amplitude. Thus, there are two conflicting tendencies in the lower layers:

(i.) increasing friction "detunes" the system, tending to decrease response, while

(ii.) the increased frictional drag from the layer above tends to force the response to higher values.

How do other parameter changes affect the transfer functions? It was shown that the stratification changes seasonally , and this will affect the rotational Froude numbers.

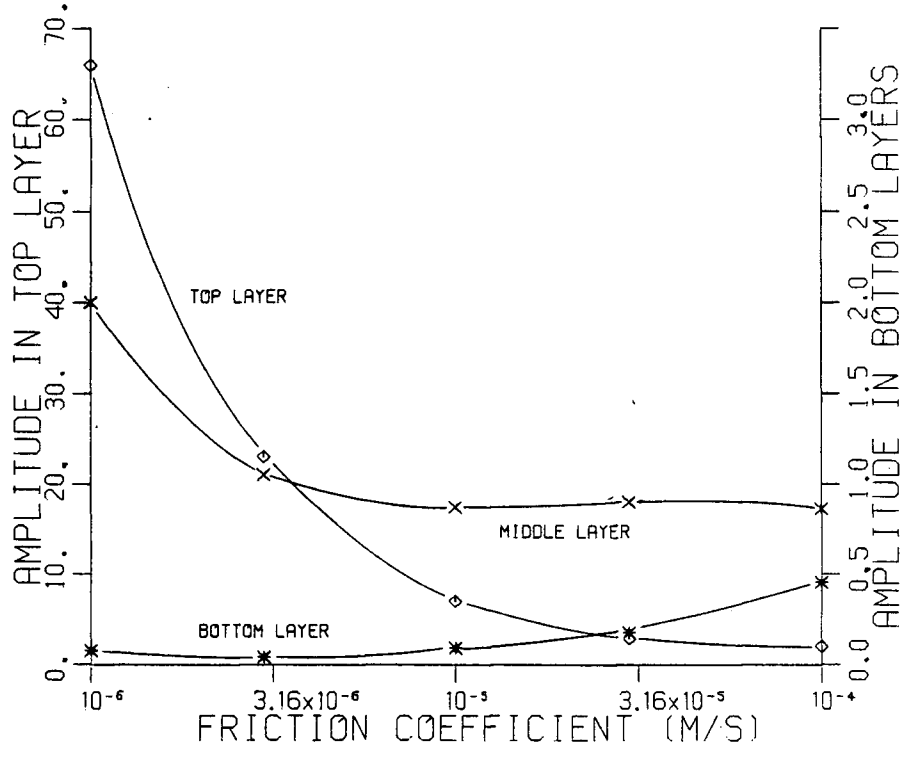

Fig.IV.20. Layer amplitudes for the upper layer shear mode as a function of the interfacial friction parameter C_I. This figure applies to the maximum shear case, with the other parameters as listed in equation(IV.78). Note that the horizontal axis is logarithmic and that separate vertical scales are used for the upper layer and the two lower layer amplitudes.

However, the transfer functions are quite insensitive to small rotational Froude number changes, and it was previously found

that the temperature gradients change little from one seasonal extreme to the other. Changes in mean current velocity are much more important , given their large magnitude (see Fig.III.11). Generally speaking, as the mean current velocities decrease the response curve of the dominant upper layer broadens, and its amplitude at resonance decreases. More importantly , however, is the change of the resonant wavenumber of the upper-layer shear mode with (time) change in current speed (Fig.IV.21) . Since the waves are propagating primarily by advection, the resonant wavenumber is simply given by $k_{RES} = \omega_o / V_1$ (where V_1 is the velocity of the surface layer). With these considerations in mind one can now apply the model to the Somali Current situation.

I will now compare the low-passed curl record with the top sensor longshore velocity record (Fig.IV.22). After about 40 days (from the record's start) the two time series show a tendency to be anti-correlated (that is, they show an apparent 180° phase shift) until about 120 days (after which they slip into phase). The model presented earlier predicts a 180° phase shift between the forcing and the velocity response (see, eg., Fig.IV.19a) when resonance is achieved. I believe that this period of large velocity amplitude and 180° phase shift represents a period of near resonance between the curl of the wind stress forcing and the velocity response . Examination of Fig.IV.21 shows that this near resonance can last only for a limited period of time, as the upper-layer velocity slowly changes in time. That is, assuming narrow band wavenumber

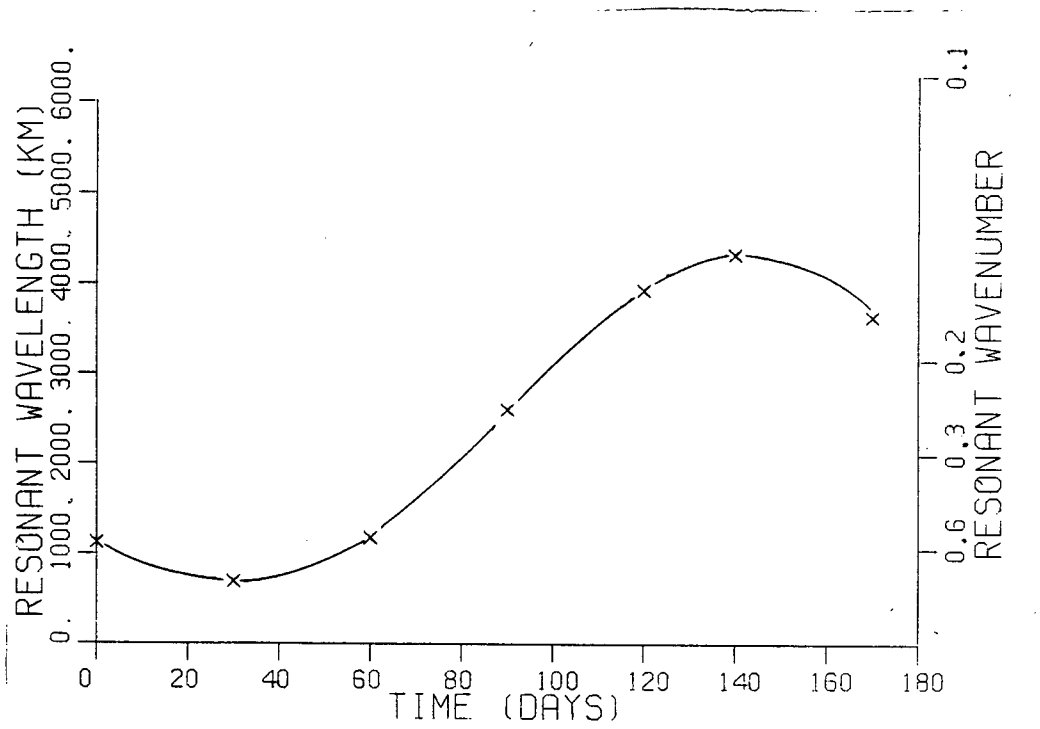

Fig.IV.21. The resonant wavenumber and wavelength for the upper layer shear mode as a function of time.

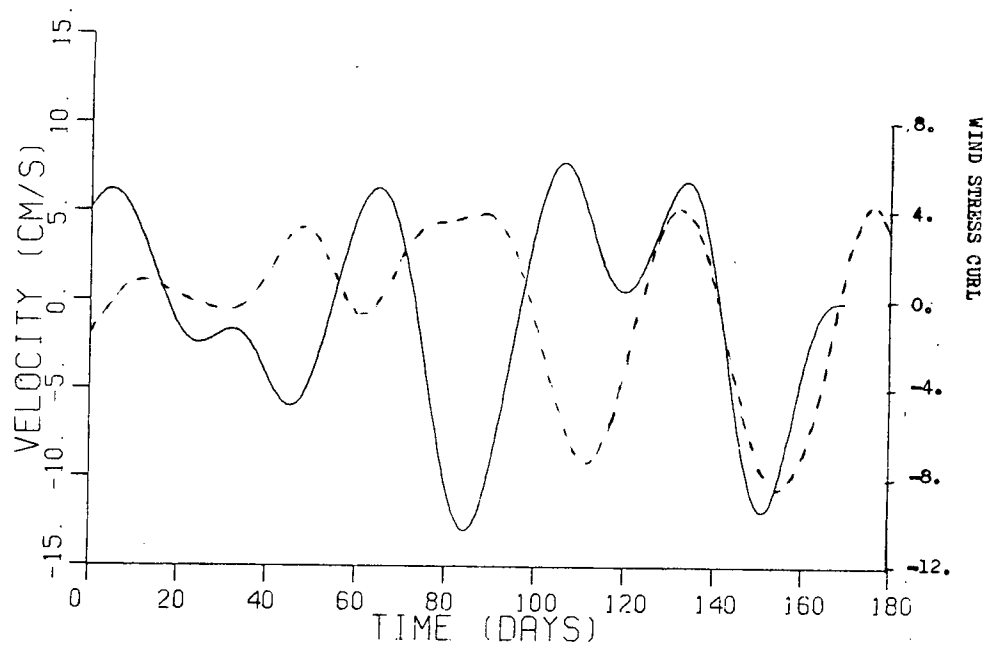

Fig.IV.22. Comparison of longshore velocity fluctuations from the top sensor at station K2 (solid line) with wind stress curl (dashed-line; the curl is in units of 10^{-8} N/m^3).

forcing, the resonant wavenumber of the system is first greater than the input wavenumber, then as time elapses it becomes smaller than the input wavenumber.[7] If one takes the input wavenumber as corresponding to the middle of the resonant interval, one finds a value of $k_{INPUT} \approx 0.25$, corresponding to wind forcing with a wavelength of about 2500km[8]. This value of 2500 km is in reasonable agreement with the value of 1500 km obtained from the longshore phase shift of the temperature time series, and is in very good agreement with the wavelength of atmospheric oscillations (λ =3200 km) established in Chapter II. The system transfer functions for this $k_{RESONANT}$ =0.25 situation are shown in Fig.IV.23a,b,c (friction coefficients of $C_I = C_B = 3 \times 10^{-5}$m/s have been used). Note that the surface-layer velocity amplitude is about 8cm/s, in quite good agreement with the values observed in the low-passed velocity record (Fig.III.21a). Velocities of about 2cm/s are predicted in the middle layer. The low-passed record from the second sensor (Fig.III.21b) shows fluctuations on this scale (before 120 days); however, it is not clear that these really are 50-day

---

[7]For a wave period of 50 days, the relevant theoretical time scale is $\omega_{DIM}^{-1} \approx$ 8 days. Since this is much shorter than the time scale of mean velocity changes shown in Fig.IV.17 (40-80 days), this type of analysis is meaningful in a WKB sense.

[8]The corresponding relevant theoretical length scale is $k_{DIM}^{-1} \approx$ 400km, which is less than 4° of latitude. Thus it appears reasonable to apply our channel model to the region of consideration (2°-4°S).

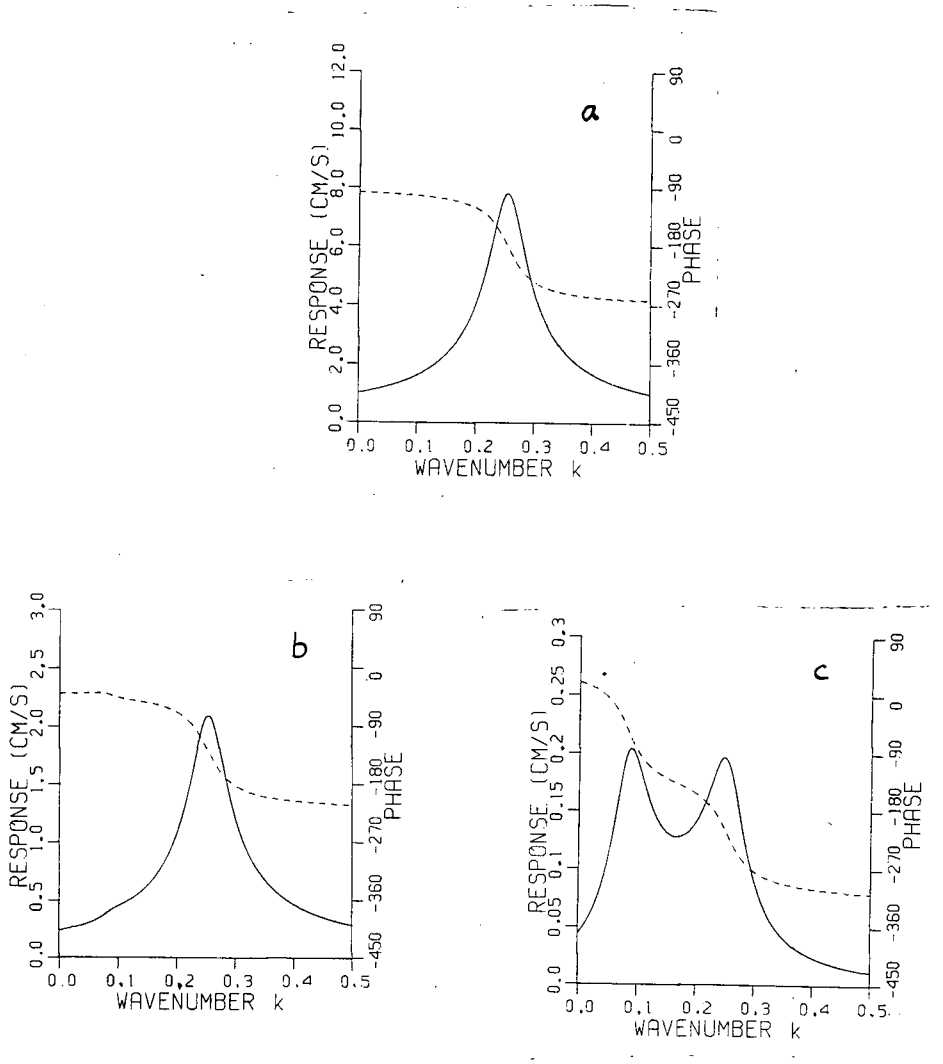

Fig.IV.23. (a) The amplitude (solid line) and phase (dashed line) of the wind induced longshore velocity as a function of the resonant wavenumber for the upper layer. The physical situation is described in the text.
(b) As in (a), except for the middle layer. Note that the vertical scale is one-quarter that in (a).
(c) As in (a) , except for the bottom layer. Note that the vertical scale is one-fourtieth that in (a).

oscillations . The same statement applies to the bottom sensor fluctuations; the amplitude is in good agreement (before 120 days) with that predicted, but observed fluctuations seem

noiselike in character.

What then happens at 120 days and after? The system is no longer resonant, and, thus, the wind sress curl can no longer excite substantial oscillations at the sensor depths. Yet , the comparison in Fig.IV.24 clearly shows the peak at about 130 days to be in phase with a peak in the wind stress . Also the pulses observed at the second sensor and at the bottom sensor (characterized by negative velocity) occur at about the same time. Comparison of Fig.IV.22 with Fig.IV.24 is helpful here. One sees that just after 130 days the wind stess itself has a strong peak , coinciding in time with the above mentioned events. The wind stress can only generate significant forcing if it interacts with the bottom topography; that is the longshore component of the wind stress sets up a near-bottom return flow for the Ekman transport at the surface. This transport then takes place over rapidly varying topography and can thus induce vortex stretching. If one imagines the return flow to be confined to a bottom layer, then one obtains a bottom forcing term

$$\frac{1}{\rho h_B^2} \frac{\partial h_B}{\partial x} \tau^{(x)}$$

where h is the thickness of the bottom layer. If one applies this forcing to the bottom layer of the 3-layer model (while neglecting the surface forcing) one can calculate the expected responses in each layer. While the response will now be off-resonant, one may expect substantial amplitudes because the bottom forcing term is 20 times larger than than the curl of the

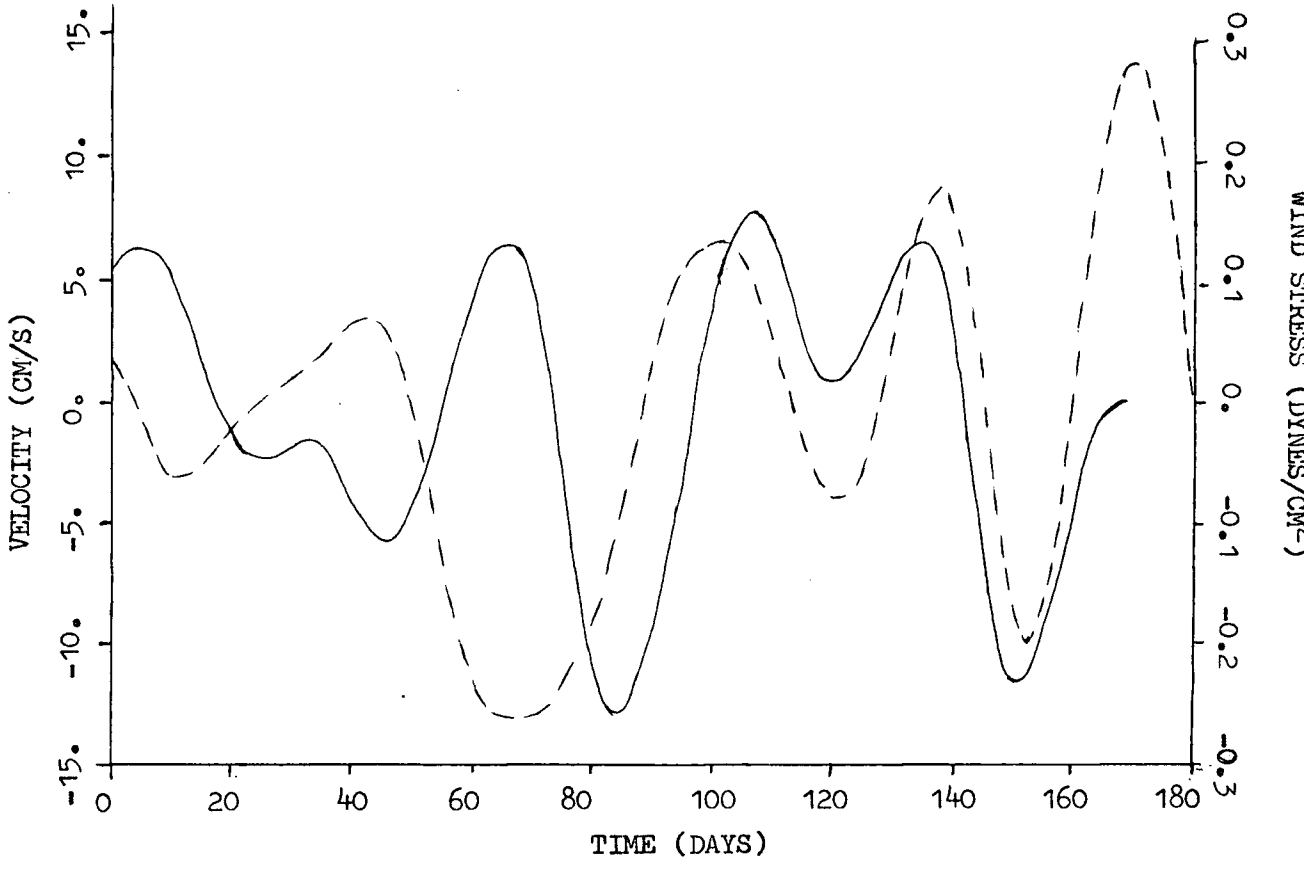

Fig.IV.24. Comparison of longshore velocity fluctuations (solid line) with wind stress (dashed line).

wind stress term. The results of such a calculation are shown in Fig.IV.25a,b,c . Amplitudes and phases are calculated on the curves at k=0.25. One sees that a reasonable amplitude and phase

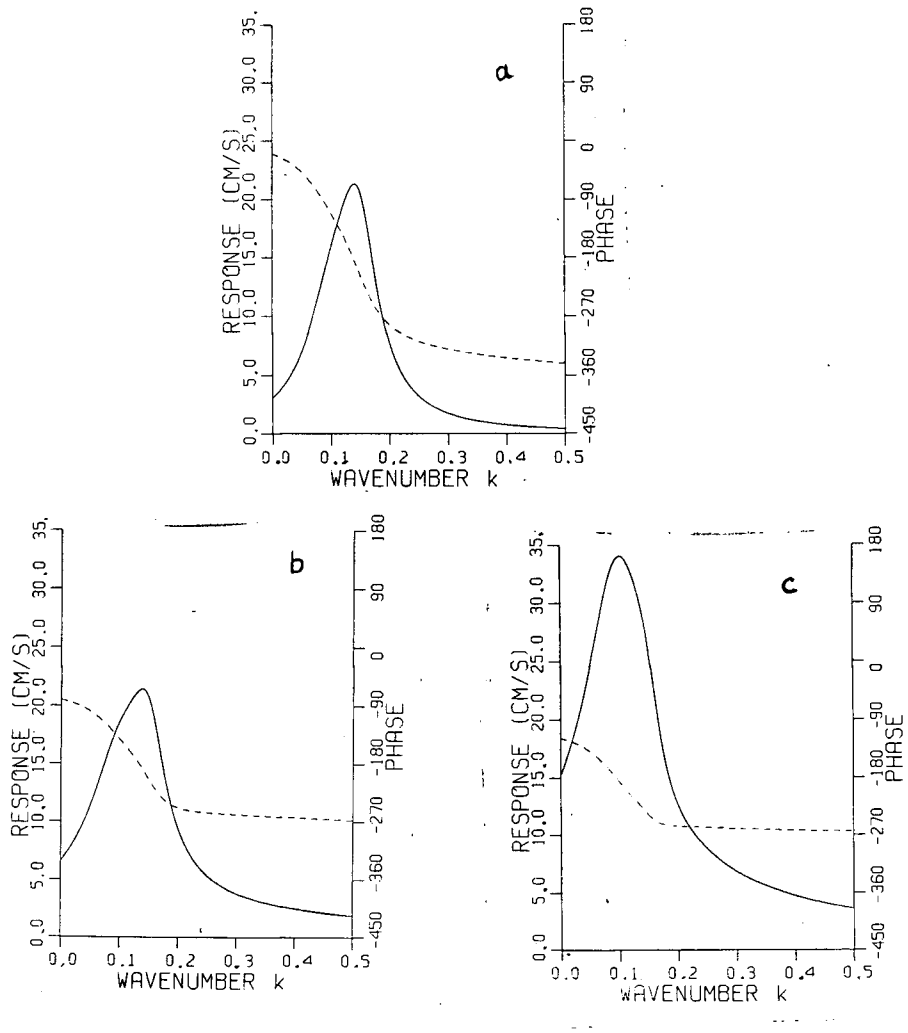

Fig.IV.25. (a) The amplitude (solid line) and phase (dashed line) of the wind induced longshore velocity as a function of the resonant wavenumber for the upper layer in the case of bottom forced motion. The physical situation is described in the text.
(b) As in (a), except for the middle layer.
(c) As in (a) , except for the bottom layer.

is obtained for the top layer: a speed of about 3 cm/s is low for the velocity peak observed in Fig.IV.24 at 130 days, but the calculated phase of about -310° is close to the phase relationship observed. It seems plausible then , that the upper

sensor peak at 130 days is due to the longshore wind stress, and that divergence effects associated with this increase of wind stress give rise to the aforementioned suppression of the temperature peak in Fig.III.20. The amplitude in the second layer is larger than that in that in the first, in accordance with observation (the pulse in Fig.III.21b at 140 days has an amplitude of 16cm/s , as compared to the 8cm/s peak in Fig.III.21a. The phase of this motion, however, is in disagreement with observation . The model predicts the second layer to lead the top layer by almost 90°, whereas they are observed to be virtually in phase. The bottom layer has a large predicted amplitude ($\approx$10cm/s) in contrast to observation (Fig.III.21c). Further the model predicts a 270° phase shift between wind stress and response in contrast to the clear 180° phase difference observed (the stress in Fig.IV.24 vs. Fig.III.21c). The bottom-forced model makes reasonable qualitative predictions for this part of the record. In contrast to the surface-forced model it yields strong current responses in the lower two layers which is as required by observation. The quantitative predictions are poor as may be anticipated from the fact that the topographic forcing varies greatly along the channel. Thus, the response at station K2 will be the sum of many wave responses, each arriving from a region of different topography. For example, a particularly strong contribution may come from the region where the topographic mode is resonant with the wind forcing (near station K1). This would give rise to a wave exhibiting a 180° phase shift relative to the forcing, and

this is just what is observed at the bottom sensor, as noted above.

IV.7 Leakage of Shear Waves into the Equatorial Waveguide

It was noted in section IV.5 that waves propagating on the restoring force provided by the horizontal mean current shear can cross the equator , since the restoring force does not depend on f. However, the disturbance these waves create in the equatorial waveguide will give rise to some equatorial wave propagation. The question is , how much energy leaks from shear modes to equatorial modes?

Evidence discussed in Chapter II leads one to believe that the 40- to 50-day oscillation propagates as an equatorial Kelvin wave in the Indian and Pacific Oceans. Thus , I examine the leakage of shear waves crossing the equator into an equatorial Kelvin mode. To examine this situation I need the momentum equations for the free equatorial Kelvin wave

$$u_t = -p_x/\rho \tag{IV.81a}$$

$$\beta y u = -p_y/\rho \tag{IV.81b}$$

with boundary condition

$$u(x=0, y, t, z) = \bar{U}(y, z, t) \tag{IV.82}$$

the function U representing the zonal component of the velocity of the shear wave crossing the equator . This problem is analogous to the treatment of current-generated trench waves

presented by Mysak and Willmott (1981). This approach will be consistent provided the leakage is relatively small so that it is not necessary to consider the loss rate in determining U(y,z,t). The forcing function, U, is here considered to be confined to a thin upper layer ($\approx$100m, as in section IV.5) lying over deep ocean (of about 3500m depth). I will also assume constant N^2 type stratification, so that one has simple vertical modes $\cos(n\pi z/H)$. With these assumptions I write

$$u = e^{-\frac{\beta}{2(gh_1)^{\frac{1}{2}}}y^2} \cos\left(\frac{\pi z}{H}\right) u_0(x,t) \qquad \text{(IV.83)}$$

(I consider here only the first baroclinic mode, of equivalent depth h_1, since Luther's observations indicate that the 40- to 50-day oscillation propagates as a first baroclinic mode Kelvin wave). The effective forcing function U(t) must be projected onto the vertical and latitudinal eigenmodes. Since U(t) represents a wave one has

$$\bar{U} = \bar{U}_0 e^{i(ky-\omega t)} \mathcal{H}(z+h) \qquad \text{(IV.84)}$$

where $\mathcal{H}(z+h)$, the Heavyside step function, is given by

$$\mathcal{H}(z+h) = \begin{cases} 1 & z > -h \\ 0 & z \leq -h \end{cases},$$

The projection cofficient for the latitudinal dependence is

given by

$$a_\ell = \frac{\int_{-\infty}^{\infty} e^{\frac{-\beta}{2(gh_1)^{\frac{1}{2}}} y^2} \cos ky \, dy}{\int_{-\infty}^{\infty} e^{\frac{-\beta}{(gh_1)^{\frac{1}{2}}} y^2} dy} \qquad \text{(IV.85)}$$

$$= \sqrt{2} \exp\left[-k^2 \frac{(gh_1)^{\frac{1}{2}}}{2\beta} \right] .$$

The projection coeffient for the vertical dependence is given by

$$a_z = \frac{\int_{-H}^{0} \cos\left(\frac{\pi z}{H}\right) \cos(z+h) \, dz}{\int_{-H}^{0} \cos^2\left(\frac{\pi z}{H}\right) dz} \qquad \text{(IV.86)}$$

$$= \frac{\frac{H}{\pi} \sin\left(\frac{\pi h}{H}\right)}{H/2}$$

and since h<<H

$$a_z \approx \frac{2h}{H} .$$

Thus

$$\bar{U}_{Effective} = \bar{U}_0 \frac{2h}{H} \exp\left[-\frac{(gh_1)^{\frac{1}{2}}}{2\beta} k^2 \right] \sin\omega t .$$

From equations (IV.81a,b) , one finds

$$\frac{\partial}{\partial t} u_0(x,t) - (gh_1)^{\frac{1}{2}} \frac{\partial}{\partial x} u_0(x,t) = 0 \qquad \text{(IV.87)}$$

$$\text{with} \quad u(x=0,t) = \sin\omega t \, \bar{U}_0 \frac{2h}{H} \exp\left[-\frac{(gh_1)^{\frac{1}{2}}}{2\beta} k^2 \right]$$

From Mysak and Willmott (1981) , one knows the solution to be

$$u_0(x,t) = \bar{U}_0 \frac{2h}{H} \exp\left[-\frac{(gh_1)^{\frac{1}{2}}}{2\beta} k^2 \right] \sin\left[2\pi \left(t - \frac{x}{(gh_1)^{\frac{1}{2}}} \right) \right] . \qquad \text{(IV.88)}$$

I take U_o to be about 1cm/s (much less than the meridional component of about 10cm/s) , and k=(2π/3000km). Lightill (1969) gives h_1 to be .75m for Indian Ocean conditions. Thus, I have

$$u_o(x,t) = 1\,cm/s \; \frac{200\,m}{3500\,m} \exp(-0.3) \sin\left[2\pi\left(t - \frac{x}{(gh_1)^{\frac{1}{2}}}\right)\right]$$

$$\cong 0.05\,cm/s \sin\left[2\pi\left(t - \frac{x}{(gh_1)^{\frac{1}{2}}}\right)\right].$$

Hence, I find that the leakage of shear waves into the equatorial Kelvin mode is negligible.

V. Summary and conclusions

In chapter II I reviewed the literature establishing the existence and properties of the 40- to 50-day oscillation in the atmosphere and to a lesser extent , in the ocean. The atmospheric oscillation is now known to be global in nature. The tropical component , propagating eastward and modulating the Walker circulation, is connected to a midlatitude component by poleward propagating fluctuations. Although less is known about it, the oceanic oscillation probably propagates as an equatorial Kelvin wave (confined to within 3° of the equator) in the Pacific Ocean and in the Indian Ocean.

In Chapter III is described an original analysis of data from the source region of the Somali Current , which showed the 40- to 50-day oscillation to exist in the atmosphere and ocean and to have unique properties there. Some of the data were consistent with the results from Chapter II showing the atmospheric fluctuations to propagate parallel to the coast , probably due to the effect of the East African Highlands. The existence of 40- to 50-day fluctuations in the wind stress curl has been shown for the first time in any region. This is particularly important since the wind stress curl is a major forcing term for low-frequency oceanic motions. Previous work has detected oceanic fluctuations at 40- to 50-days period only as mid-ocean equatorial motions. I have shown here that the oscillation exists as a coastal signal in the Somali region,

propagating parallel to the coast and toward the equator. The strength of the current fluctuations is impressive, over 10cm/s at depths in excess of 100m. These fluctuations are seen to vary in amplitude with time , posing the challenge of relating these variations to changes in the mean flow conditions and possible atmospheric forcing. I have demonstrated the existence of large temperature fluctuations in the 40- to 50-day period range. These fluctuations (of the order of 2°C at the upper sensor of station K2) may play an important role in the air-sea interactions thought to be ultimately responsible for the 40- to 50-day oscillation.

In Chapter IV I showed the atmospheric 40- to 50-day fluctuations are energetic enough to drive the observed oceanic fluctations. In particular , I demonstrated that the wind stress curl fluctuations directly pump the oceanic temperature fluctuations . The strength of the wind stress curl fluctuations is sufficient to drive the observed equatorial Kelvin waves of 40- to 50-days period in the Pacific. I modelled waves propagating parallel to the Kenyan coast, restored by forces associated with vertical and horizontal current shears , and showed that atmospheric forcing is sufficient to account for the oceanic 40- to 50-day fluctuations observed in the source region of the Somali Current. Waves propagating on the horizontal shear may cross the equator with minimal leakage of energy into the equatorial waveguide . I found that vertical shear modes experience resonance with the atmospheric forcing at a wavelength that corresponds to the known wavelength of

atmospheric 40- to 50-day fluctuations (~3000km). This resonance condition gives the best fit between model and observed properties. The energy I believe to exist in these vertical shear modes will, in contrast to the horizontal shear modes, be strongly leaked into the equatorial waveguide and may be an important source of the mid-ocean equatorial 40- to 50-day waves seen in the Indian Ocean. Clearly, the real problem of interest is the leakage of energy into the equatorial waveguide when both horizontal and vertical current shear are present in the modelled current which lies in an unbounded ocean.

BIBLIOGRAPHY

Anderson, D. L. T., 1981:
Cross-equatorial waves with application to the low-level East-African jet. Geophys. Fluid Dynamics, 16 , 267,284.

Anderson, J. R., 1984:
Ph.D. Thesis, Colorado State University, Fort Collins.

Anderson, J., and R. D. Rosen, 1983:
The latitude-height structure of 40-50 day variations in atmospheric angular momentum. J. Atmos. Sci., 40 , 1584-1591.

Bjerknes, J., 1969:
Atmospheric teleconnections from the equatorial Pacific. Mon. Wea. Rev., 97 , 163,172.

Block, R. G., 1984:
El Nino and world climate: Piecing together the puzzle. Environment, 26 , 14-39.

Boyd, J. P., 1977:
A review of equatorial waves in the atmosphere. Review Papers of Equatorial Oceanography, FINE Workshop Proceedings . Nova/N.Y.I.T. University Press.

Brown, O. B., J. G. Bruce, and R. H. Evans, 1980:
Evolution of sea surface temperature in the Somali Basin during the Southwest Monsoon of 1981. Science, 209 , 595-597.

Chang, C. P., 1977 :
Viscous internal gravity waves and low- frequency oscillations in the tropics. J. Atmos. Sci., 34 , 901-910.

Charney, J. G., 1964:
On the growth of the hurricane depression. J. Atmos. Sci., 21 , 68-75.

Cox, M. D., 1976:
Equatorially trapped waves and the generation of the Somali Current. Deep-Sea Res., 23 , 1139-1152.

Düing, W., 1970:
The Monsoon Regime of the Currents of the Indian Ocean. International Indian Ocean Expedition oceanographic monographs, no. 1 , Hawaii Institute of Geophysics, Honolulu, 68 pp.

Düing, W., R. L. Molinari, and J. C. Swallow, 1980:
Somali Current: Evolution of surface flow. Science, 209 , 588- 590.

Düing, W., and F. Schott, 1978:
Measurements in the source region of the Somali Current during the Monsoon reversal. J. Phys. Oceanogr., 8 , 278-289.

Erikson, C. C., M. B. Blumenthal, and P. Ripa, 1983:
Wind- generated equatorial Kelvin waves observed across the Pacific Ocean. J. Phys. Oceanogr., 13 , 1622-1639.

Fernandez-Partagas, J., and W. Düing, 1977:
Surface Wind Maps for the Western Indian from August 1975 to October 1976. Technical Report, Rosentiel School of Marine and Atmospheric Science, Univ. of Miami, Miami, Florida, 33149.

Fernandez-Partagas, J., G. Samuels, and F. Schott, 1980:
Surface Wind Maps for the Western Indian Ocean from January to September 1979. Technical Report, TR80-4, Rosentiel School of Marine and Atmospheric Science, University of Miami, Miami, Florida, 33149.

Gill, A. E., 1982:
Atmosphere-Ocean Dynamics. Academic Press, New York, 661 pp.

Goswami, B. N., and J. Shukla, 1984:
Quasi-periodic oscillations in a symmetric general circulation model. J. Atmos. Sci., 41 ,20-38.

Hayashi, Y., 1974:
Spectral analysis of tropical disturbances appearing in a GFDL general circulation model. J. Atmos. Sci., 31 , 180-218.

Hayes, S. P., 1979:
Benthic current observations at DOMES sites A, B, and C in the tropical North Pacific Ocean. Marine Geology and Oceanography of the Central Pacific Manganese Nodule Province , Plenum Press.

Holton, J., 1979:
An Introduction to Dynamic Meteorology. Academic Press, New York, 391 pp.

Jones, J. H., 1973:
Vertical mixing in the Equatorial Undercurrent. J. Phys. Oceanogr., 3 , 286-296.

Jones, R., 1972:
The use and abuse of spectral analysis in tropical meteorology. Dynamics of the Tropical Atmosphere: Notes from a Colloquiam, 252,263. National Center for Atmospheric Research, Boulder, Colorado.

Julian, P. R., and R. A. Madden, 1981:
Comments on a paper by T. Yasunari, a quasi-stationary appearance of 30 to 40-day period in the cloudiness fluctuations during the summer monsoon over India. J. Met. Soc. Japan, 59, 435-437.

Kanasewich, E. R., 1981:
Time Sequence Analysis in Geophysics . The University of Alberta Press, Edmonton, 480 pp.

Kerr, R. A., 1984:
Slow Atmospheric Oscillations Confirmed. Science, 225 , 1010-1011.

King, C. A. M., 1962:
An Introduction to Oceanography. McGraw Hill, New York, 337 pp.

Krishnamurti, T. N., P. K. Jayakumar, J. Sheng, N. Surgi, and A. Kumar, 1985:
Divergent circulations on the 30 to 50 day time scale. J. Atmos. Sci., 42 ,364-375.

Lau, K., and H. Lim, 1982:
Thermally driven motions in an equatorial beta-plane: Hadley and Walker circulations during the winter monsoon. Mon. Wea. Rev., 110 , 336-353.

LeBlond, P. H., and L. A. Mysak, 1978:
Waves in the Ocean. Elsevier, New York, 602 pp.

Lee, C. A., 1975:
The generation of unstable waves and the transverse upwelling two problems in geophysical fluid dynamics. Ph.D. Thesis, Institute of Oceanography and Institute of Applied Mathematics, University of British Columbia, 157 pp.

Leetmaa, A., 1972:
The response of the Somali Current to the Southwest Monsoon of 1970. Deep-Sea Res., 19 , 319-325.

Leetmaa, A., 1973:
The response of the Somali Current at 2 S to the Southwest Monsoon of 1971. Deep-Sea Res., 20 , 397-400.

Leetma, A., H. T. Rossby, P. M. Saunders, and P. Wilson, 1980:
Subsurface circulation of the Somali Current. Science, 209 , 590-592.

Lighthill, M. J., 1969:
Dynamic response of the Indian Ocean to onset of the Southwest Monsoon. Philos. Trans. R. Soc. Lond., A, 265 , 45-92.

Lindzen, R. S., 1974:
Wave-CISK in the tropics. J. Atmos. Sci., 31 , 156-179.

Luther, D. S., 1980:
Observations of long period waves in the tropical oceans and atmosphere. Ph.D. Thesis, Massachusetts Institute of Technology and Woods Hole Oceanographic Insitution, 210 pp.

Luyten, J. R., and D. H. Roemmich, 1982:
Equatorial currents at semi-annual period in the Indian Ocean. J. Phys. Oceanogr., 12 , 406-413.

Madden, R. A., 1978:
Further evidence of travelling planetary waves. J. Atmos. Sci., 35 , 1605-1618.

Madden, R. A., and P. R. Julian, 1971:
Detection of a 40- to 50 day oscillation in the zonal wind of the tropical Pacific. J. Atmos. Sci., 28 , 702-708.

Madden, R. A., and P. R. Julian, 1972a:
Description of global-scale circulation cells in the tropics with a 40- 50 day period. J. Atmos. Sci., 29 , 1109-1123.

Madden, R. A., and P. R. Julian, 1972b:
Further evidence of global-scale 5-day pressure waves. J. Atmos. Sci., 29 , 1464-1469.

McNider, R. T., and J. J. O'Brien, 1973:
A multi-layer transient model of coastal upwelling. J. Phys. Oceanogr., 3 , 258-273.

McPhaden, M. J. ,1982:
Variability in the equatorial Indian Ocean, Part I: Ocean Dynamics. J. Mar. Res., 40 , 157-176.

Murakami, T., T. Nakazawa, and J. He, 1984:
On the 40- 50 day oscillations during the 1979 Northern Hemisphere summer. Part I: Phase propagation. J. Met. Soc. Japan, 62 , 440-469.

Mysak, L. A., E. R. Johnson, and W. W. Hsieh, 1981:
Baroclinic and barotropic instabilities of coastal currents. J. Phys. Oceanogr., 11 , 209-230.

Mysak, L. A., and A. J. Willmott, 1981:
Forced trench waves. J. Phys. Oceanogr., 11 , 1482-1502.

Niiler, P. P., and L. A. Mysak, 1971:
Barotropic waves along an eastern contintental shelf. Geophysical Fluid Dynamics, 2 , 273-288.

O'Brien, J. J. , and H. E. Hurlburt, 1972:

A numerical model of coastal upwelling. J. Phys. Oceanogr., 2, 14-26.

Quadfasel, D. R., and J. C. Swallow, 1984:
Personal Communication.

Pedlosky, J., 1979:
Geophysical Fluid Dynamics. Springer- Verlag, New York. 624 pp.

Philander, S. G. H., 1973:
The equatorial thermocline. Deep-Sea Res., 20, 69-86.

Philander, S. G. H., 1976:
Instabilities of zonal equatorial currents: I. J. Geophys. Res., 81, 3725-3735.

Philander, S. G. H., 1978:
Instabilities of zonal equatorial currents: II. J. Geophys. Res., 83, 3679-3682.

Philander, S. G. H., T. Yamagata, and R. C. Pacanowski, 1984:
Unstable air-sea interactions in the tropics. J. Atmos. Sci., 41, 604-613.

Pond, S., and G. L. Pickard, 1978:
Introductory Dynamic Oceanography. Pergammon Press, Toronto, 241 pp.

Robinson, A. R., 1966:
An investigation of the wind as the cause of the Equatorial Undercurrent. J. Mar. Res., 24, 179-203.

Schott, F., and D. R. Quadfasel, 1982:
Variability of the Somali Current system during the onset of the Southwest Monsoon, 1979. J. Phys. Oceanogr., 12, 1343-1357.

Schumann, E. H., 1981:
Low frequency fluctuations off the Natal Coast. J. Geophys. Res., 86 6499-6508.

Speth, P., and R. A. Madden, 1983:
Space-time spectral analyses of Northern Hemisphere geopotential heights. J. Atmos. Sci., 40, 1086-1100.

Thompson, J. D., and J. J. O'Brien, 1973:
Time dependent coastal upwelling. J. Phys. Oceangr., 3, 33-46.

Veronis, G., and H. Stommel, 1956:
The action of variable wind stress on a stratified ocean. J. Mar. Res. 15, 43-75.

Weickmann, K. M., 1983:
Intraseasonal circulation and outgoing longwave radiation modes during Northern Hemisphere winter. Mon. Wea. Rev., 111 , 1838-1858.

Weisberg, R., A. Horigan, and C. Colin, 1979:
Equatorially trapped Rossby-Gravity wave propagation in the Gulf of Guinea. J. Mar. Res., 37 , 67-86.

Yasunari, T., 1981:
Structure of an Indian summer monsoon system with a period of around 40 days. J. Met. Soc. Japan, 59 , 336-354.

Appendix I: The Maximum Likelihood Method.

The data analyzed in this thesis presents two problems:

(i.) the shortness of the time series compared to the period under consideration.

(ii.) the essentially quasi-periodic nature of the 40- to 50-day oscillation (potentially leading to rather broad-banded instead of sharp spectral peaks).

These difficulties lead to problems in choosing a spectral window . The window must do two things:

(i.) it must suppress the side-lobes of any major peak (especially important for short time series).

(ii.) it must smooth the data , i.e., enhance the signal to noise ratio.

Given a short time series the method of side-lobe suppression is very important. Traditionally , one simply tapers the data at both ends with a cosine-bell to reduce the ringing (side-lobes). This can , however, unduly reduce the variance of long-period signals. For example, suppose one has only one cycle in the series, as illustrated in Fig.AI.1. Then , tapering with a cosine bell (one multiplies the series by the taper function shown in Fig.AI.2 strongly reduces the oscillation at its peak

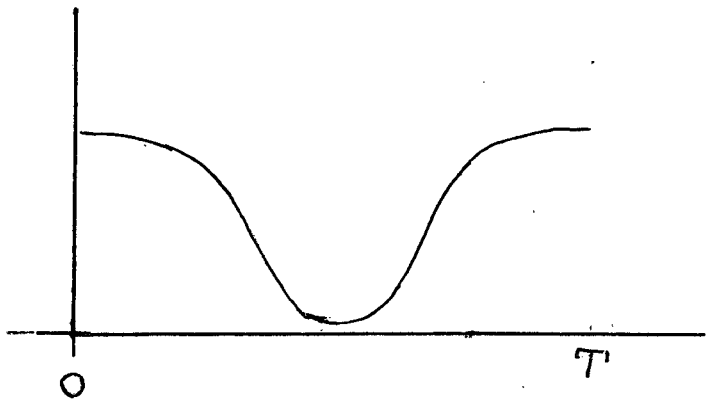

Fig.AII.1. Time series with peaks at ends.

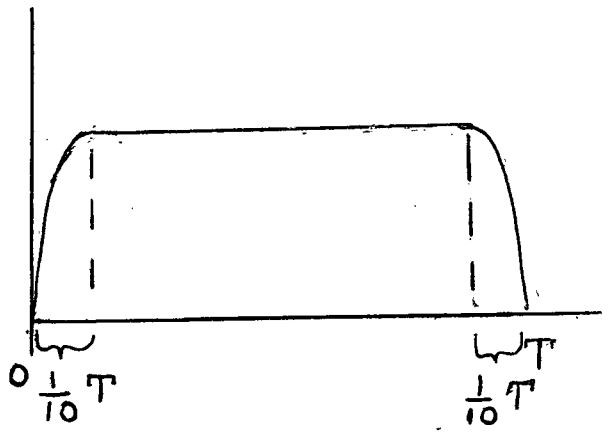

Fig.AII.2. Cosine bell taper.

Fig.AII.3. Time series with peak in middle.

values. Note that a much different result might be obtained if the cycle has its peak in mid-series (see Fig.AI.3- the taper has little effect). Thus , one wishes to use an optimally chosen window. In the maximum liklihood case , the window optimally passes sinusoids. In the maximum entropy case one obtains an optimally smooth spectrum. However, there seems to be the possibility of over smoothing when dealing with quasi-periodic processes as is illustrated in Fig.AI.4 . In this case the maximum entropy window smooths the 40- to 50-day fluctuations entirely.

The spectra presented in this thesis are calculated using maximum likelihood . In the oceanic spectra, all the 40- to 50-day peaks are significant (with 90% confidence) with only two degrees of freedom (the minimum possible). The curl of the wind stress spectrum (Fig.III.5) also shows a 40- to 50-day peak significant at the same level of confidence (90%) while the wind stress spectra (Figs. III.4, III.8) show significant 40- to 50-day energy at an 80% confidence level (again with two degrees of freedom).

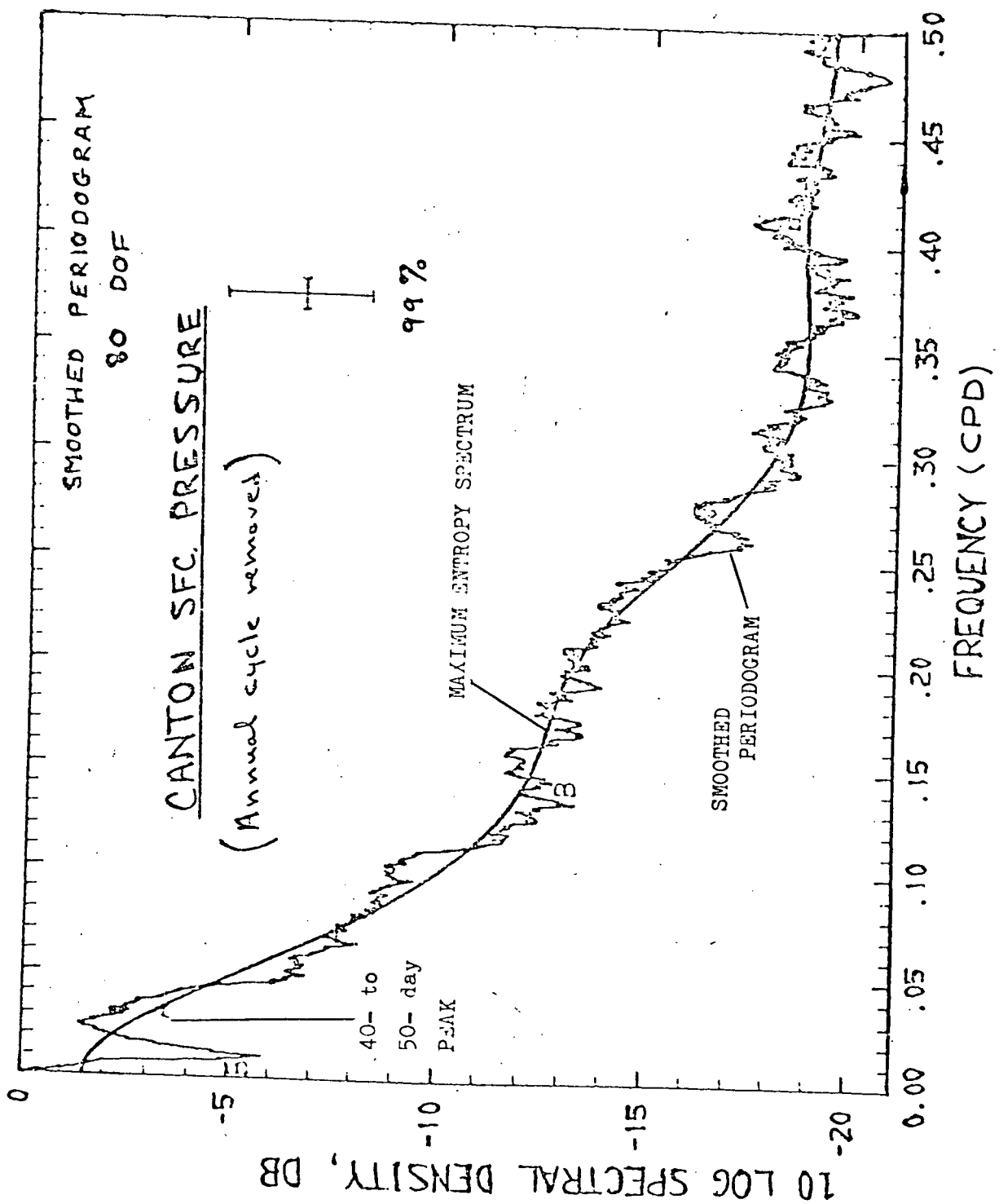

Fig. AII.4. Comparison of maximum entropy and conventional smoothing in resolving the 40- to 50-day peak. (From Jones, 1972).

APPENDIX II.

The coefficients a_{ij} in equation (IV.76) :

$$a_{11} = -(-\omega_o + k V_1)(F_{21} + K^2) + k F_{21}(V_1 - V_2) + i K^2 R_{12}$$

$$a_{12} = (-\omega_o + k V_1) F_{21} - i K^2 R_{12}$$

$$a_{21} = (-\omega_o + k V_2) F_{22} - i K^2 R_{21}$$

$$a_{22} = -(-\omega_o + k V_2)(F_{22} + F_{32} + K^2) + k\{F_{32}(V_2 - V_3) - F_{22}(V_1 - V_2)\} + i K^2 (R_{21} + R_{23})$$

$$a_{23} = (-\omega_o + k V_2) F_{32} - i K^2 R_{23}$$

$$a_{32} = (-\omega_o + k V_3) F_{33} - i K^2 R_{32}$$

$$a_{33} = -(-\omega_o + k V_3)(F_{33} + K^2) - k\{T + F_{33}(V_2 - V_3)\} + i K^2 (R_{32} + R_b)$$

Appendix III. The Effect of the Ocean on the Atmosphere

The purpose of this appendix is to calculate the strength of the atmospheric fluctuations which may be produced by the known oceanic temperature fluctuations in the 40- to 50-day period range (of strength of about 2°C). If these temperature fluctuations can induce atmospheric fluctuations of significant strength, then the importance of the role of the ocean in the generation of the 40- to 50-day oscillations will be established. That is, such a finding will support the idea that ocean-atmosphere interaction is responsible for the 40- to 50-day oscillations.

Philander, Yamagata and Pacanowski (1984) model the atmospheric response to a heat source Q(x,y,t) via the equations

$$-f\bar{V} + g H_x = -A\bar{U} \qquad \text{(AIII.1)}$$

$$f\bar{U} + g H_y = -A\bar{V} \qquad \text{(AIII.2)}$$

$$D(\bar{U}_x + \bar{V}_y) = -BH - Q \qquad \text{(AIII.3)}$$

The coordiates (x,y) measure distance in an eastward and northward direction; the corresponding (atmospheric) velocity components are U and V. The one-layer atmosphere has a depth D (I will treat the oscillation I wish to model as barotropic over a 10 km depth; the 40- to 50-day oscillation has been found to

have appreciable strength at least up to 10 km. Perturbations to D are measured by H. The coefficient for Rayleigh friction is A, and the coefficient for Newtonian cooling is B.

The motions modelled are quasi-steady in that the time variation terms that would normally occur in equations(AIII.1,2) are small compared to the frictional decay term A . That is , $A=(1/5)day^{-1}$, $\omega=(2\pi/50days)\approx(1/8)day^{-1}$. Also, one has $B=(1/15)day^{-1}$. Coupling between the ocean and atmosphere is via the heat source term Q. That is, changes in sea surface temperature (SST) change the water vapor content of the atmosphere and thus the latent heat release responsible for tropical convection. The change in the partial pressure of water vapor in a saturated atmosphere over the ocean may be found from the Clausius- Clapeyron equation:

$$\ln P = -\frac{\Delta E_v}{R}\left(\frac{1}{T}\right) + const. \qquad \text{(AIII.2)}$$

where P is the partial pressure of water vapor , T the absolute temperature, ΔE_v is the latent heat of condensation of water, and R is the gas constant. From this relation one finds that a 2°C fluctuation in ocean temperature (fluctuations of this magnitude were found in Chapter III) giving rise to the same change in surface atmospheric temperature creates a partial pressure change of about 0.02 atm (based on a background temperature of about 300°K). The partial pressure of the water

vapor is equal to the saturation mixing ratio (q_s) multiplied by the molecular weight of water (about 18 grams per mole) divided by the molecular weight of air (about 28 grams per mole) , so that one finds

$q_s \equiv$(mass of water vapor/mass of air in given volume)

$=0.02(18/28) \cong 0.01.$

With this knowlege of the saturation mixing ratio change due to the temperature fluctuation , one can calculate the induced rising (due to latent heat release) velocity from equation(12.36) of Holton(1979):

$$w \frac{\partial \ln \theta}{\partial z} = -\frac{\Delta E_v}{c_p T} \frac{dq_s}{dt} \qquad \text{(AIII.3)}$$

where θ is the potential temperature, C_p is the heat capacity of air at constant pressure , and w is the vertical velocity. (This equation is derived by assuming that the buoyant force due to latent heat release and consequent expansion is balanced by entrainment). I now write equation(AIII.3) as

$$w \frac{1}{\theta} \frac{d\theta}{dz} = -\frac{\Delta E_v \omega}{c_p T} q_s \qquad \text{(AIII.4)}$$

where I have replaced (dq_s/dt) with ωq_s, with ω corresponding to a 50-day period. The term $(d\theta/dz)$ may be estimated from Figure 12.1 of Holton (1979); $(d\theta/dz) \approx 3°K/km$ on average over the lower 10 km of a tropical atmosphere. One thus finds:

$$w \approx 5 \times 10^{-3} \text{ m/s},$$

which is the quantity Q needed in eqaution (AIII.1).

Now note that the types of disturbances we are interested in here only have a zonal component (V=0), so that equation(AIII.1) becomes

$$g H_x = -A\bar{U}$$
$$\Rightarrow H = \frac{A\bar{U}}{igk} \qquad \text{(AIII.5a)}$$

$$D\bar{U}_x = -BH - Q$$
$$\Rightarrow ikD\bar{U} = -(BH + Q) \qquad \text{(AIII.5b)}$$

where I have used $(\partial/\partial x) = ik$. Thus,

$$ikD\bar{U} = -\left(B\frac{A\bar{U}}{igk} + Q\right) \qquad \text{(AIII.6)}$$

and

$$|\bar{U}| = \frac{|Q|}{\left|kD - \frac{BA}{gk}\right|} \qquad \text{(AIII.7)}$$

I now assume k corresponds to a planetary wavenumber 1 (about 40,000 km) oscillation so as to model the global-scale circulation cells. Then, substituting the calculated value of w for Q one finds

$$U \approx 3 m/s.$$

In Chapter III I found zonal wind stress fluctuations of a strength of about 0.3 dyne/cm^2 corresponding to a zonal velocity fluctuation of about 5m/s. Thus, one sees that 2°C fluctuations in SST at a 40- to 50-day period can give rise to a atmospheric velocity fluctuations which are almost as strong as the observed oscillations. Thus, it seems that the ocean has a signifigant input into the dynamics of the 40- to 50-day oscillation in the atmosphere.